The Discrete Multi-Physics method applied to biomechanics

By

Mostapha ARIANE

Primary supervisor: Doctor Alessio ALEXIADIS

Secondary supervisor: Professor Mostafa BARIGOU

A thesis submitted to

The University of Birmingham

for the degree of

DOCTOR OF PHILOSOPHY

School of Chemical Engineering

College of Engineering and Physical Sciences

The University of Birmingham

January 2018

ABSTRACT

Nowadays, computational simulations are frequently used in the biomedical field. In the case of physiological fluids, for instance, they can highlight details of the flow that are very difficult to capture even with the latest visualisation techniques. Moreover, many different solutions can be quickly evaluated numerically so that only the most promising designs are sent to the scale-up laboratory for more expensive and time-consuming tests. In this thesis, we use a new approach to multi-physics, which is based on a mesh-free representation of both the liquid and the solid phases. Instead of using a grid, the solution is calculated on a number of computational particles. This is a 'discrete' approach to multi-physics called the Discrete Multi-Physics that combines the Smoothed Particle Hydrodynamics for the fluid mechanics, the Mass and Spring Model for the solid mechanics and the Discrete Element Method for the contact mechanics. Within this approach, the distinction between liquid and solid depends exclusively on the type of force that acts on each computational particle and therefore a wide range of applications can be covered with a single model and little efforts. For instance, in our simulations of biological valves, we were able to account for repeated opening-closing cycles and also introduce an agglomeration algorithm to model clotting. Besides cardiovascular and venous flows, we also applied the Discrete Multi-Physics and its sub-models to respiratory tracts for modelling (i) cilia motion and drug diffusion in the periciliary layer (ciliated epithelium) and (ii) the release of active ingredients in powder inhalers for drug delivery in the lungs. Thanks to Discrete Multi-Physics, we advanced the state-of-the-art of multi-physics simulations in biomechanics and extended solid-liquid mechanics analyses.

Keywords: Discrete Multi-Physics, Smoothed Particle Hydrodynamics, Mass and Spring Model, Discrete Element Method, biological valve, clot-like solid, cilia, diffusivity, contact mechanics, dry powder inhaler.

1. Au nom de Dieu, le Clément, le Très Miséricordieux.

2. Louange à Dieu, Seigneur de l'univers.

3. Le Tout Miséricordieux, le Très Miséricordieux.

4. Maître du Jour du jugement.

5. C'est Toi (Seul) que nous adorons, et c'est Toi (Seul) dont nous implorons secours.

6. Dirige-nous dans le sentier droit.

7. Le sentier de ceux que Tu as comblés de bienfaits, non pas de ceux qui ont encouru Ta colère, ni celui des égarés.

Sourate Al Fatiha, l'Ouverture.

This thesis is dedicated to my family

ACKNOWLEDGEMENTS

First of all, I am thankful to Professor Mostafa Barigou and the School of Chemical Engineering at the University of Birmingham for giving me the opportunity to conduct this PhD and provide the necessary technical and financial support.

I wish to truly express my gratitude to my supervisor Doctor Alessio Alexiadis for trusting in my potential in recruiting me and guiding me throughout this thesis. I have learnt a lot from him and I have gained in confidence thanks to him. I think highly of him and without him, the thesis wouldn't be the same and not achievable at all.

This manuscript would not be possible without the total support of my family especially my wife and my children who follow me without hesitation and accept this challenge in a foreign country whose language had been unknown to them. Hopefully, their patience will be beneficial in their future, personally and professionally. Huge thanks to my mother and my father who accept our separation and have been patient during all these years. Without forgetting my brothers and my sister and their children who have always been present when the need arises.

Last but not least, special thanks to my colleagues in France: Frédéric, Hatem, Foad and Jean-Claude for their support and in Chem. Eng: Douglas, Gian, Gilmore and Saifullah for making the years of research exciting. Likewise, I don't forget Naser for his wise advice and guidance.

LIST OF PAPERS AND CONFERENCES

From the work of this thesis, the following papers have been published or submitted

- **Ariane, M**., Allouche, M. H., Bussone, M., Giacosa, F., Bernard, F., Barigou, M. and Alexiadis, A. (2017). Discrete Multi-Physics: A mesh-free model of blood flow in flexible biological valve including solid aggregate formation. Plos One, 12 (4).

- **Ariane, M**., Wen, W., Vigolo, D., Brill, A., Nash, G. B., Barigou, M. and Alexiadis, A. (2017). Modelling and simulation of flow and agglomeration in deep veins valves using Discrete Multi Physics. Computers in Biology and Medecine, 89: 96-103.

- **Ariane, M**., Vigolo, D., Brill, A., Nash, G. B., Barigou, M. and Alexiadis, A. (2017). Using Discrete Multi-Physics for studying the dynamics of emboli in flexible venous valves. Computers and Fluids. 166: 57-63.

- **Ariane, M**., Stravos, K., Velaga, S. and Alexiadis, A. (2017). Discrete Multi-Physics simulations of diffusive and convective mass transfer in boundary layers containing motile cilia in lungs. Computers in Biology and Medecine, 95: 34-42.

- **Ariane, M**., Sommerfeld, M. and Alexiadis, A. (2018). Wall collision and drug-carrier detachment in dry powder inhalers: using dem to devise a sub-scale model for cfd calculations. Powder Technology. Submitted

During this doctoral research, the findings were also presented at conferences:

- **Ariane, M**., Alexiadis, A. Smoothed Particle Hydrodynamics based modelling for blood flow in heart and vein valves. Accepted for a poster presentation at the 6th BEAR PGR Conference, Birmingham, 2015. BEST STUDENT POSTER AWARD.

- **Ariane, M**., Alexiadis, A., Barigou, M. SPH modelling of an aortic valve with flexible leaflets. Accepted for a poster presentation at the ChemEngDayUK2016 Conference, Bath, 2016.

- **Ariane, M**., Alexiadis, A., Barigou, M. Smoothed Particle Hydrodynamics (SPH) modelling of an aortic valve with flexible leaflets. Accepted for a poster presentation at the Research Poster Conference, Birmingham, 2016.

- **Ariane, M**., Alexiadis, A., Barigou, M. Flow modelling of an aortic valve with flexible leaflets. Accepted for a poster presentation at the European Society of Biomechanics ESB Conference, Lyon (France), 2016. TRAVEL AWARD.

- **Ariane, M**., Alexiadis, A., Barigou, M. Discrete Multi-Physics: a mesh-free approach for modelling the hydrodynamics in flexible biological valves including the formation of solid aggregates. Accepted for an oral presentation at the 7th Annual BEAR PGR conference, Birmingham, 2016.

- **Ariane, M**., Alexiadis, A., Barigou, M. Discrete Multi-Physics approach for modelling flexible valves and solid aggregation. Accepted for a poster presentation at the ChemEngDayUK2017 Conference, Birmingham, 2017.

- **Ariane, M**., Alexiadis, A., Barigou, M. Discrete Multi-Physics: a mesh-free approach for modelling biological valves including aggregation. Accepted for a poster presentation at the European Society of Biomechanics ESB Conference, Sevilla (Spain), 2017. CO-CHAIR INVITATION.

TABLE OF CONTENTS

LIST OF FIGURES

LIST OF TABLES

CHAPTER 1: INTRODUCTION

1.1 Computational simulations in medicine and biology

As mathematical modelling and computer simulations are becoming an increasingly valuable tool in biology and medicine, numerical studies, therefore, can provide a fundamental contribution to the full understanding of a biological system under investigation since it provides details on both the fluid and the solid dynamics. In these fields, traditional *in-vivo* and *in-vitro* models are more and more often supported by *in-silico* models to achieve a better understanding of many physiological and biomechanics problems. In the following section, we provide a brief introduction to cardiovascular and respiratory systems which are relevant to this thesis.

1.2 Cardiovascular system

The human cardiovascular system, by means of contraction movements, acts like a pump generating blood circulation in the human body and involves different complex mechanisms such as pulsatile flow, valve movements, coagulation and aggregation.

Cardiovascular diseases are responsible for 17.5 million deaths per year globally, representing 31% of all disease-related deaths including valve dysfunction and thromboembolism (Priori et al. 2015). A certain number of potential diseases can affect the valve network and, as a consequence unwanted shutting, non-closure and backflow can occur (MacIver et al. 2016). The origin of these disorders can be congenital (malformation), mechanical (under or hyper-elasticity), or physical (coagulation and aggregation) (Gottlob and May 1986).

Several *in-vivo* imaging techniques for valve disease detection are available such as the Doppler echocardiography, or the Magnetic Resonance Imaging (MRI) among others.

Doppler imaging is used for a quantification of the blood circulation (Doppler effect) and a visualisation of vascular structure (echography) in real time. However, because of manual and local acquisition (by means of probes), the snapshots are often difficult to observe and can lead to different interpretations and wrong diagnoses. MRI provides good static imaging of valve, but the technique is less effective with small and movable structures like free solid aggregate (emboli).

Among the *in-vitro* techniques accessible to quantify velocity and turbulence, the Particle Imaging Velocimetry (PIV) and the 3D Particle Tracking Velocimetry (PTV) have gained significant interest in the cardiovascular system (Gulan et al. 2012, Gallo et al. 2014). However, both measurement techniques have limitations such as limited near-wall resolution which needs to be considered while comparing with simulations.

1.3 Respiratory system

1.3.1 Respiratory epithelium

Epithelia are biological tissues with chemical glandular function (endocrine and exocrine gland) and mechanical function (epidermis and respiratory epithelium). In the case of the respiratory epithelium (trachea, primary bronchi and lungs), the mechanical function of epithelium is ensured by the presence on the surface of a number of vibrated slender protuberances (cilia) which control the pulmonary ventilation, condition the mucus airways and protect the human body against pathogens and undesired particles (D'Angelo and Franco 2009). The effectiveness of this biological line of protection in respiratory ways, called mucociliary clearance or mucociliary escalator, is mostly affected by cilia beat (metachronal wave), the chemical composition of the mucus and air surface hydration (Boucher 2007).

Under normal conditions, the synchronised cilia motion guarantees the upward circulation of the mucus toward the respiratory tract and the expulsion of the impurities trapped in the mucus via coughing or swallowing. In pathological conditions, such as a dysfunction of the cilia beat frequency or a malformation of cilia (number, position, length or motility), the cleansing is incomplete (ciliopathy) which may lead to several diseases such as chest infection or destruction of lung architecture.

With *in-vivo* procedures, the velocity of the mucus motion can be assessed. For instance, a sweet-track-component is introduced at the bottom of the trachea and the perception of taste in the larynx is correlated with the time and the ascent velocity of mucus can be evaluated (Tilley et al. 2015).

Additionally, numerous *in-vitro* techniques are available to analyse the cilia network using cultured cells. For instance, with light microscopy and electron microscopy, the structure and the length of the cilium can be evaluated (Badano et al. 2006, Leopold et al. 2009). With cine photography, the cilia beat frequency can be estimated (Marino and Aiello 1982). Whereas, with digital high-speed imaging, the cilia beat pattern can be observed (Chilvers and O'Callaghan 2000).

Despite numerous experimental techniques, the comprehension of mechanisms such as cilia beat frequency, pattern and drug diffusion remain essentially depictive especially in case of abnormalities (Tilley et al. 2015).

1.3.2 Respiratory drug delivery

Administration of medicines via inhalation is a treatment using the respiratory tract to deliver drugs into lungs by means of aerosols. There are three main types of aerosols: (i) liquid

aerosols called pressured metered dose inhalers, (ii) mist aerosols called nebulisers and (iii) dried aerosols called dry powder inhalers. In all three cases, the active ingredient, the so-called Active Pharmaceutical Ingredient (API), is administered in the form of particles (drops or solids).

Dry Powder Inhalers (DPI) are very efficient in terms of flow propulsion, but the quantity of drug delivery remains often limited to 40% (Sommerfeld and Schmalfuss 2016). One of the reasons is related to the size of the APIs. The particles should be small enough (< 5 μm) to ensure the airways are unbreathable for the patient and pulmonary particles deposit (Reychler et al. 2007). However, the small size also favours the inter-particle interaction (cohesion forces) and agglomeration (adhesion forces). Therefore, the main challenges are to optimise the design of the devices and to limit agglomeration phenomena.

In DPI, the particle dispersion is mainly controlled by the airflow turbulence and the API-wall collision in the inhaler chamber (Reychler et al. 2007). Concerning the airflow, engineers have tested different types of grids in order to increase the turbulence as well as disperse the agglomerate particles (Chan 2006, Milenkovic et al. 2014). In literature, the airflow and its influence are well known, however, the particles impact mechanics remain difficult to quantify and the involved forces such as adhesion forces or contact forces need to be better predicted.

1.4 In-silico contribution

Given the limitations of actual *in-vivo* and *in-vitro* techniques, a number of numerical studies are conducted in this thesis (see Chapter 3, 4, 5, 6 and 7). We use a methodology called the Discrete Multi-Physics (see Chapter 2) to implement computer simulations of several medical

and biological applications in cardiovascular and respiratory systems. The Discrete Multi-Physics is a fully Lagrangian technique based on a particle methodology. The choice of a discrete approach to simulate fluid dynamics, solid mechanics and contact mechanics in biological and medical fields has the following advantages:

- The absence of a grid in a mesh-free representation induces a local discretisation and avoids mesh regeneration after each iteration.

- The mesh-free framework running with no fixed connectivity is adapted for solid large deformation.

- The possibility to simulate, in non-symmetrical models, 'real' solid-solid contact without the use of additional stabilisation algorithms or 'ghost walls' between the solids.

- The sub-domains solid and fluid are not fixed and can change or invert during the simulation process.

- The nodes (particles) can easily be implemented separately and give a realistic mimic of solid elements, in particular during an oscillating flow.

- The properties are associated with notional particles allowing a direct tracking of particle motion.

- The different sub-set models share a common framework which eases their linkage to multi-physics problems.

- The Discrete Multi-Physics approach can directly account for the hydrodynamics, the solid deformation and the formation of solid aggregates at the same time.

The main limitation associated with this discrete approach remains the calculation time which is known to require more computational effort compared with traditional mesh-based methods. Moreover, other difficulties are the definition of the influence domain of each particle and the boundary conditions which should be implemented cautiously to avoid any problems of convergence and unrealistic results.

Other techniques can also be implemented for the interaction fluid/structure. In the biomedical field, the most used are the Immersed Boundary method and the Lattice-Boltzmann method.

In the Immersed Boundary method (Halevi et al. 2015), the interface between the fluid and the structure is treated as a constraint and the force exerted by the structure to the fluid becomes a source term in the momentum equation. As a result, the fluid and solid equations are solved independently. However, the Immersed Boundary method has difficulties handling phenomena such as calcification and clotting that involve some sort of transition where part of the liquid transforms into a solid.

In the Lattice-Boltzmann method (Harrison et al. 2008), fluid resolution is based on a particle collision-propagation scheme and more suitable for complex fluids such as non-Newtonian fluids and compressible fluids. Furthermore, in fluid/structure cases, the model generally assumes simple hydrodynamic conditions and/or refer to straight channels with no moving/deforming parts. Finally, breakage process cannot be handled.

1.5 Aim and objectives of the thesis

The aim of the thesis is (i) to show that Discrete Multi-Physics is a promising alternative to traditional modelling for a large variety of phenomena and (ii) to demonstrate that Discrete Multi-Physics can tackle, with relatively little effort, problems that are considered very

challenging with mesh-based multi-physics. This thesis, therefore, has the following objectives:

- To apply the Discrete Multi-Physics to biological flexible structures such as cardiovascular valves and motile ciliated tissues.
- To study fluid dynamics and solid mechanics during a complete valve cycle (opening and closing phase) and a coordinated cilia motion (metachronal wave).
- To evaluate the importance of the valve typologies such as the flexibility, the elasticity and the length on the haemodynamics, the stress and the flow stagnation.
- To implement, during the simulations, a solid formation algorithm and to investigate the impact of the solids (mobile or fixed) on the flow and the valve deformations.
- To quantify the effects of the cilia motion and the velocity flow on mass transfer process in a respiratory epithelium system.
- To investigate the release of active pharmaceutical ingredients in dry powder inhalers for drug delivery in the lungs.

1.6 Layout of the study

The thesis structure is organised into one methodology chapter and five paper-format chapters:

Chapter 2 introduces the Discrete Multi-Physics. The method is based on the combination of the Smoothed Particle Hydrodynamics, the Mass and Spring Model and the Discrete Element

Method. This chapter focuses on the methodology used in the following study chapters and also introduces specific phenomena such as solid aggregation and mass transfer.

Chapter 3 applies the Discrete Multi-Physics to cardiovascular flows and pathological conditions. In this chapter, a two-dimensional biological valve is implemented and compared with a mesh-based modelling and experimental data. Various types of aggregates are also studied such as clotting and calcification.

Chapter 4 extends the methodology to leg venous valves with different lengths, velocities, and elasticities. In this chapter, attention is given to the flow pattern and stress profiles as well as the effect of cell agglomeration behind the valve.

Chapter 5 is related to deep veins. In this chapter, a double valve system is considered and a muscle contraction boundary condition is implemented. The study focuses on fluid and emboli dynamics in the valve environment.

Chapter 6 explores the capability of the Discrete Multi-Physics for modelling mass diffusion in lung cilia. A parametric study is conducted with three variables: the velocity of the mucus, the initial concentration and the velocity of the ciliated-layer. The goal is to determine which parameter most impacts the diffusivity in the periciliary layer.

Chapter 7 presents a drug-carrier-wall collision (dry powder inhaler) model using the Discrete Element Method. The quantity of drug particles which detach from a carrier particle after a wall impact for the lung delivery is investigated. The aim is to evaluate the influence of the velocity, the rotation and the wall impact angle of the drug-carrier on the dispersion process and to suggest an analytic model.

Chapter 8 summarises all the findings and perspectives for future work.

Chapters 3, 4, 5, 6 and 7 are presented in *publication-style format chapters* according to The University of Birmingham regulation scheme. Therefore, certain sentences and description of the models can be tautological.

CHAPTER 2: THE DISCRETE MULTI-PHYSICS

2.1 Introduction

In numerical studies, the domain of differential equations can be discretised using (A) a Eulerian approach where coordinates and properties are defined in the overall system, or (B) a Lagrangian approach where coordinates and properties are defined for each local field (Fig. 2.1).

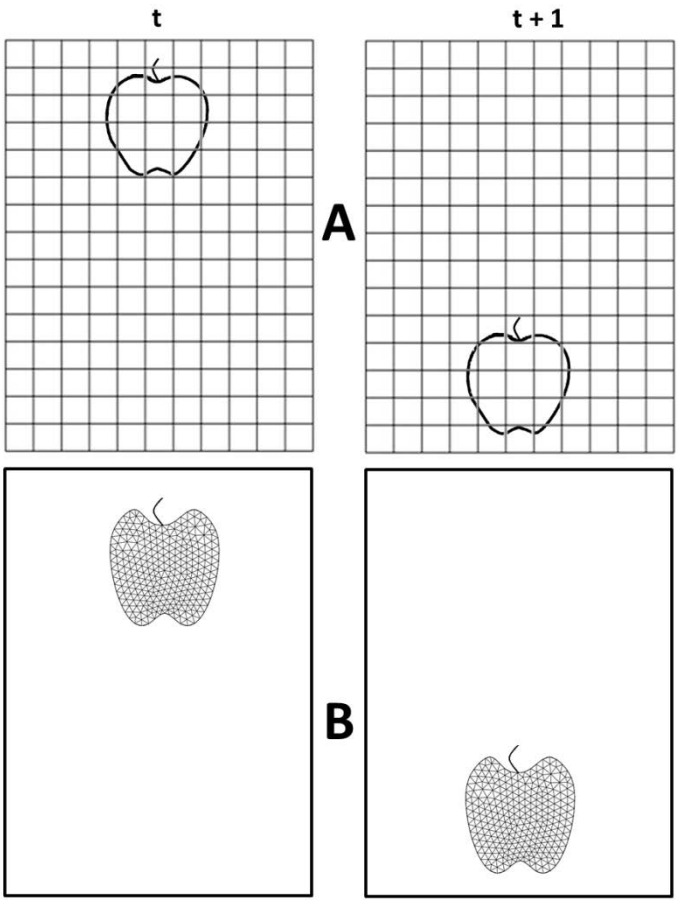

Fig. 2.1. Mesh design for Eulerian (A) and Lagrangian (B) approaches.

In the Eulerian approach (Fig. 2.1a), nodes coordinates are implemented before the simulation and the discretisation is completed in a fixed space. No movement of nodes and elements is

required. The Eulerian approach is adapted for simple geometries and fast calculations but becomes limited with complex geometries and models with high deformations.

In the Lagrangian approach (Fig. 2.1b), nodes coordinates are not fixed and change every time-step according to their spatial geometry position. The absence of a closed domain allows a better implementation and treatment of high deformations, in particular, simulation of free surface flow (Monaghan 2011).

In the case of co-simulation, the Eulerian and the Lagrangian association is traditionally considered. The Eulerian-mesh is used for the fluid and the Lagrangian-mesh is applied to the solid structure. Certain techniques such as the Arbitrary Lagrangian-Eulerian method (ALE) (Hughes et al. 1981, Simão et al. 2016, Basting et al. 2017) or the Immersed Boundary Method (IBM) (Peskin 2002, Lee and Jung 2015) are based on this association.

Independently of the method used (Eulerian or Lagrangian), the calculation codes can execute the resolution of the equations either in a field defined by a grid (mesh-based method) or in a field defined by a set of particles (mesh-free method). The choice of either one technique or both depends on applications, calculation time disposal, and convergence stability.

In mesh-based methods, the overall domain is meshed. The network consists of a set of elements linked to each other by nodes. The mesh can be regular (elements with the same size) or irregular (finer near the critical zones or the interesting sections), and the choice of the mesh size will determine the type of calculation that the programmers wish to implement: either a large mesh is chosen thus speeding-up the calculation but with potentially inaccurate results, or a fine-mesh is favoured which provides accurate results but with big memory needs and slow calculations. Therefore, attention is given to find the best compromise between calculation time and accuracy. An alternative solution consists of minimizing the size issues

with an automatic adaptive mesh refinement in the cell of interest cell as suggested by (Popinet 2003).

By contrast with mesh-based methods, mesh-free methods do not require a structured mesh for the discretisation such as with the implementation of nodes-connectivity, edges or elements. Nodes are independent, not connected with each other and can move 'freely' in the overall domain. These methods are commonly used in case of high fluid motion or large solid deformations. Mesh-free methods can be implemented using an approach based on the moving least square approximations such as the element free Galerkin method (Belytschko et al. 1994), the diffuse element method (Nayroles et al. 1992) and the HP-cloud method (Duarte and Oden 1996), or based on a particle approach such as the vortex method (Chorin and Bernard 1973, Leonard 1980), the reproducing kernel particle method (Liu et al. 1995), the particle in cell method (Harlow 1964), the molecular dynamics (Frenkel and Smit 2002) the discrete element method (Cundall and Strack 1979) or the smoothed particle hydrodynamics (Liu and Liu 2003). Other techniques are available and readers can refer to (Belytschko et al. 1996) for more details related to mesh-free methods.

2.2 Particle-based methods

In particle-based modelling, a set of particles represents the system and all particles move according to the Newtonian equation of motion (in the thesis, vectors are represented in bolt)

$$m_i \frac{d\mathbf{v}_i}{dt} = m_i \frac{d^2\mathbf{r}_i}{dt^2} = \sum_{i \neq j} \mathbf{F}_{i,j} + \sum \mathbf{F}_E, \tag{2.1}$$

with m_i is the mass of particle i, $\mathbf{v}_i$ its velocity, $\mathbf{r}_i$ its position, $\mathbf{F}_E$ the external forces, and $\mathbf{F}_{i,j}$ the internal or inter-particle forces of particle i and particle j.

To study multi-physics problems, we link together different particle methods such as the Smoothed Particle Hydrodynamics, the Mass and Spring Model and the Discrete Element Method using a common framework and algorithm structure called the Discrete Multi-Physics. The typical routine (Fig. 2.2) systematically includes the definition of the constraints and the calculation of the internal and the external forces. The different sub-models differ from each other by the representation of the internal forces.

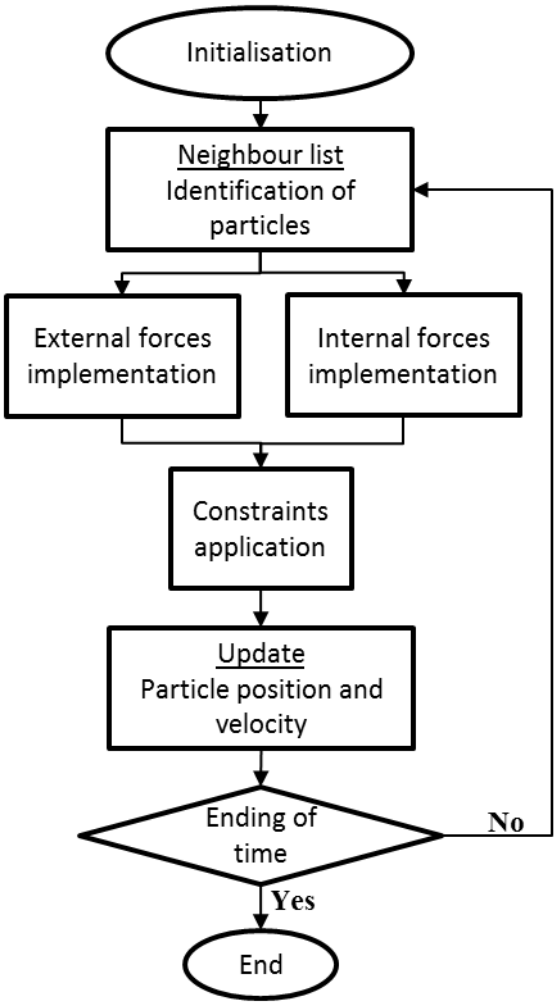

Fig. 2.2. Typical algorithm used in particle methods.

In the Smoothed Particle Hydrodynamics, the internal forces represent the viscous and the pressure forces (hydrodynamic forces). In the Mass and Spring Model, the internal forces refer to the interaction forces between two particles (deformation forces). In the Discrete Element Method, the internal forces characterise the contact between two colloid particles (collision forces).

In this thesis, the treatment of the fluid is implemented with the Smoothed Particle Hydrodynamics (Gingold and Monaghan 1977, Liu and Liu 2003), the solid structure with the Mass and Spring Model (Alexiadis 2015a), the solid contact with the Discrete Element Method (Alexiadis 2015a) and the connection solid-liquid with the Discrete Multi-Physics.

2.3 The Smoothed Particle Hydrodynamics

2.3.1 Historical background

The Smoothed Particle Hydrodynamics (SPH) is a fully Lagrangian method created initially for astro-physic problems in order to simulate gravity corps in a three-dimensional open-space (Fig. 2.3). Since its introduction by (Gingold and Monaghan 1977, Lucy 1977), areas of the application has remained limited to space study up until the 1990's. Later, SPH has been developed in fluid dynamics (Monaghan 1992, Swegle and Attaway 1995, Morris et al. 1997), in particular, with the development of free surface flow models ((Monaghan 1994) and multi-fluid problems (Monaghan 2012).

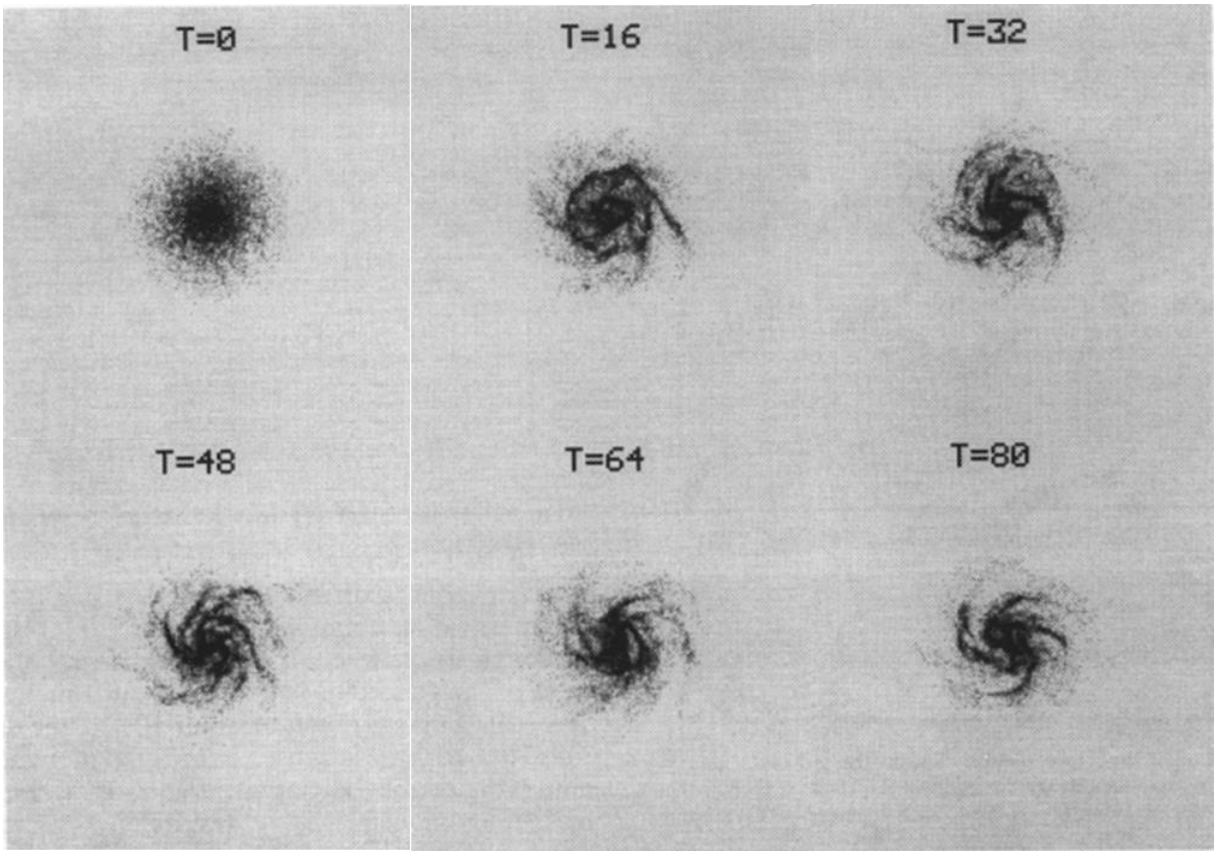

Fig. 2.3. Star formation using SPH (Mihos and Hernquist 1994).

2.3.2 Fundamentals

In SPH, equations of motion are governed by discrete approximations of the Navier-Stokes equations (Eq. (2.1)). The domain consists of a set of particles characterised by their own mass, density, pressure and velocity. Each element is defined by its position r and a generic function $f(\mathbf{r})$ over the volume V:

$$f(\mathbf{r}) = \iiint f(\mathbf{r}')\delta(\mathbf{r}-\mathbf{r}')d\mathbf{r}', \tag{2.2}$$

where $\delta(\mathbf{r}\text{-}\mathbf{r}')$ is a Dirac delta function. In SPH formalism, the delta function is approximated by a smoothing weight (or Kernel) function W which according to Monaghan (1992) is similar to a Gaussian function and satisfies the following conditions:

$$\iiint W(\mathbf{r}-\mathbf{r}', h)d\mathbf{r}' = 1 \quad \text{(normalisation condition)}, \tag{2.3}$$

$$\lim_{h\to 0} W(\mathbf{r}\text{-}\mathbf{r}', h) = \delta(\mathbf{r}\text{-}\mathbf{r}') \quad \text{(limit condition)}, \tag{2.4}$$

$$W(\mathbf{r}-\mathbf{r}', h) = 0 \quad \text{when} \quad |\mathbf{r}-\mathbf{r}'| > h \quad \text{(compact condition)}, \tag{2.5}$$

with h the characteristic length, the so-called smoothing length, which determines the size of the neighbouring domain (Fig. 2.4).

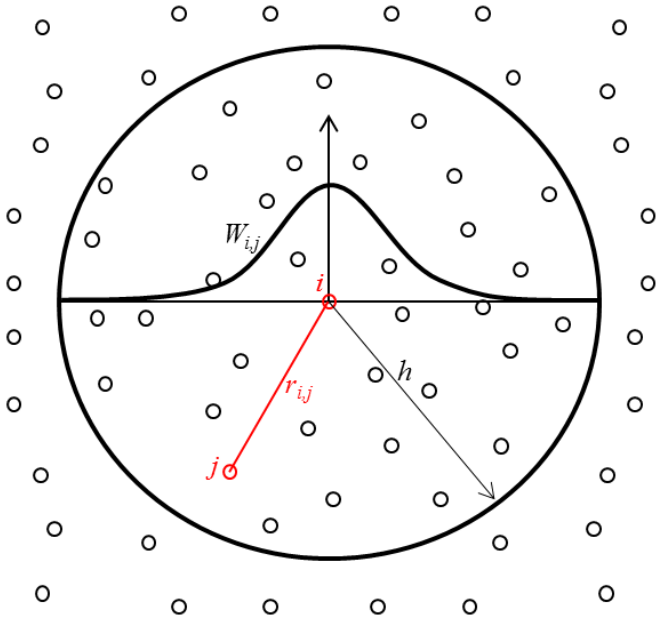

Fig. 2.4. The domain of the smoothing kernel function $W_{i,j}$ with the smoothing length h.

After interpolation, Eq. (2.2) becomes

$$f(\mathbf{r}) \approx \iiint f(\mathbf{r}')W(\mathbf{r}-\mathbf{r}',h)d\mathbf{r}'. \tag{2.6}$$

Eq. (2.6) is then discretised using a summation operator (Monaghan 1992) over a set of particles of mass $m = \rho(\mathbf{r})d\mathbf{r}$ as

$$f(\mathbf{r}) \approx \sum_i \frac{m_i}{\rho_i} f(\mathbf{r}_i)W(\mathbf{r}-\mathbf{r}_i,h), \tag{2.7}$$

where ρ_i is the density of the i^{th} particle, and i ranges over all particles within the smoothing kernel (i.e. $|\mathbf{r}-\mathbf{r}_i| < h$).

2.3.3 Smoothing kernel function

The smoothing kernel function is a key parameter in SPH since it describes the interpolation form in the neighbouring domain. Various forms of the smoothing kernel function are available in the literature such as the Lucy form (Lucy 1977), the exponential form (Gingold and Monaghan 1977), the cubic spline form (Monaghan 1992) and the quartic spline form (Morris 1996) among others. However, there is no general consensus on the most adapted smoothing kernel function. Indeed, for instance, according to Monaghan (1992), a Gaussian exponential form is the most adapted and constitutes a 'golden rule' in SPH for its stability and accuracy. Contrary to Belytschko et al. (1996) who argue that there is no significant advantage over a spline form.

In this study, we use the original Lucy kernel function (Eq. (2.8)) as it was successfully used for simulating water (Lucy 1977) and cardiovascular flows with similar geometries and same conditions (Shahriari 2011).

$$W(\mathbf{r}-\mathbf{r}_i,h)=\lambda_d\left[1+3\frac{|\mathbf{r}-\mathbf{r}_i|}{h}\right].\left[1-\frac{|\mathbf{r}-\mathbf{r}_i|}{h}\right]^3 \quad \text{for } |\mathbf{r}-\mathbf{r}_i|<h,$$
$$W(\mathbf{r}-\mathbf{r}_i,h)=0 \quad \text{for } |\mathbf{r}-\mathbf{r}_i|\geq h, \tag{2.8}$$

with $\lambda_d=5/4h$, $5/\pi h^2$ and $105/16\pi h^3$ in one, two and three dimensions, respectively.

For more details and other smoothing kernel function forms, an overview can be found in (Liu and Liu 2010).

2.3.4 Smoothing length

The smoothing length h which defines the size of the neighbouring domain is an essential parameter in SPH modelling. The smoothing length determines the quality of the calculation and the accuracy of the results. Therefore, the choice of the value must be considered cautiously. Indeed, if the smoothing length value is too small, the neighbouring domain will be represented by an insufficient number of particles and the representation will be truncated. On the other hand, a very large value of the smoothing length will negatively affect the accuracy of the calculation by smoothing out particle details and their local properties. A good compromise is usually achieved by setting a number of neighbouring particles of 5, 21 and 57 in one, two and three dimensions, respectively (Liu and Liu 2003). This number can also be increased or decreased according to the specific cases. In our simulations, to avoid any partially filled kernel, we (i) overlap fluid (SPH) and solid (MSM) particles at the boundaries,

(ii) test different values of *h* and (iii) choose, for each study case, the value of *h* which is the best compromise between accuracy and computational times.

2.3.5 Fluid dynamic equations

The discrete function (Eq. (2.1)) can be used to approximate the Newtonian equation of motion (Eq. (2.9)) and the continuity density equation (Eq. (2.10)) in a Lagrangian representation where each particle is characterised by its own mass, density, pressure and velocity

$$m_i \frac{d\mathbf{v}_i}{dt} = \sum_j m_i m_j \left[\frac{P_i}{\rho_i^2} + \frac{P_j}{\rho_j^2} \right] \nabla_j W_{i,j} + \sum \mathbf{F}_E, \tag{2.9}$$

$$\frac{d\rho_i}{dt} = \sum_j m_j \mathbf{v}_{i,j} \nabla_j W_{i,j}, \tag{2.10}$$

with P_i the pressure and $\mathbf{v}_{i,j} = \mathbf{v}_i - \mathbf{v}_j$. $W_{i,j}$ means $W(\mathbf{r}_i\text{-}\mathbf{r}_j,h)$ and ∇_j denotes the gradient of the kernel with respect of the coordinate r_j. In SPH concept, the fluid is often considered weakly compressible (+/- 1% of the reference density) or incompressible.

The density form used in Eq. (2.10) is called the continuity density. Another approximation of the density based on summation called the summation density can be used. In the summation density, the density of a particle *i* is calculated from Eq. (2.6), by simple substitution of the function $f(r)$ with density ρ

$$\rho_i = \sum_j \frac{m_j}{\rho_j} W(\mathbf{r}_{i,j}, h). \tag{2.11}$$

An artificial Tait's equation of state used by Monaghan (1994) is often implemented for simulating free surface water flow and can be used in our simulations

$$P(\rho) = \frac{c_0 \rho_0}{7} \left[\left(\frac{\rho}{\rho_0} \right)^7 - 1 \right], \tag{2.12}$$

where c_0 and ρ_0 are the sound speed and the density at zero applied stress, respectively.

2.3.6 Artificial viscosity

In the original SPH, unphysical oscillations (Monaghan and Gingold 1983) are treated by considering the energy transformation (kinetic energy into heat energy) similar to a viscous dissipation (Liu and Liu 2003). Mathematically, a viscous term $\Pi_{i,j}$, the so-called artificial viscosity, is introduced in the momentum equation (Eq. (2.9)) as

$$m_i \frac{d\mathbf{v}_i}{dt} = \sum_j m_i m_j \left[\frac{P_i}{\rho_i^2} + \frac{P_j}{\rho_j^2} + \Pi_{i,j} \right] \nabla_i W_{i,j} + \sum \mathbf{F}_E, \tag{2.13}$$

The stability of the calculation is ensured by the parameter $\Pi_{i,j}$. Various expressions are available in the literature and in this thesis, two forms are used: Morris' form (Morris et al. 1997)

$$\Pi_{i,j} = \frac{\left(\mu_i + \mu_j\right).\mathbf{v}_{i,j}}{\rho_i \rho_j \mathbf{r}_{i,j}}, \tag{2.14}$$

and Monaghan's form (Monaghan and Gingold 1983)

$$\Pi_{i,j} = -\alpha h \frac{c}{\rho_{ij}} \frac{v_{i,j}\mathbf{r}_{i,j}}{\mathbf{r}_{i,j}^2 + bh^2}, \tag{2.15}$$

where α is a parameter used to avoid high dissipation and to ensure the stability of the simulation, c is the artificial sound speed in the liquid and b is a constant introduced to avoid singularities in the case of very close particles ($b \approx 0.01$). The value of α depends on the specific type of simulation and can be calculated from the effective kinematic viscosity v for a two-dimensional representation (Macia et al. 2012)

$$v = \frac{\alpha h c}{8}. \tag{2.16}$$

2.4 The Mass and Spring Model

Molecular Dynamics (MD) is a particle method (Frenkel and Smit 2002) used in atomistic for simulating atoms and molecules movement as well as their interactions. MD is commonly associated with mesh-based methods such as the finite methods (finite volume, finite element, and finite difference) for implementing region with high inhomogeneity or region with complex features (crack soils, biological membrane deformation) but limited to a very small length scale and very short time. The Mass and Spring Model (MSM) is the coarse-grained representation of MD as a limited number of atoms is used. In previous discrete multi-hybrid system publications (Alexiadis 2014, Alexiadis 2015a), the term Coarse Grained Molecular Dynamics (CGMD) was employed. In fact, the terms MSM and CGMD are interchangeable and depend on the fact that these articles cover different scales. Articles dealing with microscopic scales use CGMD, whereas articles dealing with macroscopic scales use MSM. Mathematically, however, the two techniques are equivalent and, in this thesis, MSM is

preferred, which is more consistent with the scale under investigation. The atomic motion is classically represented by a Newtonian equation of motion

$$m_i \frac{d^2\mathbf{r}_i}{dt^2} = -\frac{\partial}{\partial \mathbf{r}} U_{tot}(\mathbf{r}_1, \mathbf{r}_2, ...\mathbf{r}_N) + \sum \mathbf{F}_E, \tag{2.17}$$

where U_{tot} is the total inter-atomic potential. The negative gradient is associated with the inter-particle force $\mathbf{F}_{i,j}$ (Eq. (2.1)). The total inter-atomic potential U_{tot} represents the sum of intermolecular potential and non-bonded potential. Non bonded potentials are represented by attractive and repulsive forces (section 2.6.2). Intermolecular potentials can be divided as

$$U_{\text{intermolecular}} = U_{bond} + U_{\text{angle}} + U_{dihedral} \tag{2.18}$$

where U_{bond} is the bond potential, U_{angle} is the angular potential and $U_{dihedral}$ is the torsional potential. Various forms of potential are available in the literature and the one used in this thesis is the harmonic form,

$$U_{bond} = k_b (r - r_0)^2, \tag{2.19}$$

with k_b is the Hookean coefficient and r_0 is the initial distance,

$$U_{angle} = k_a (\theta - \theta_0)^2, \tag{2.20}$$

with k_a is the angular Hookean coefficient and θ_0 is the initial angle,

$$U_{dihedral} = k_d(\phi - \phi_0)^2, \tag{2.21}$$

with k_d is the torsional Hookean coefficient and ϕ_0 is the dihedral initial angle.

Eq. (2.19) is commonly used to create a cohesion force between two atoms with an initial distance r_0 and is similar to stretching. Eq. (2.20) consists of three atoms maintained with a reference angle θ_0 and is similar to bending. Eq. (2.21) generates a specific dihedral angle ϕ_0 among four atoms and is similar to torsion. These three potentials constitute the molecular origin form of MSM (Fig. 2.5).

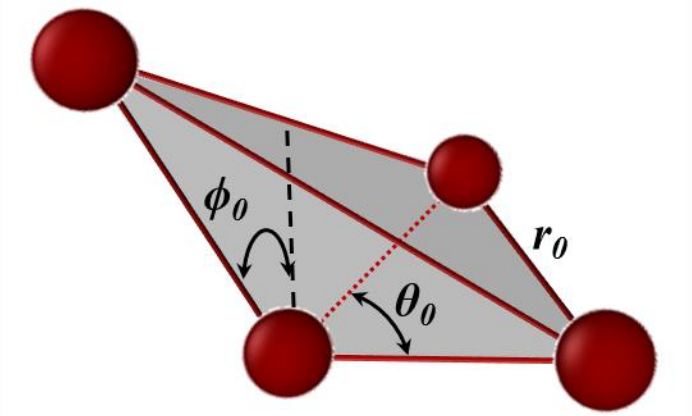

Fig. 2.5. Standard Hookean coefficient used with harmonic potential in MSM.

From the Molecular origin form, various mechanical properties can be easily implemented as illustrated in Fig. 2.6. For instance, bond potential can be used to represent elastic modulus (spring), solidification (bond formation) and melting (bond breaking). By associating bond potential with angular potential, shear modulus (rigidity) and bending modulus (hinge) can be added.

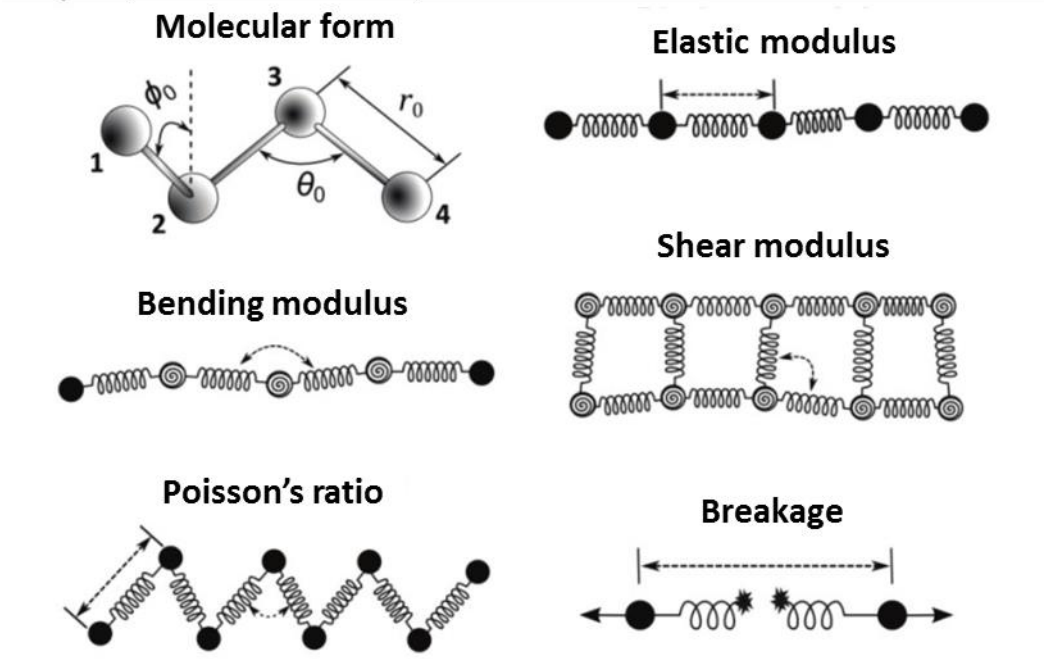

Fig. 2.6. Solid mechanics adapted to coarse-grain modelling (Alexiadis 2015a).

Frictional interaction can also be implemented by applying a damping force to the particles

$$F_{friction} = -k_v v_i, \tag{2.22}$$

where k_v is the viscous damping coefficient and v_i is the velocity of the particle i. The frictional force confers a viscoelasticity to the selected particles as a Kelvin-Voigt material.

2.5 The Discrete Element Method

The Discrete Element Method (DEM) is a particle method initially introduced for rock mechanics (Cundall and Strack 1979) and then extended to granular flows (Thornton and Yin 1991). The motion and the trajectory of the DEM particles (called 'grains') are also determined by the Newtonian equation of motion (Eq. (2.1)). The internal forces $F_{i,j}$ in Eq. (2.1) are defined by the contact forces resulting from the collision of two particles.

These forces can be decomposed into the normal forces and the tangential forces. There is a variety of contact force models in the literature, in this thesis, the Hertzian model is used (Zhang and Makse 2005)

$$f^n = \sqrt{\delta}\sqrt{R_{eff}}(k_n\delta - m_{eff}\gamma_n v_n), \tag{2.23}$$

$$f^t = -\sqrt{\delta}\sqrt{R_{eff}}(k_t\xi + m_{eff}\gamma_t v_t), \tag{2.24}$$

where f^n and f^t are the normal contact forces and the tangential contact forces, $R_{eff} = R_iR_j/(R_i+R_j)$, is the effective radius of the colliding particles i and j with radius R_i *and* R_j, k_n and k_t are the stiffness constants, δ and ξ are respectively, the overlap and the displacement between 2 particles in the normal and the tangential direction, γ_n and γ_t are respectively, the tangential and normal damping coefficients and $m_{eff} = m_im_j/(m_i+m_j)$ is the effective mass of 2 colliding particles with mass m_i and m_j.

2.6 Coupling SPH-MSM-DEM: the Discrete Multi-Physics

In this thesis, solid-liquid systems involve three main categories: fluid dynamics, solid mechanics, and contact forces. The three categories constitute a multi-physics problem, called the Discrete-multi-Physics (DMP), and, as explained in Section 2.2, can be implemented with the regulation of the internal forces (Eq. (2.1)) in the common paradigm of SPH, MSM and DEM. This specificity eases the linkage among the sub-set models as illustrated in Fig. 2.7. In this example, the fluid is represented by SPH particles, the solid is structured by MSM interactions and the contact between the two squares is implemented by DEM forces. The

system is, therefore, defined by four types of interactions. Type 1 is the interaction liquid-liquid SPH particles and relates the viscous and the pressure forces (Eqs. (2.9) and (2.10)). Type 2 is the interaction solid-solid MSM particles and links each particle by means of bonds (Eqs.(2.19), (2.20) and (2.21)). Type 3 is the DEM contact interaction between the two squares in the event of a collision (Eqs.(2.23) and (2.24)). Type 4 is the interaction liquid-solid at the solid interface. This latter type defines the boundary conditions such as no penetration and no-slip condition (detailed in section 2.6.2).

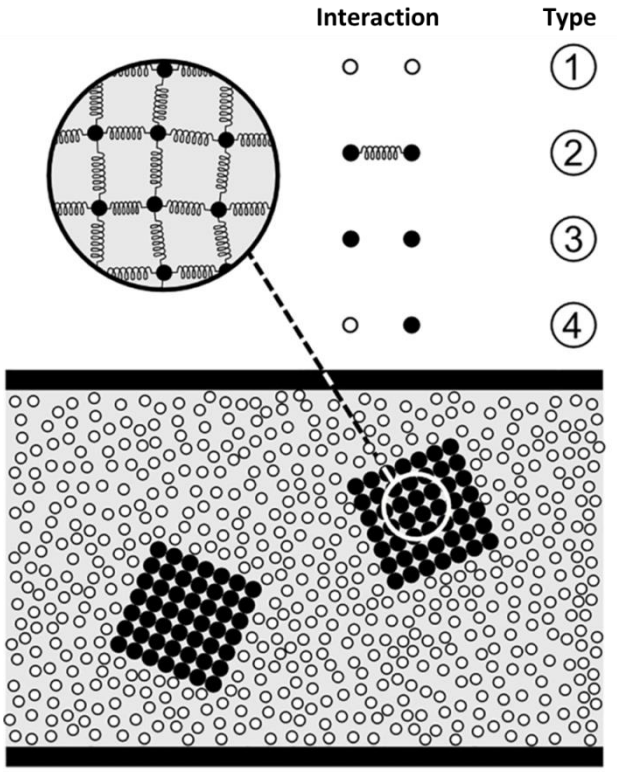

Fig. 2.7. Type of inter-particles interaction of cubic solids and fluid motion in a channel (Alexiadis 2015a).

2.6.1 Initial particle distribution

Particle distribution can be generated with a programming code or a pre-processing solver. In the first case, the coordinates of the points are created with a separate standard programming

code such as C++ and MATLAB, or directly in the processing solver with an integrated algorithm (in the software LAMMPS for instance). For complex geometries, a pre-processing commercial builder (GAMBIT, ABAQUS, SALOME) can be used for the structure and the associated mesh is then replaced with particles (Fig. 2.8).

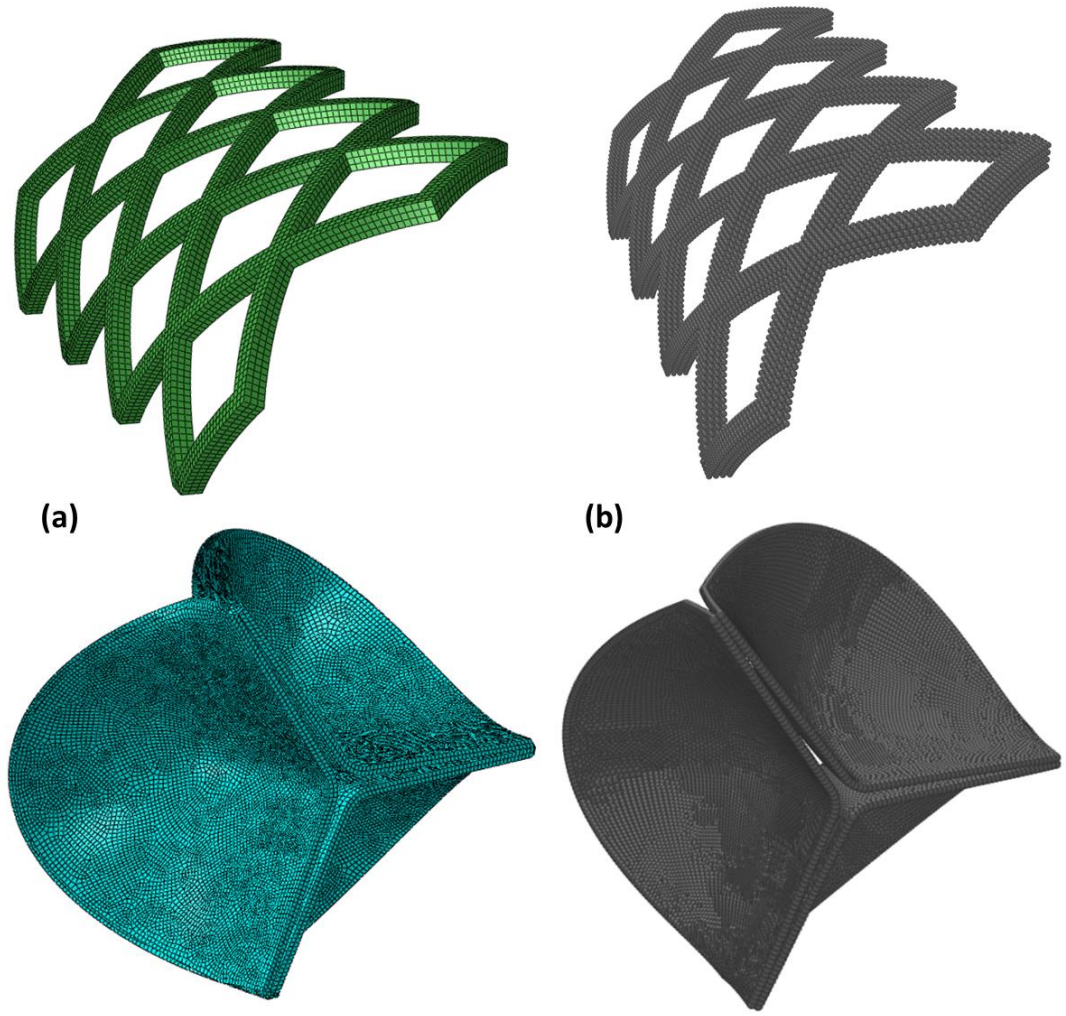

Fig. 2.8. Mesh generation using a pre-processing solver (a) and the generated particle distribution (b).

2.6.2 Solid boundary conditions

In particle methods, boundary conditions between solid particles and liquid particles are implemented by means of interaction forces. These forces define the behaviour of the two distinct materials at the liquid-solid interface. Three types of conditions are accounted for: no-penetration, no-slip, and continuity of stresses (Müller et al. 2004)

$$(\frac{\partial}{\partial t}\mathbf{u} - \mathbf{v}) \cdot \mathbf{n} = 0 \ \text{(no - penetration)}, \tag{2.25}$$

$$(\frac{\partial}{\partial t}\mathbf{u} - \mathbf{v}) \times \mathbf{n} = 0 \ \text{(no - slip)}, \tag{2.26}$$

$$\sigma_s \mathbf{n} = \sigma_f (\mathbf{-n}) \ \ \text{(continuity of stress)}, \tag{2.27}$$

with **u** the displacement of the solid, **v** the velocity of the liquid, **n** the normal to the boundary, σ_s and σ_f the stresses in the solid and in the fluid respectively. With the no-penetration condition, no mixing between two different phases is ensured. With the no-slip condition, the friction between the solid and the fluid is related. The continuity of stress is automatically satisfied by Eq. (2.1).

In finite-element methods, the same velocity is imposed at the solid-liquid interface for the two materials in order to enforce the no-penetration and no-slip conditions. While in the DMP framework, interaction forces are used (Ferrand et al. 2013).

2.6.2.1 Repulsion interactions

The repulsion interaction is implemented by means of a Lennard-Jones type potential often used in particle methods. It can be used between two liquid particles or between a liquid

particle and a solid particle. A particle approaching another particle is repulsed by a force defined as a function of a distance r,

$$f(r) = K\left[\left(\frac{r^*}{r}\right)^{n_1} - \left(\frac{r^*}{r}\right)^{n_2}\right]\frac{\mathrm{r}}{r^2}, \tag{2.28}$$

with r^* the radius of repulsion of the particle and K a constant defined according to the characteristic of the velocity flow. The exponents n_1 and n_2 are usually set to 4 and 2 for liquid-liquid particles and 12 and 6 for liquid-solid (Lennard-Jones potential) (Monaghan 1994).

2.6.2.2 Fixed particles

In the fixed particle approach, the time integration is performed every time-step for the local density but not for the position and the velocity of particles. Therefore, the particles are stationary and define the rigid solid wall. In addition, two or three layers of wall particles can be added successively to avoid any fluid penetration (Violeau and Issa 2007).

2.7 Solid aggregation algorithm

With DMP, phenomena such as solid aggregation can be implemented with a relative effort. Indeed, mathematically, the difference between a fluid SPH particle and a solid MSM particle is the use of interaction forces (bond, angle, repulsion, attraction, etc..) and can be achieved by changing the forces acting on certain particles from SPH to MSM. In Chapters 3 and 4, a

solid aggregation scheme is used (Fig. 2.9) and summarized here (specific applications are detailed in Chapter 3).

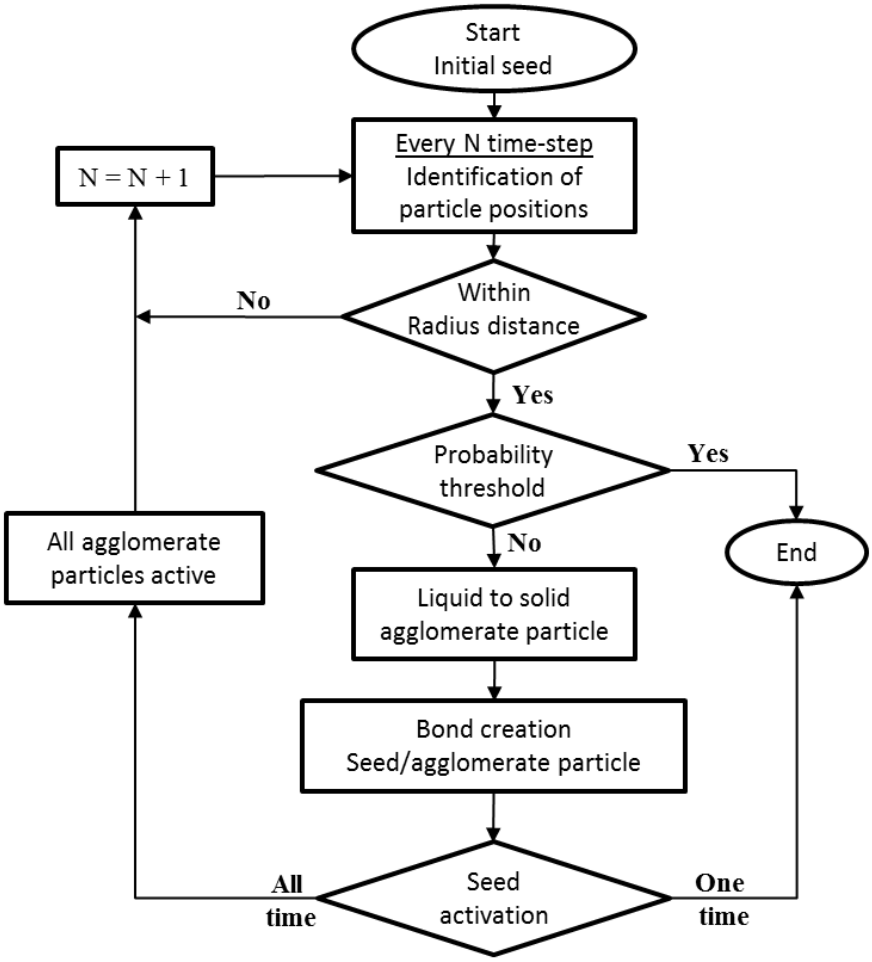

Fig. 2.9. Solid aggregation scheme.

Before the simulation, a particle (fluid or solid) is selected to represent the initial seed, a radius distance of interaction *Rmax* is defined and a threshold of probability is chosen. During the simulation, in the first step, all particle positions are scanned by the algorithm. If a fluid particle is within *Rmax*, the particle is changed to a solid particle and a bond is created between the seed and the new solid particle (Fig. 2.10). The scan is then repeated every *N* time-step and the algorithm is activated according to the probability (Fig. 2.9). If the seed and

the new solid particles are active all the time, the agglomeration process is applied to all particles around them. If the seed and the new-solid particles are active one-time, the agglomeration process is only applied to the last new created particle.

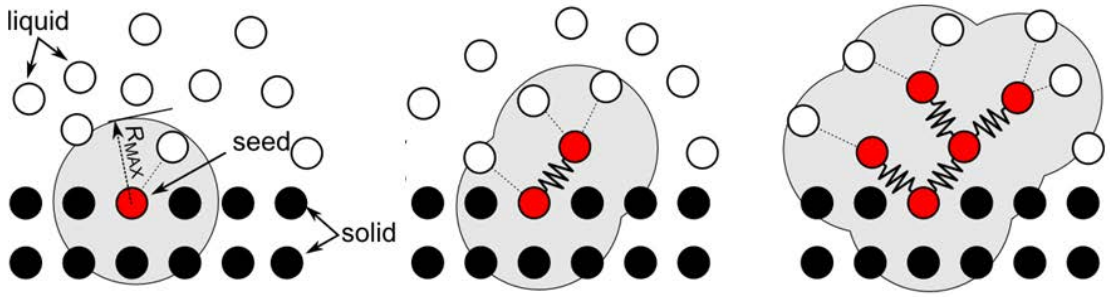

Fig. 2.10. Mechanism of solid formation.

2.8 Mass transfer

Mass transfer, in multicomponent systems, can be included in DMP using the SPH framework (Chapter 6). In order to simulate the variation of the concentration of a species A, an elemental concentration is added to each individual particle by writing the diffusive mass balance (Alexiadis 2015a) in SPH framework

$$\frac{dw_i}{dt} = -\sum_j \frac{m_i m_j}{\rho_i \rho_j} \frac{(D_i + D_j)(C_i + C_j)}{r_{i,j}^2} \mathbf{r}_{i,j} \cdot \nabla_i W_{i,j}, \tag{2.29}$$

where w_i is the mass of fluid, D is the diffusion coefficient of particle i and C is the concentration. Each SPH particle is now characterised by its position, its velocity and its concentration (Alexiadis 2015a).

In order to close Eq. (2.29), we link m_i, C_i and ρ_i

$$w_i = C_i \frac{m_i}{\rho_i}. \tag{2.30}$$

2.9 DMP and other hybrids unifications

Coupling fluid dynamics and solid mechanics can be also implemented with other hybrid models with their specific advantages and limitations such as SPH-MD, SPH-DEM and SPH-SPH.

With the SPH-MD hybrid model, the system is divided into two distinct domains: SPH fluid particle with a characteristic smoothing length *h* and MD solid particle with a characteristic distance *r*. The solid MD structure is implemented using interaction forces such as Lennard Jones pair potential as explained in section 2.4. The interface can be treated in the SPH domain (overlap region) or associated with the MD domain. Contrary to the unique DMP domain, the SPH-MD use different domains with different time and length scales making the co-simulation more complicated.

In SPH-DEM unification, each sub-model shares the same domain. Therefore, SPH field applications can be extended to solid-liquid mechanics (Wu et al. 2016) but remain not applicable for phenomena such as solidification, melting and breakage without MSM. Moreover, with the use of elemental particles in DEM, mesoscale simulation cannot be considered.

A full SPH representation can also be used for both solid and liquid (Gray et al. 2001, Lobovsky and Kren 2007). In this case, an artificial stress using a similar approach of an artificial viscosity (see section 2.3.6) is added. The solid SPH representation can be adapted for simulating solid structures with elasticity such as oscillating beams, colliding rings or

elastic solid (Gray et al. 2001, Monaghan 2012) but not adapted for accounting for phenomena of contact mechanics, agglomeration and granular flow (Alexiadis 2015a). Additionally, using MSM rather than SPH for the solid structure, we have a wider choice of inter-particle potentials and, therefore, more phenomena can be accounted for. Indeed, the SPH method is based on pair potential-interactions between computational particles. Using MSM approach, we can introduce many-body potentials when necessary. For example, in this work, we use the angle potential that is a three-body potential.

2.10 Summary

In this chapter, an overview of the methodology used in this study is presented. The description of the mathematical concepts of the SPH, MSM, DEM and DMP are detailed. These concepts include the smoothing kernel, the discrete equations, the interaction potentials, the contact mechanics and the liquid-solid boundary conditions among other mesh-free characteristics. Specific phenomena related to solid aggregation and mass transfer are also summarised.

2.11 Notation and abbreviations

Notation

m	Mass, kg
v	Velocity, m s^{-1}
r	Distance, m
t	Time, s
F_E	External forces, N
$F_{i,j}$	Internal or inter-particle forces, N
P	Pressure, Pa
ρ	Density, kg m^{-3}
V	Volume, m^3
h	Smoothing length, m
W	Kernel function, m
e	Energy, J
τ	Viscous stress tensor, Pa
μ	Constant dynamic viscosity, Pa s
Π	Artificial viscosity, Pa s

c	Artificial sound speed, m s^{-1}
U	Interatomic potential, J
k_b	Bond Hookean coefficient, J m^{-2}
r_0	Initial distance, m
k_a	Angular Hookean coefficient, J
θ_0	Initial angle, rad
k_d	Torsional Hookean coefficient, J
ϕ_0	Dihedral initial angle, rad
k_v	Viscous damping coefficient, kg s^{-1}
u	Displacement, m
σ	Stress, Pa
f^n	Normal contact force, N
f^t	Tangential contact force, N
k_n, k_t	Stiffness constant coefficient, N m^{-1}
γ	Dumping coefficient, s^{-1}
δ	Overlap between two particles, m
ξ	Tangential displacement between two particles, m

R_{eff}	Effective radius, m
Rmax	Maximum particle distance, m
w	Mass of fluid, kg
D	Diffusion coefficient, $m^2\ s^{-1}$
C	Concentration, $kg\ m^{-3}$

Abbreviations

DDPE	Discrete Differential Partial Equations
CFD	Computational Fluid Dynamics
ALE	Arbitrary Lagrangian Eulerian
IBM	Immersed Boundary Method
FSI	Fluid Structure Interaction
FV	Finite Volume
FE	Finite Element
MD	Molecular Dynamics
DEM	Discrete Element Method
SPH	Smoothed Particle Hydrodynamics
CGMD	Coarse Grained Molecular Dynamics

DMP	Discrete Multi-Physics
LES	Large Eddy Simulation
RSM	Reynolds Stress Model
EARSM	Explicit Algebraic Reynolds Stress Model
LANS	Lagrangian Averaged Navier-Stokes
FENE	Finite-Extensible Non-linear Elastic

CHAPTER 3: TWO-DIMENSIONAL VALVE MODELLING INCLUDING CALCIFICATION AND CLOTTING

3.1 Abstract

A mesh-free and discrete (particle-based) multi-physics approach is proposed for modelling the hydrodynamics in flexible biological valves. In the first part of this study, the method is successfully validated against both traditional modelling techniques and experimental data. In the second part, it is further developed to account for the formation of solid aggregates in the flow and at the membrane surface. Simulations of various types of aggregates highlight the main benefits of Discrete Multi-Physics and indicate the potential of this approach for coupling the hydrodynamics with phenomena such as clotting and calcification in biological valves.

3.2 Introduction

Computational fluid dynamic (CFD) simulations of biological valves have steadily improved over the years; however, procedures accounting for the formation of actual solid aggregates, such as calcifications or clots, have not been implemented yet. At the same time, researchers have also devised mathematical models for clot formation and growth; however, these models have been developed independently and are not usually associated with the dynamics of the valve. A particle-based method is proposed that, by taking advantage of its mesh-free nature, can compute the fluid dynamics, together with valve deformation and formation of solid aggregates.

In general, the simulation of biological valves, where a solid structure interacts with the surrounding flow, constitutes a fluid-structure interaction (FSI) problem. The algorithms to solve FSI problems may be broadly classified into two categories (Hou et al. 2012): conforming mesh methods (Fig. 3.1a) and non-conforming mesh methods (Fig. 3.1b). Conforming mesh methods (Marom 2015) divide the computational domain into two parts: (i) a part occupied by the liquid where the Navier-Stokes equations are solved, and (ii) a part occupied by the structure where the stress-deformation equations are solved. Since the structure moves and/or deforms with time, re-meshing is needed as the solution advances. Non-conforming mesh methods, most notably the Immersed Boundary Method (IBM) (Halevi et al. 2015), treat the interface between the fluid and the structure as a constraint and the force exerted by the structure to the fluid becomes a source term in the momentum equation. As a result, the fluid and solid equations are solved independently and re-meshing is not necessary. Both methods, however, have difficulties handling phenomena such as calcification and clotting that involve some sort of transition where part of the liquid transforms into a solid. In

general, attempts to account for the formation of solid aggregates in CFD/FSI studies are based on 'numerical artifices' such as fluids with higher viscosities to mimic clotting (Narracott et al. 2005), or membranes with higher stiffness to mimic calcification (Keijsers et al. 2015).

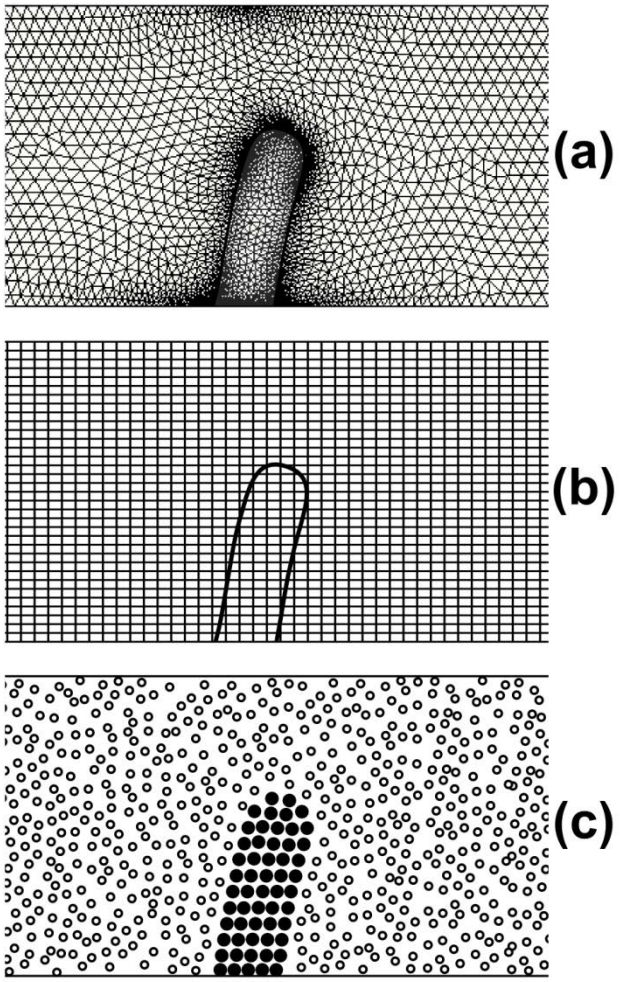

Fig. 3.1. FSI algorithms: (a) conforming mesh, (b) non-conforming mesh, (c) mesh-free.

On the other hand, modelling of clot formation and growth had followed an independent path that, in some cases, has brought to particle-based techniques such as the Lattice-Boltzmann method (Harrison et al. 2008) or the Coarse Grained Molecular Dynamics (Bajd and Sersa 2013). In general, however, these models assume simple hydrodynamic conditions and/or

refer to straight blood vessels with not moving/deforming parts. Additionally, coupling fluid dynamics and solid deformation can be implemented with the Smoothed Particle Hydrodynamics method (Gray et al. 2001, Lobovsky and Kren 2007). But, it can't easily account for other phenomena such as contact mechanics and agglomeration.

In order to account for the fluid dynamics, the valve deformation, and the formation of solid aggregates at the same time, Discrete Multi-Physics (DMP): a mesh-free approach is proposed, where computational particles are employed for both the flow and the structure (Fig. 3.1c). With this method, the distinction between liquid and solid depends exclusively on the types of forces that act on each particle: pressure and viscous forces characterise liquid particles, while elastic forces characterise solid particles. By changing the type of forces on specific groups of particles, we can change their status form liquid to solid and vice versa. In (Alexiadis 2015a), this idea is used to model melting and solidifying flows; in this study, we extend it to the formation of agglomerates in biological valves.

This chapter is organised as follows. Initially, we discuss the basic ideas behind the Discrete Multi-Physics technique and describe the geometry used in the simulations. Next, we validate the model against both traditional modelling techniques and experimental data. Finally, we introduce the formation of solid aggregates at the membrane surface and in the flow.

The objective of this work is to apply DMP to biological valves in general. For this reason, we do not focus on a specific type of valve at this stage. However, in order to test our model in the most challenging scenario, we chose dimensions and velocities similar to those occurring in aortic valves. We consider these conditions to be the most challenging scenario because (i) they involve higher velocities, which generate complex recirculation patterns (see section 3.4), and (ii) they involve higher stresses, which generate larger membrane

deformations (see section 3.4). From this point of view, the fact that we simulate bicuspid valves, while the aortic valve has three leaflets, is not a limitation. Given the same mechanical stress, in fact, deformations are higher in bicuspid valves than in tricuspid valves (Bavo et al. 2016). Therefore, by forcing velocities that are typical of aortic valves in bicuspid valves, we test our model under conditions that are even more critical (i.e. produce higher deformations) than those occurring in aortic valves.

3.3 Methodology

3.3.1 Modelling

Our Discrete Multi-Physics approach is based on the so-called discrete Multi-Hybrid System (DMHS). This technique combines various mathematical models to achieve a representation of fluid-structure interactions and solid-liquid systems that is not attainable with each model separately. Elsewhere (Alexiadis 2014), we showed that the linkage of different models is mathematically complex and computationally time-consuming. In order to facilitate this, the DMHS combines models that share a common discrete (particle-based) paradigm, such as the Smoothed Particle Hydrodynamics (SPH), Mass and Spring Model (MSM), the Discrete Element Method (DEM) or the Brownian Dynamics (BD).

In this study, models for solid contact/collision (i.e. DEM), or for fluctuating hydrodynamics (i.e. BD) are not necessary; consequently, the coupling is limited to SPH (liquid phase) and MSM (solid phase). For the numerical solution, the model was implemented in LAMMPS (Plimpton 1995). Specific details of the DMHS and other mesh-free hybrid techniques can be found in (Alexiadis et al. 2014, Alexiadis 2015a, Alexiadis 2015b, Liu and Liu 2016, Alexiadis et al. 2017).

3.3.2 Geometry

A two-dimensional simplified geometry is used for modelling a generic bicuspid valve as illustrated in Fig. 3.2. The channel half-thickness is $Z = 0.0125$ m, the length of the membrane is $L = 0.016$ m and the radius of the circular area is $R = 0.0215$ m.

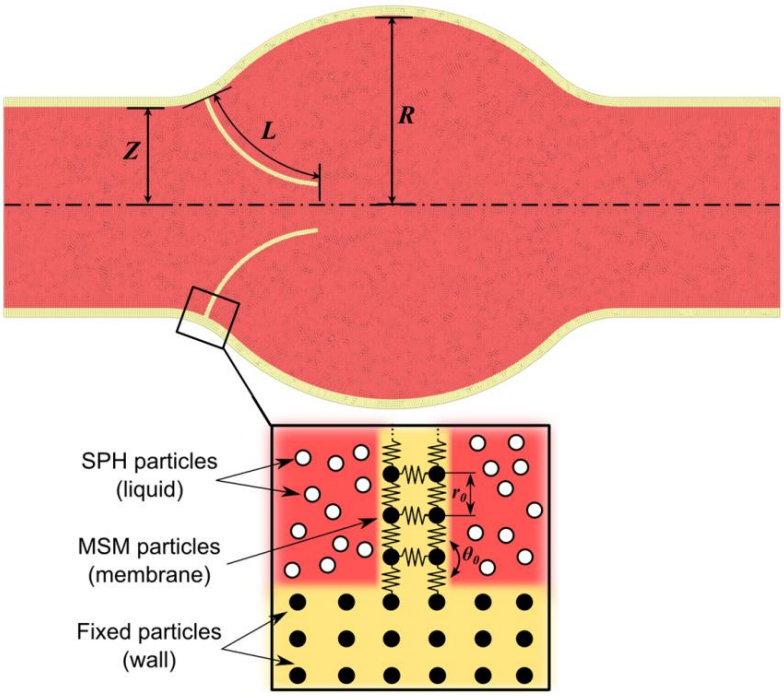

Fig. 3.2. Valve geometry and types of particles used in the simulations.

As mentioned above, DMP combines various particle-based modelling techniques. In this study, the simulations are based on two models and three types of particles: SPH particles for the fluid, fixed SPH particles for the walls and MSM particles for the flexible leaflets (membrane).). The initial spatial distribution of the fixed SPH particles and the MSM particles is regular as shown in Fig. 3.2, while the initial spatial distribution of the fluid SPH particles is generated automatically and randomly with a pre-processing meshing software (Abaqus 6.14). In both cases, the initial spacing among particles Δr is equal to 2.5 10^{-4} m (Table 3.1).

Periodic boundary conditions are used at the inlet/outlet. To model the Young modulus E and the flexural rigidity F of the membrane, the MSM particles are joined together by numerical 'springs' and 'hinges', as described in Chapter 2. The relation between the spring (k_b) and hinge (k_a) constants and the actual Young modulus and the flexural rigidity is given in section 3.3.4.

3.3.3 Pulsatile flow

In order to test the model in the most critical conditions, we target high velocities typical of cardiac valves such as the aortic valve. The flow is pulsatile and corresponds to a normal cardiac output of 5.5 L min^{-1}, a beat rate of 72 bpm and an aortic pressure of 100 mmHg. This frequency gives a peak velocity of around 0.9 m s^{-1}. In the simulation, we force the flow by means of a sinusoidal pressure P gradient

$$\frac{dP}{dx} = A\sin(\frac{2\pi}{T}t), \tag{3.1}$$

where A is the force amplitude and T the period. To obtain this pressure gradient in the simulations, we impose to each liquid particle the acceleration

$$g = g_0 \sin(2\pi ft), \tag{3.2}$$

with g_0 = 500 m s^{-2} and oscillation frequency $f = 1/T$ (T = 1 s). Under these conditions, we reach high velocities but the flow remains laminar. We focus on the laminar regime for two reasons: (i) blood flow under normal conditions is laminar, and (ii) we want to test, at this stage, the accuracy of our model without dealing with the additional complexity of turbulence.

3.3.4 Solid mechanics

The mechanical properties of structures simulated with MSM potentials are the constants k_a (Eq. (2.19)), k_b (Eq. (2.20)) and k_d (Eq. (2.21)) used in MD-like potentials. The mechanical properties of a real material, however, are measured by means of macroscopic properties such as the elastic modulus E, the flexural rigidity F and the torsional rigidity T (not used in this thesis). In order to compare the calculations with the experimental works, a relation to link k_a and k_b with E and F is necessary. In our case, since no torsional and shear stress are considered, k_a and k_b can be defined as (Scarpa et al. 2010)

$$k_a = 4\frac{EI}{L}, \tag{3.3}$$

and

$$k_b = \frac{EM}{L}, \tag{3.4}$$

where E is the elastic modulus, $I = wd^3/12$ is the moment of inertia, $M = wd$ the cross-section, w the width of the structure and d its thickness. In the particle framework, the membrane has an equivalent thickness d that, combining Eqs. (3.3) and (3.4), can be calculated by

$$d = \sqrt{3\frac{k_a}{k_b}}. \tag{3.5}$$

Using this value of d, we can calculate I and M, subsequently E from Eq. (3.4), and finally $F = EI$ from Eq. (3.3).

3.3.5 Dimensionless analysis

In Section 3.4.2, we compare our simulations with experimental data. The comparison is based on specific dimensional groups that are defined in this section.

Dimensional analysis bring to three fundamental groups *Re* (Reynolds Number), N_f (dimensionless frequency) and Λ (geometric ratio), defined as

$$Re = \frac{\rho U Z}{\mu}, \tag{3.6}$$

$$N_f = \frac{\rho f^2 d^5}{F / L}, \tag{3.7}$$

and

$$\Lambda = \frac{Z}{L}, \tag{3.8}$$

where ρ is the density of the fluid, U is a reference velocity (here we use the max velocity in the channel), μ the fluid viscosity, d the membrane thickness. The computational particles used in our simulations are point particles; strictly speaking, they do not have an actual thickness. Their thickness is the result of the repulsive forces acting on the particles to impose no-penetration boundary conditions (see Chapter 2). The value of d in Eq. (3.7), therefore, is calculated from k_a and k_b as discussed in section 3.3.4. The value of the Young modulus E does not compare explicitly to any of the dimensionless numbers above; this is due to the fact that F and E are interchangeable as discussed in section 3.3.4. In theory, we should also account for another dimensionless group based on R (radius of the circular area in Fig. 3.2). In practice, however, this group is not necessary as discussed in Section 3.4.2.

Each dimensionless number provides specific information about the geometric constants and the physical forces acting in the system. *Re* indicates the extent of the inertial forces with respect to the viscous forces. N_f indicates the membrane resistance with respect to the stress generated by the oscillating flow. Λ indicates the geometric ratio between the channel thickness and the membrane length. In comparing the simulations with the experimental data (see Section 3.4.2), we found that the group

$$N_R = Re.N_f = \frac{\rho^2 f^2 d^5 UZ}{\mu F / L} \tag{3.9}$$

is particularly relevant. This dimensionless number compares the effect of the forces that tend to deform the membrane (numerator) with those that tend to oppose the deformation (denominator). In Section 3.4.2, we show that different geometries and flow conditions generate the same type of membrane deformation if N_R is the same.

3.4 Results and discussion

There are two types of parameters required for the simulations: model parameters and simulation parameters. The first group consists of internal parameters used by the SPH and MSM solvers; the second refers to the operative conditions. This Section focuses on the second group (i.e. Z, L, R, μ, ρ and F); the internal parameters (e.g. k_a, k_b, number of particles, time step, smoothing length, etc.) can be found in Table 3.1.

In Table 3.1, the initial distance between particles is in accordance with similar geometries (Shahriari et al. 2012) and ensures a realistic contact between the two leaflets during the closing phase. The value of h reflects the best compromise between accuracy and computational times and avoids any partially filled kernel during the simulations. Finally, for

all simulations, we consider a fix time-step in order to ease the interaction between each sub-model (SPH and MSM).

The geometric parameters L, Z, R are given in section 3.3.2 (see also Fig. 3.2). All the simulations assume blood as a liquid medium. Blood is a viscoelastic fluid, but in flow simulations (Hosseini and Feng 2009, Sinnott et al. 2012, Bavo et al. 2016) is often considered Newtonian. In our calculations, we also use the Newtonian approximation with ρ = 1056 kg m^{-3} and μ = 0.0035 Pa s. We consider membranes with different flexural rigidities, the specific value of F, for each case, is given in section 3.4.2 (Table 3.2).

This section is divided into three parts. The first part is dedicated to the flow, and we validate our results against traditional CFD simulations. The second part is dedicated to the membrane, and we validate our results against experimental data. The third part focuses on the formation of solid aggregates and highlights the main advantages of the DMP in modelling biological valves.

Table 3.1. Model parameters used in the simulations.

SPH (Eqs.(2.12), (2.13), (2.15))	
Parameter	**Value**
Number of SPH wall particles (4 layers)	3262
Number of SPH valve particles (2 layers)	272
Number of SPH fluid particles	49224
Mass of each particle (fluid)	$6.6 \cdot 10^{-5}$ kg
Mass of each particle (wall and valve)	$12 \cdot 10^{-5}$ kg
Initial distance among particles Δr	$2.5 \cdot 10^{-4}$ m
Smoothing length h	$6.25 \cdot 10^{-4}$ m
Artificial sound speed c_0	27 m s^{-1}
Density ρ_0	1056 kg m^{-3}
Time step Δt	(i) 10^{-6} s, (ii) 10^{-7} s
Total time of each simulation*	10s (simulation), 34h (computation)
(i) Fix membrane, (ii) flexible membrane	
MSM (Eqs. (2.19) and (2.20))	
Parameter	**Value**

Angular coefficient k_a	(a) 0.01 J, (b) 1 J, (c) 0.01 J
Hookean coefficient k_b	(a) $3.1 \cdot 10^5$ J m^{-2}, (b) $2.2 \cdot 10^6$ J m^{-2}, (c) $9.8 \cdot 10^6$ J m^{-2}
Equilibrium distance r_0	$2.5 \cdot 10^{-4}$ m
Equilibrium angle Θ_0	$\pi/2$ rad
BOUNDARIES (Eq. (2.28))	
Constant K	$4 \cdot 10^{-4}$ J
Repulsive radius r*	$2.5 \cdot 10^{-4}$ m
CLOT FORMATION (Section 0)	
Number of time step for clot formation N	10^5 s
R_{max}	(1) $2.28 \cdot 10^{-4}$ m, (2) $2.3 \cdot 10^{-4}$ m, (3) $2.5 \cdot 10^{-4}$ m
Agglomeration probability	25 %
Max bonds per clot particle	(1) 6, (2) 6, (3) 2
(a) soft, (b) intermediate, (c) hard	(1) calcification, (2) free clot, (3) filiform
*dual-processor 8-core (16 cores/node, 2 nodes used) 64-bit 2.2 GHz Intel Sandy Bridge E5-2660	

3.4.1 Hydrodynamics

We compare results obtained with our model with traditional CFD simulations performed with ABAQUS 6.14® with the same geometry and under similar flow conditions. In these simulations, the membrane is fixed in order to focus solely on the hydrodynamics. This is done on purpose: if at this stage we had considered both the fluid and the membrane together, we could not have distinguished whether potential errors originated from the fluid dynamics or the membrane mechanics.

Calculations are run at two constant inlet velocities, 0.2 m s^{-1} and 0.9 m s^{-1}. Because of the different nature of the two modelling techniques, the inlet/outlet boundary conditions (b.c.) are not the same. The DMP uses periodic inlet/outlet b.c., while in the CFD simulation the inlet has constant velocity and the outlet fixed pressure. Fig. 3.3 shows the CFD results; Fig. 3.4 shows the DMP results.

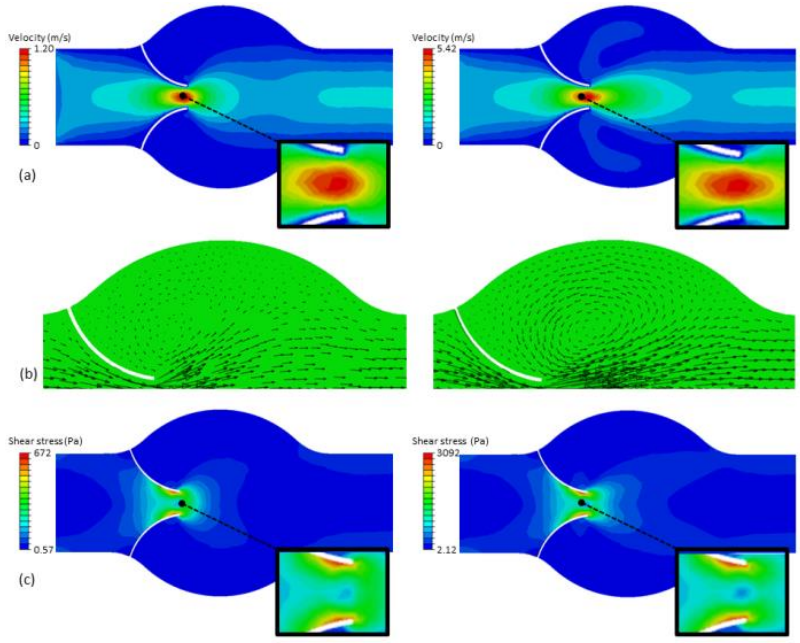

Fig. 3.3. Velocity magnitude (a), velocity vectors (b) and shear stress (c) at 0.2 m s^{-1} (left) and 0.9 m s^{-1} (right) calculated with CFD.

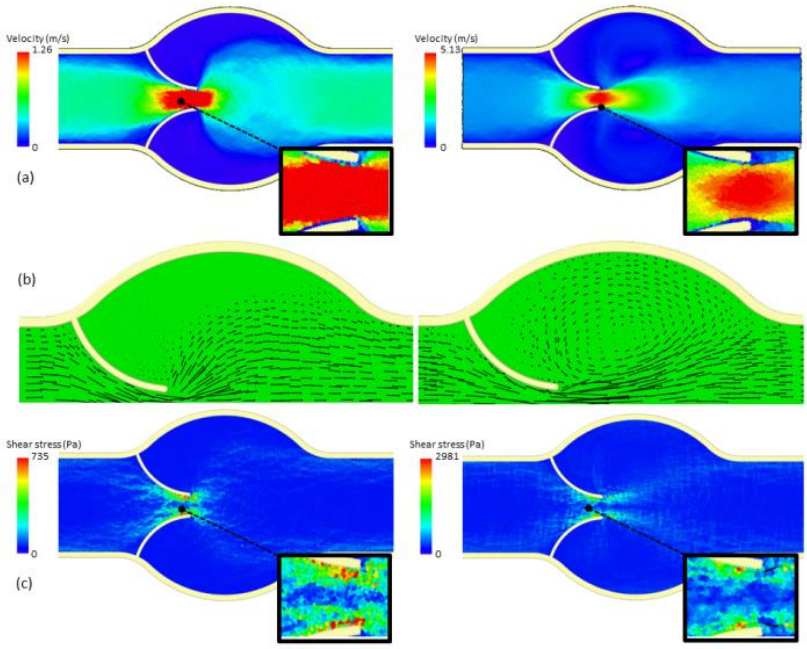

Fig. 3.4. Velocity magnitude (a), velocity vectors (b) and shear stress (c) at 0.2 m s^{-1} (left) and 0.9 m s^{-1} (right) calculated with the DMP.

Comparison between Fig. 3.3 and Fig. 3.4 shows a good agreement between the CFD and the DMP calculations. Both models, in particular, capture the recirculation zones in the circular chamber in the centre. For the velocity, minor differences (2-5%) can be found at the tip of the valve. These differences depend on the different inlet conditions between the DMP and the CFD model and the nature of the discretization method (particles vs. mesh).

Another important variable often reported in the literature is shear stress (Fig. 3.3c and Fig. 3.4c). But also, in this case, CFD and DMP results are similar. Both models, in particular, identify a region of high stress near, but not exactly at, the end of the leaflets.

3.4.2 Membrane deformation

In this section, we account for the flexibility of the leaflets and calculate both the flow and the membrane dynamics. For validation purposes, we compare the membrane deformation observed during the simulations with those obtained experimentally by (Ledesma-Alonso et al. 2014). In both simulations and experiments, the valve has two leaflets and the flow is pulsatile. The geometric conditions, however, are not exactly the same: in (Ledesma-Alonso et al. 2014), in fact, L = 0.0263 m, Z = 0.015 m, and the channel is straight without the circular chamber in the centre (this is why, in Section 3.3.5, we did not introduce a forth dimensionless number). Additionally, our simulations are 2D and based on blood, while (Ledesma-Alonso et al. 2014) employ water in a rectangular channel with depth w = 0.05 m. Table 3.2 gathers all the parameters used in the simulations and in the experiments. The values of k_a and k_b corresponding to a specific F in the simulations are given in Table 3.1. The values of d for the simulations are calculated according to the procedure described in section 3.3.4.

Table 3.2. Geometric parameters, fluid conditions, and membrane constants used in the simulations and in the experiments.

	Simulations	Experiments	Membranes
Z	0.0125 m	0.015 m	All
L	0.016 m	0.026 m	
ρ	1056 kg m^{-3}	1000 kg m^{-3}	
μ	0.0035 Pa s	0.001 Pa s	
Λ	0.78	0.58	
U	0.9 m s^{-2}	0.42 m s^{-2}	Soft
d	0.0003 m	0.0004 m	
f	1 s^{-1}	0.5 s^{-1}	
F	0.008 kg m^{-3} s^{-2}	$2.30 \cdot 10^{-7}$ kg m^{-3} s^{-2}	
Re	3259	6300	
N_f	$6 \cdot 10^{-10}$	$3.11 \cdot 10^{-10}$	
N_R	$1.96 \cdot 10^{-6}$	$1.96 \cdot 10^{-6}$	
U	0.9 m s^{-2}	0.51 m s^{-2}	Intermediate
d	0.00016 m	0.0004 m	
f	1 s^{-1}	0.167 s^{-1}	
F	0.056 kg m^{-3} s^{-2}	2.30 10^{-7} kg m^{-3} s^{-2}	
Re	3259	7650	
N_f	$8.12 \cdot 10^{-11}$	$3.47 \cdot 10^{-10}$	
N_R	$2.65 \cdot 10^{-7}$	$2.66 \cdot 10^{-7}$	
U	0.9 m s^{-2}	0.2 m s^{-2}	Hard
d	0.0003 m	0.0004 m	
f	1 s^{-1}	0.333 s^{-1}	
F	0.12 kg m^{-3} s^{-2}	4.61 10^{-6} kg m^{-3} s^{-2}	
Re	3259	3000	
N_f	$6.36 \cdot 10^{-12}$	$6.9 \cdot 10^{-12}$	
N_R	$2.07 \cdot 10^{-8}$	$2.07 \cdot 10^{-8}$	

After running a large number of simulations and observing how the membrane deforms under various flow conditions, we realised that the fundamental group that affects the membrane dynamics is N_R (Eq.(3.9)). Therefore, we chose specific values of f, g_0 (which gives U), k_a and k_b (which give F and d) to obtain in our simulations the same N_R of the experiments.

We consider three cases that we call, soft membrane, intermediate membrane, and hard membrane. We start with the case of the intermediate membrane (Fig. 3.5a): the 'normal' case, which subsequently is compared to the soft (Fig. 3.5b) and the hard membrane (Fig. 3.6).

Fig. 3.5a shows the comparison between simulations and experiments in the case of the intermediate membrane. The overall dynamics is very similar, but there are some noticeable differences. In the simulation, the maximum opening of the membrane is wider. This is due to the absence of the central chamber in the experimental set-up. Another minor difference occurs at the end of the cycle when the backpressure closes the valve completely. When closed, the experimental valve has a more elongated shape since the leaflets are longer. This is a consequence of the fact that, besides the main group N_R, also Λ (Eq. (3.8)) has a (minor) effect on the membrane. Experiments and simulation have the same N_R, but not exactly the same Λ (see Table 3.2); some (minor) differences, therefore, are expected.

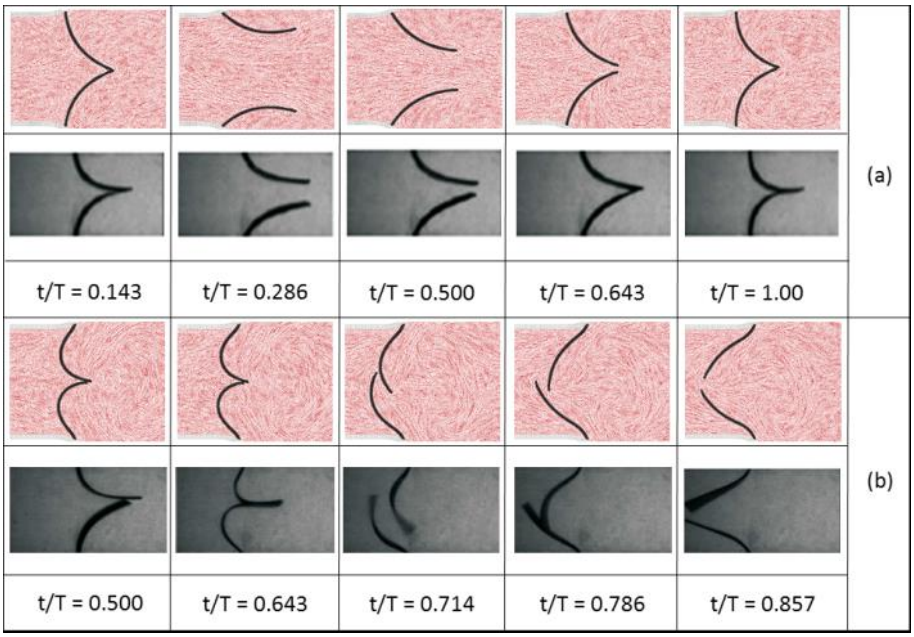

Fig. 3.5. Comparison between simulations and experiments from (Ledesma-Alonso et al. 2014): (a) intermediate membrane, (b) soft membrane.

Fig. 3.5b shows the comparison between simulations and experiments in the case of the soft membrane. The soft membrane can be considered defective since its position is completely reversed by the backflow. As in the previous case, there are some minor differences, but the

overall of the membrane behaviour is well captured by the model. Similar deformation profiles have also been reported by other studies (Bavo et al. 2016).

Fig. 3.6 shows the comparison between simulations and experiments in the case of the hard membrane. Also, the hard membrane can be considered defective since it does not completely open. In this case, the comparison focuses on the membrane's tip. At this location, the two leaflets slide one over the other and symmetry is lost. This phenomenon is captured in both the simulations and the experiments.

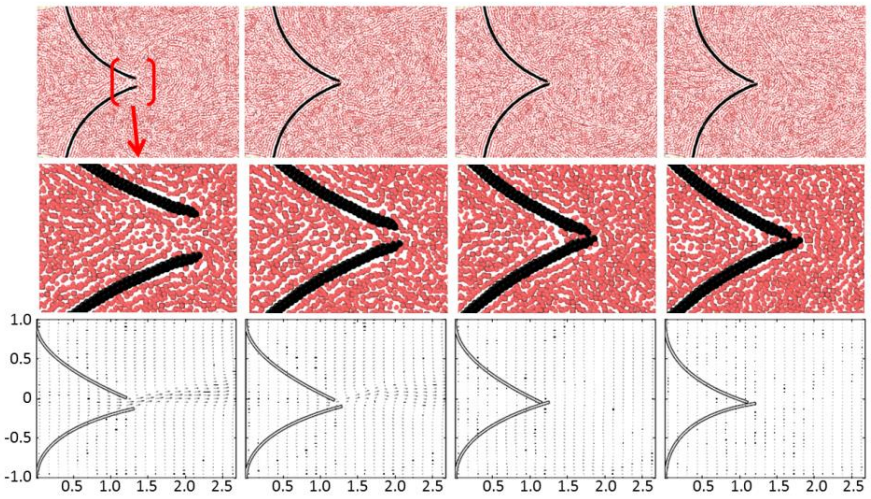

Fig. 3.6. Hard membrane: comparison between simulations and experiments from (Ledesma-Alonso et al. 2014).

The loss of symmetry suggests that the simulations should account for the whole geometry and not only half of it (considering only one leaflet) (De Hart et al. 2000, van Loon et al. 2004, van Loon et al. 2006).

Besides validating our model, this section also highlights the importance of N_R. The values of Re, Λ and N_f between the simulations and in the experiments are different, but, since N_R is the

same, the membrane behaviour in both cases is similar (with the little caveat about Λ as discussed above).

The simulations with different flexibilities show the key role played by the leaflets' elasticity during the diastole. Leaflets with high elasticity are good for the blood circulation with a total opening and closing of the valve during a systole-diastole, but increase the probability of unsynchronised valve motion and consequently risks of reversed flow. Conversely, leaflets with high rigidity ensure a smoothed opening and closing of the valve but, in certain circumstances, do not close completely and, therefore, they may be inefficient in preventing blood reflux.

3.4.3 Formation of solid aggregates

This section develops the solid aggregation scheme presented in Chapter 2. We consider two cases: solid deposits at the membrane surface, and formation of aggregates in the main flow. We generally indicate the first case as 'calcification' and the second as 'clotting'. Our focus, however, is not on the formation and the evolution of actual calcifications and clots. These are very complicated biochemical phenomena (Panteleev et al. 2015) and their full dynamics is beyond the scope of this chapter. The goal is here to illustrate how, given a criterion for aggregation, this can be implemented in our model. Once this has been achieved, more complicated agglomeration models (Harrison et al. 2008, Bajd and Sersa 2013) can be implemented.

Both calcification and clotting imply the formation of solid aggregates developing from the liquid. In the DMP framework, this can be achieved by changing the forces acting on certain particles from SPH to MSM. Fig. 3.7 describes the mechanism used in the simulations.

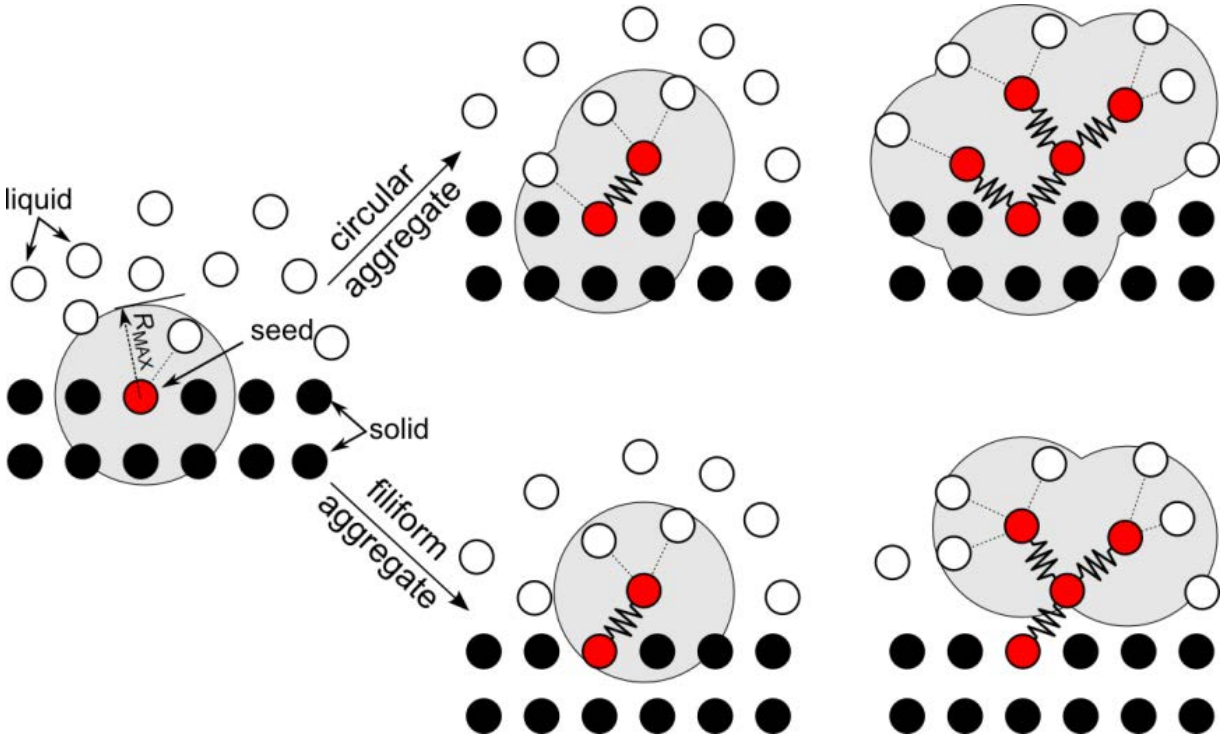

Fig. 3.7. Algorithm for circular and filiform aggregates.

The procedure starts from an agglomeration seed. In our simulations, the seed is chosen arbitrarily, but it can depend on a specific criterion; for example, when local shear stress exceeds a threshold value, the particle at that location becomes a seed. Once the position of the seed is known, the algorithm propagates the agglomerate. Every N time-steps, it identifies all the particles within a distance R_{MAX} from the seed, and, with a certain probability, transforms some of the liquid-particles in solid agglomerate-particles by (i) changing the forces acting on the particles from SPH to MSM, (ii) and creating a bond between the seed and the newly created agglomerate-particle. The strength of the new bond determines the material properties of the agglomerate (see Table 3.1). In our simulations, the probability of transforming a liquid-particle in an agglomerate-particle has been related to a fixed value (see Table 3.1), but, as mention before, it can be associated to a specific criterion (e.g. shear stress threshold).

The algorithm repeats the above procedure iteratively to propagate the agglomerate further and new agglomerate particles create bonds only to other fluid particles and not to existing agglomerate particles. At the next time step, the previously generated agglomerate-particles become seeds; these seeds create new agglomerate-particles and so on as illustrated in Fig. 3.7

We can affect the final shape of the agglomerate by changing, as time progresses, the behaviour of the seeds. If the seeds are active all the time, they continue to create new agglomerate-particles around them until they are fully surrounded by the agglomerate. In this case, the overall shape of the agglomerate tends to be circular. If the seeds remain active only for one time step, the agglomerate propagates in one preferential direction and tends to assume a filiform (thread-like) shape (Fig. 3.7).

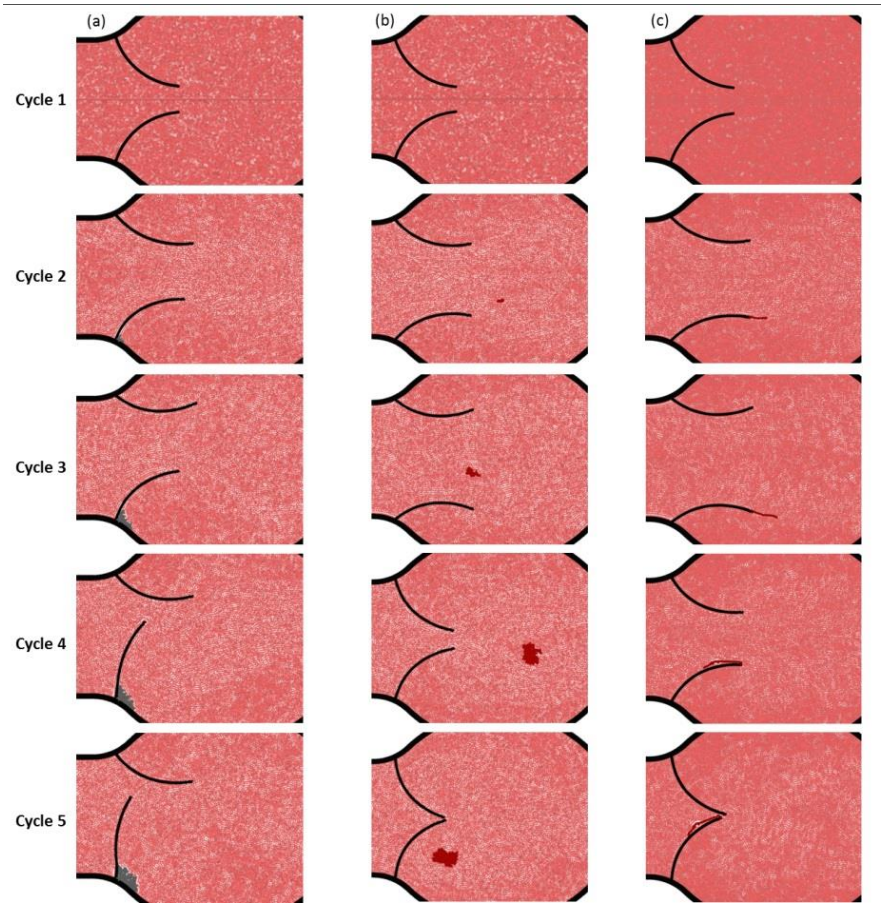

Fig. 3.8. Solid aggregates: (a) ‘calcification’, (b) ‘free clot’ (c) and ‘filiform clot’.

Fig. 3.8 shows three types of simulations where the algorithm is applied to three different configurations. The simulation parameters (N, R_{MAX}, agglomeration probability, etc.) for all three cases are gathered in Table 3.1. With the goal of obtaining a sizable aggregate in a few cycles, we accelerated the agglomerate formation by using higher aggregation probabilities. This is a typical technique used to study phenomena with very different timescales as those occurring in pipelines erosion.

In the first case (called 'calcification' in Fig. 3.8a), the initial seed is located in the region between the membrane and the wall and the deposit propagates following the circular agglomeration algorithm illustrated in Fig. 3.7. An interesting feature of the simulation is that, as time progresses, the agglomerate makes increasingly difficult the movement of the lower leaflet until it stops almost completely.

In the second case (called 'free clot' in Fig. 3.8b), the initial seed is located in the flow and the agglomerate propagates following the circular algorithm. The presence of a solid aggregate alters the hydrodynamics as indicated in Fig. 3.9. Once a liquid particle transforms into a solid particle, the fluid streamlines must change direction to account for the new solid-liquid boundaries. This feature would not be possible with mesh-based algorithms and highlights one of the advantages of DMP.

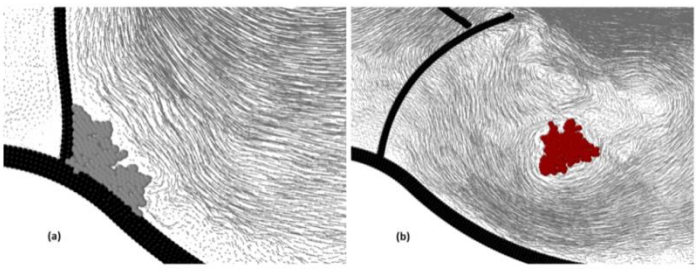

Fig. 3.9. Velocity vectors illustrating how the presence of the aggregate affects the hydrodynamics: (a) 'calcification', (b) 'free clot'.

We can emphasise another advantage of using a particle-based technique by introducing fragmentation. The drag between the fluid and the agglomerate creates internal stresses in the solid. These stresses tend to pull apart the agglomerate-particles that respond with a stronger binding force (according to Eq.(2.19)). At this point, we can slightly modify the algorithm and introduce a criterion for the break-up: if the force between two agglomerate-particles exceeds a certain value, the bond breaks. In Fig. 3.10, we used a threshold force of $1.3 \cdot 10^{-7}$ N. At a certain point of the simulation, the threshold force is exceeded and the agglomerate breaks into two parts. One part remains attached to the leaflet; the other becomes free and moves unrestricted with the flow.

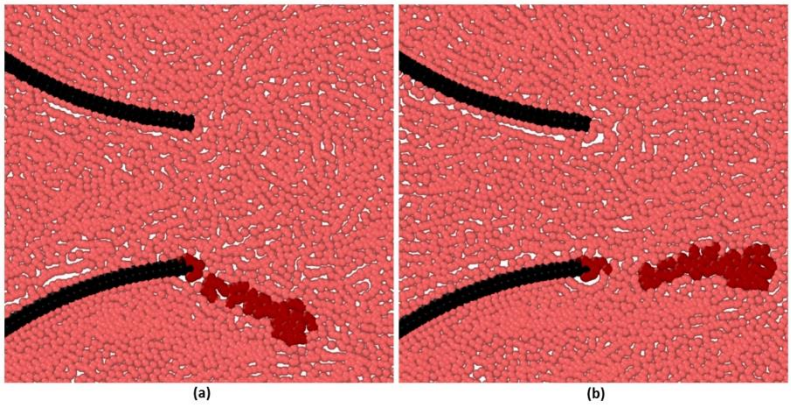

Fig. 3.10. Fragmentation of the agglomerate.

3.5 Conclusions

Mesh-free methods are usually considered viable alternatives to traditional modelling but have never enjoyed the same popularity of mesh-based techniques. Many mesh-free methods have been developed only in relatively recent years and offer, to the potential user, less available information, experience and software. On the other hand, a specific sub-set of the mesh-free algorithm (e.g. SPH, DEM, MSM, BD etc.) share a common particle-based

framework that makes particularly easy their linkage in multi-physics problems. In this chapter, we show that, in certain circumstances, it is more than a mere alternative to traditional modelling. Discrete Multi-Physics can tackle, with relatively little effort, problems that are considered very challenging with mesh-based multi-physics. Elsewhere (Alexiadis 2014, Alexiadis 2015a, Alexiadis 2015b), we focused on solid-liquid flows where the dispersed phase is made of deformable, breakable, dissolving, melting or solidifying particles. Here, we apply the same approach to biological valves including the formation of solid aggregates in the flow and at the membrane surface. To the best of our knowledge, this is the first study to directly account for the hydrodynamics, the membrane deformation and the formation of solid aggregates at the same time and, as such, it has the potential to open a new perspective to the modelling of biological valves.

3.6 Notation and abbreviations

Notation

m	Mass, kg
Z	Half thickness, m
L	Length of the membrane, m
R	Circular area, m
E	Young modulus, kg m^{-1} s^{2}
F	Flexural rigidity, kg m^{3} s^{-2}
k_b	Bond Hookean coefficient, J m^{-2}
r_0	Equilibrium distance, m
k_a	Angular Hookean coefficient, J
θ_0	Equilibrium angle, rad
P	Pressure, Pa
A	Amplitude, (-)
t	Time, s
T	Period, s
g	Acceleration, m s^{-2}

f	Oscillation frequency, s^{-1}
Re	Reynolds number, (-)
Nf	Dimensionless frequency, (-)
N_R	Dimensionless factor, (-)
Λ	Geometric ratio, (-)
ρ	Density, kg m^{-3}
U	Reference velocity, m s^{-1}
μ	Fluid viscosity, Pa s
d	Membrane thickness, m
T	Torsional rigidity, N m
I_i	Moment of inertia, m m^3
M	Cross section, m^2
h	Smoothing length, m
c_0	Artificial sound speed, m s^{-1}
Δt	Time step, t
w	Width, m
Δr	Initial distance, m

r^*	Repulsive radius, m
P	Agglomeration probability, (-)
R_{max}	Distance, m
N	Number of time step, (-)

Abbreviations

CFD	Computational Fluid Dynamics
FSI	Fluid Structure Interaction
IBM	Immersed Boundary Method
DMHS	Discrete Multi-Hybrid System
SPH	Smoothed Particle Hydrodynamics
DEM	Discrete Element Method
BD	Brownian Dynamics
LAMMPS	Large-scale Atomic/Molecular Massively Parallel Simulator
MSM	Mass and Spring Model
DMP	Discrete Multi-Physics

CHAPTER 4: STRESS AND STAGNATION IN DEEP VEINS VALVES

4.1 Abstract

The hemodynamics in flexible deep veins valves is modelled by means of Discrete Multi-Physics and an agglomeration algorithm is implemented to account for blood accrual in the flow. Computer simulations of a number of valves typologies are carried out. The results show that the rigidity and the length of the valve leaflets play a crucial role in both mechanical stress and stagnation in the flow. Rigid and short membranes may be inefficient in preventing blood reflux, but reduce the volume of stagnant blood potentially lowering the chances of thrombosis. Additionally, we also show that in venous valves, cell agglomeration is driven by stagnation rather than mechanical stress.

4.2 Introduction

Thrombosis is a medical condition which relates to the formation of blood clot and resulting to Deep venous thrombosis (DVT) in deep veins. Such thrombi contain blood cells (including red blood cells and platelets) within a mesh of coagulated protein which is predominantly fibrin. If one of these aggregates detaches from the vein, it can reach the lungs leading to a potentially life-threatening complication known as pulmonary embolism (PE). In the UK, the number of deaths (around 25,000 deaths annually) caused by DVT and PE (designated together as venous thromboembolism, VTE) is more than the total of deaths from breast cancer, AIDS, breast cancer and road traffic accidents combined (Hunt 2009).

One of the factors exacerbating DVT is prolonged immobility (e.g. bed ridden after surgery, limb paralysis and long-haul flights), where the insufficient efficacy of the muscle pump, which normally assists blood flow through the leg veins, leads to sluggish flow. Stasis and low flow states are classically associated with a high probability of thrombus formation (Reitsma et al. 2012). Because of this, it is likely that flow motion in veins, in particular, in the vicinity of the valve, can play a fundamental role in the formation of thrombi (Bovill and van der Vliet 2011). Since hydrodynamics is affected by the valve characteristics, the valve characteristics can also affect thrombus agglomeration but the actual mechanisms remain unclear.

Moreover, once a person has developed DVT and has been successfully treated, he or she is likely to develop other thrombi in the future, suggesting that the person's specific valve geometry or flexibility may also contribute to the solid blood formation.

By providing hydrodynamic information of the blood flow around the valve, computer simulations can improve our understanding of the link between fluid dynamics and DVT. Computational blood dynamics has been widely and successfully used for cardiac valves (e.g. (De Hart et al. 2000, Fenlon and David 2001, van Loon et al. 2004, Buxton and Clarke 2006, Watton et al. 2007, van Loon 2010, Astorino et al. 2012, Espino et al. 2012, Bahraseman et al. 2014, Al-Azawy et al. 2015, Borazjani 2015, Halevi et al. 2015, Kamensky et al. 2015, Marom 2015, Miandehi et al. 2015, Bavo et al. 2016), but with a few exceptions so far little attention has been given to venous valves (e.g. (Wijeratne and Hoo 2008, Keijsers et al. 2015)). In the majority of the venous valve simulations, the valve is fixed and the complex interaction between the flow and the moving leaflets is lost. Recently, flexible structures were investigated with the Fluid Structure Interaction (FSI) method (Simão et al. 2016). Nevertheless, analyses remain often limited to few cycles or implemented with one symmetrical leaflet. One of the reasons is related to the intrinsic difficulty of the FSI to simulate the leaflets' contact at the end of the closing phase. A few studies (e.g. (van Loon 2010, Kamensky et al. 2015)) used additional contact algorithms to account for the mechanical contact of leaflets. However, the implementation of these algorithms is complex and the frequency of the re-meshing close to the contact point remains an issue.

In this work, we use the Discrete Multi-Physics (DMP) approach developed in Alexiadis (2015) to model both the fluid dynamics and the flexible leaflets. This approach was previously used for cardiac valves (Chapter 3). In this previous work, based on both dimensionless analysis and direct numerical simulations, we have shown that size and rigidity of the leaflets, together with inlet velocity, are key parameters and have determined which factors most affect the hydrodynamics around the valve. For comparison, we focus on these

parameters in this study, to specific flow patterns and stress profiles in a venous valve system using the DMP approach.

Other advantages of the approach proposed here are that, contrary to FSI simulation, it can account for a complete valve closure without the use of a stabilisation algorithm.

Finally, using DMP gives the possibility of introducing an agglomeration algorithm that transforms a portion of the liquid into a solid. Other studies (e.g. (Simão et al. 2016)) simulated cell aggregates by tweaking the viscosity of the liquid, but with the method proposed here, we can form actual solid structures within the liquid phase. By introducing the agglomeration algorithm, we identify among the regions where thrombi are most likely to form and which have the highest growth probability.

4.3 Methodology

4.3.1 Modelling

The DMP modelling technique used in this work is based on the so-called Discrete Multi-Hybrid System (DMHS). In the DMHS model, the liquid is represented by Smoothed Particle Hydrodynamics (SPH) particles (Monaghan 1994, Morris et al. 1997, Liu and Liu 2003) , while the solid structure is divided into many notional particles linked by computational springs (to model the elastic modulus of the solid), computational hinges (to model the flexural modulus) and computational dashpots (to model the viscous material behaviour). Mathematically, this is similar to the treatment of molecular bonds used in Molecular Dynamic (MD) simulations.

4.3.2 Geometry

In this study, we use a two-dimensional schematic representation of the leg venous valve (Wijeratne and Hoo 2008) as illustrated in Fig. 4.1. The channel radius is Z = 0.004 m, the radius of the valve chamber is R = 0.007 m and its length is Y = 0.04 m. Three different lengths L of the membrane are studied: long (0.0256 m), medium (0.0175 m) and short (0.01 m). In order to distinguish different parts of the geometry, we refer to the region between the two leaflets as the ‘opening region’ and to the two regions between the wall and the leaflet as ‘sinus regions’. Fig. 4.1 shows the location of the opening region and one of the two sinus regions (the other is symmetric and located above the upper leaflet).

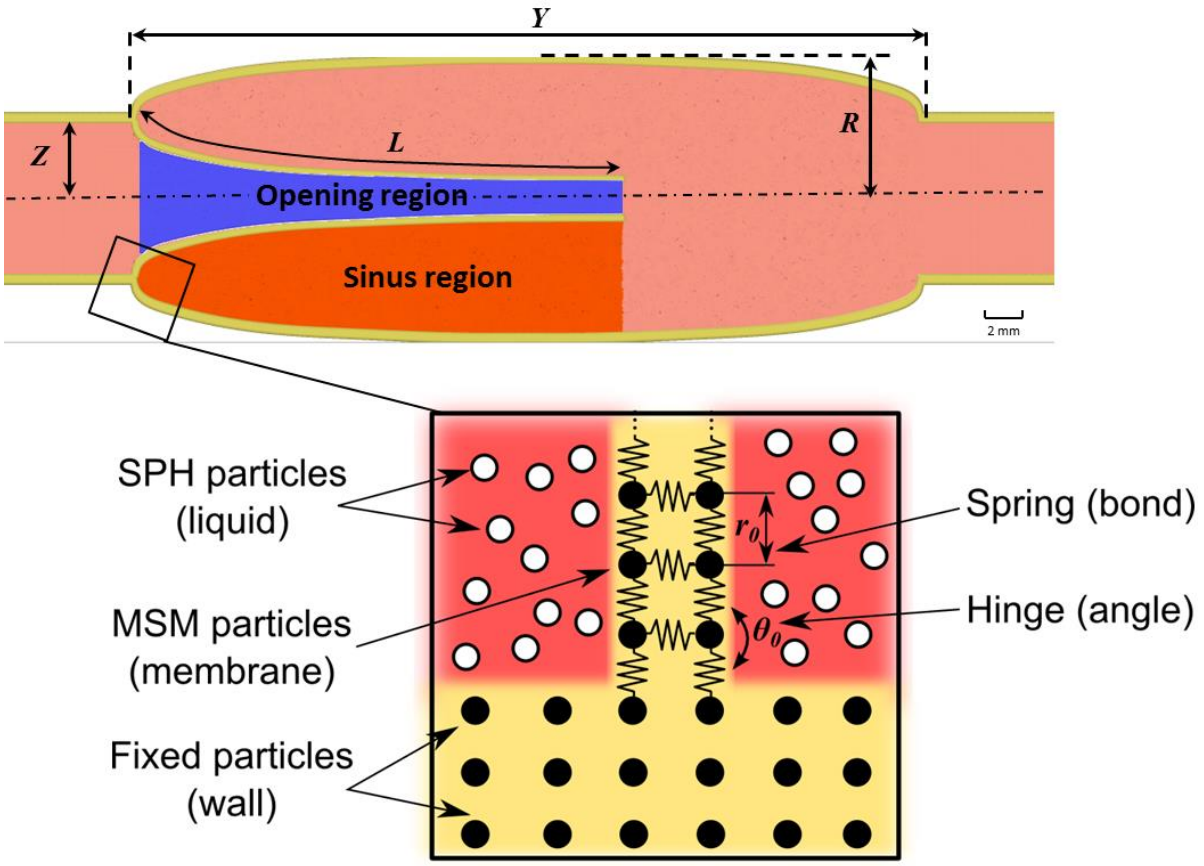

Fig. 4.1. Illustration of the venous valve 2D geometry and particle representation.

The leaflets are represented by (solid) MSM particles joined together by springs and hinges (Fig. 4.1) as discussed in section 2.4, SPH particles are used for the fluid and stationary (solid) particles for the walls. Three layers of particles are used for the channel and two for each leaflet.

There are two types of parameters required for the simulations: model parameters and simulation parameters. The first group consists of internal parameters used by the SPH and MSM solvers (Table 4.2); the second refers to the operative conditions detailed below.

4.3.3 Simulation conditions

The Young's modulus E and the flexural modulus F of the membrane are the results of the MSM particles joined together by numerical springs and hinges. The relation between the spring (k_b) and hinge (k_a) constants and the actual Young's modulus and the flexural modulus is given in section 3.3.4. A viscous coefficient (k_v) is added to the MSM springs to confer viscoelastic properties to the membrane as in a Kelvin–Voigt material.

Periodic boundary conditions are used at the inlet/outlet and we implement the same pulsatile flow (purely oscillatory) used by (Wijeratne and Hoo 2008) and imposing to each liquid particle the acceleration g as shown in Eq. (4.1)

$$g = g_0 \sin(2\pi f t), \tag{4.1}$$

with amplitude g_0 , time t and oscillation frequency $f = 1/T$ (with T the period oscillation). We use Eq. (4.1) as a simple means of forcing alternating flow in the valve, but the real oscillation is not sinusoidal and the frequency is not constant. We chose $T = 4$ s, which is long enough to ensure full closure. Here we limit the total time of calculation with 4 full cycles (opening and closing) which correspond to 16 s. Previous work (Wijeratne and Hoo 2008) used $T = 3$ s and simulated only one full cycle. When the muscles contract, the blood within the veins is compressed and the valve opens; when the muscles dilate, the valve closes preventing backward flow. The blood velocity depends on the force of the muscle contraction and, in general, it is related to the level of physical activity of a specific person. In order to account for three levels of physical activity, we take into account three values of g_0 (0.1 m s^{-2}, 0.25 m s^{-2} and 0.4 m s^{-2}), which result in three different flows with maximum velocities in the inlet channel of 0.03 m s^{-1} (low physical activity), 0.07 m s^{-1} (intermediate case), 0.13 m s^{-1} (high

level of physical activity) respectively. The low velocity is from (Simão et al. 2016), the intermediate velocity is from (Wijeratne and Hoo 2008) and we include the third highest velocity to account for high levels of physical activity. In all cases, the flow is laminar.

The length and the flexibility of the membrane vary from person to person (Mühlberger et al. 2008, Moore et al. 2011). In order to investigate a variety of individual variations, we consider three membrane lengths (0.0256 m, 0.0175 m, and 0.01 m). The longest length is from (Wijeratne and Hoo 2008) and the shortest length is chosen as the minimum size allowing a complete closure of the leaflets. Regarding the flexibility and the stiffness, in Chapter 3, the literature review for the aortic valve has shown that the membrane has three dynamic regimes based on the membrane stiffness (De Hart et al. 2000, van Loon et al. 2006, Ledesma-Alonso et al. 2014, Bavo et al. 2016). In the simulation, we vary the stiffness of the valve according to these regimes (see Table 4.1).

Table 4.1. List of simulations with fluid velocities and membrane parameters.

Variation of the membrane length and the velocity with k_a = 0.01 J		
Length of the membrane L [m]	V [m s^{-1}]	Designation
Short L= 0.01 m	0.03	L0.01/V0.03/k_a0.01
	0.07	L0.01/V0.07/k_a0.01
	0.13	L0.01/V0.13/k_a0.01
Medium L= 0.0175 m	0.03	L0.0175/V0.03/k_a0.01
	0.07	L0.0175/V0.07/k_a0.01
	0.13	L0.0175/V0.13/k_a0.01
Long L= 0.0256 m	0.03	L0.0256/V0.03/k_a0.01
	0.07	L0.0256/V0.07/k_a0.01
	0.13	L0.0256/V0.13/k_a0.01

Variation of the membrane flexibility with L = 0.0256 m and V = 0.07 m s^{-1}	
Angular coefficient k_a [J]	Designation
0.0001	L0.0256/V0.07/k_a0.0001
0.002	L0.0256/V0.07/k_a0.002
0.005	L0.0256/V0.07/k_a0.005
0.02	L0.0256/V0.07/k_a0.02
0.05	L0.0256/V0.07/k_a0.05

4.3.4 Agglomeration algorithm

In order to understand the agglomeration dynamics, we introduce in the model the agglomeration algorithm developed for Chapter 3. At this stage, our focus is to understand if hydrodynamics alone favours agglomeration at different locations. The actual biochemical process of thrombus formation is an extremely complex phenomenon (e.g.(Panteleev et al. 2015)) and it is beyond the scope of this study.

Specific particle points are used as agglomeration seeds. The algorithm every N time-steps checks all the fluid particles at a distance R_{MAX} from the seeds and, with a certain probability P, transforms some of these particles into solid agglomerate-particles.

In the simulations, the values of N, R_{MAX} and P are given in Table 4.2. These values do not correspond to the real time-scale of agglomeration but were chosen in order to accelerate agglomeration and to observe significant growth in few cycles. Since our goal is to determine where agglomeration is more likely, this 'accrual acceleration' does not affect the validity of the results, as long as the timescale of agglomeration is longer than the timescale of the flow.

Table 4.2 Model parameters used in the simulations.

SPH (Eqs. (2.12), (2.13), (2.14))	
Parameter	**Value**
Number of SPH wall particles (3 layers)	5360
Number of SPH valve particles (2 layers)	(1) 1026, (2) 702, (3) 402
Number of SPH fluid particles	(1) 89592, (2) 89726, (3) 90012
Mass of each particle (fluid)	$1.05 \cdot 10^{-5}$ kg
Mass of each particle (wall and valve)	$2 \cdot 10^{-5}$ kg
Initial distance among particles Δr	$1 \cdot 10^{-4}$ m
Smoothing length h	$2.5 \cdot 10^{-4}$ m
Artificial sound speed c_0	10 m s^{-1}
Density ρ_0	1056 kg m^{-3}
Time step Δt	10^{-7} s
Total time of each simulation*	16s (simulation), 76h (computation)
MSM (Eqs. (2.19) and (2.20))	
Parameter	**Value**
Angular coefficient k_a	See Table 4.1
Hookean coefficient k_b	$1 \cdot 10^{6}$ J m^{-2}
Viscous damping coefficient k_v	0.01 kg s^{-1}
Equilibrium distance r_0	$1 \cdot 10^{-4}$ m
Equilibrium angle Θ_0	$\pi/2$ rad
BOUNDARIES (Eq. (2.28))	
Constant K	$4 \cdot 10^{-4}$ J
Repulsive radius r*	$1 \cdot 10^{-4}$ m
CLOT FORMATION (Section 0)	
Number of time step for solid formation N	$0.5 \cdot 10^{6}$ s
Distance R_{max}	$2.5 \cdot 10^{-4}$ m
Agglomeration probability P	50 %
Max bonds per solid particle	4
(a) long, (b) medium, (c) short membrane	
*dual-processor 8-core (16 cores/node, 4 nodes used) 64-bit 2.2 GHz Intel Sandy Bridge E5-2660	

4.4 Results and discussion

4.4.1 Stress and residence time

According to (Simão et al. 2016), causes of DVT among young people remain unknown in most of half of the cases. When the origin of DVT is known, thrombus initiation is often

associated with blood coagulability, changes in the vessel wall or immobility (Esmon 2009). In the case of immobility, low velocity and high residence time are the most causes of blood aggregation (Bovill and van der Vliet 2011, Menichini et al. 2016). Although, shear stress can also play a role in platelet aggregation and activation. In fact, components of the coagulation cascade and platelets can be activated by all shear stresses, just mechanisms will be different. For instance, at low shear stress, platelets adhere to fibrinogen, whereas at high shear stress to von Willebrand factor (Ikeda et al. 1991). Likewise, abnormal shear stress distribution can initiate and accelerate the formation of thrombi (Hou et al. 2015). In the arterial setting, high stress could be an activator of platelet aggregation (Zhang et al. 2002). However, arterial and venous thrombi are structurally different. In arteries, high shear may induce platelet activation and formation of what is sometimes called white thrombi with few red cells in it. In veins, the thrombus is red with many red cells trapped in coagulated proteins. In this case, coagulation seems to be the dominant process, suggesting a slower, time-dependent, accrual.

The following discussion focuses on both mechanical stress and residence time, to account for the two factors that are most generally related to thrombus formation (Zhang et al. 2002).

4.4.1.1 Mechanical stress

Our DVT calculations show that shear stress (Tshear) is high only in the opening region and almost negligible everywhere else (Fig. 4.2a). Clinical experience, however, indicates that thrombi do not form in the opening region, where shear stress is high, but rather in the sinus region (Bovill and van der Vliet 2011) where it is at its lowest. Ju et al. (2016) suggest that total mechanical stress (Ttot), rather than shear stress should be investigated and our results show that, in this case, stress is high on both sides of the membrane (Fig. 4.2b).

In a fluid, the total mechanical force is the sum of viscous forces (shear stress), pressure forces and body forces (here gravity is ignored). Fig. 4.2c shows the pressure profile (Ptot) and indicates that the higher stress on the membrane cannot be justified by pressure alone. When a solid body moves in the fluid, however, the change of the relative velocity of the body with respect to the fluid generates additional forces such as the so-called added force, which explains the higher stresses on the membrane in the sinus region.

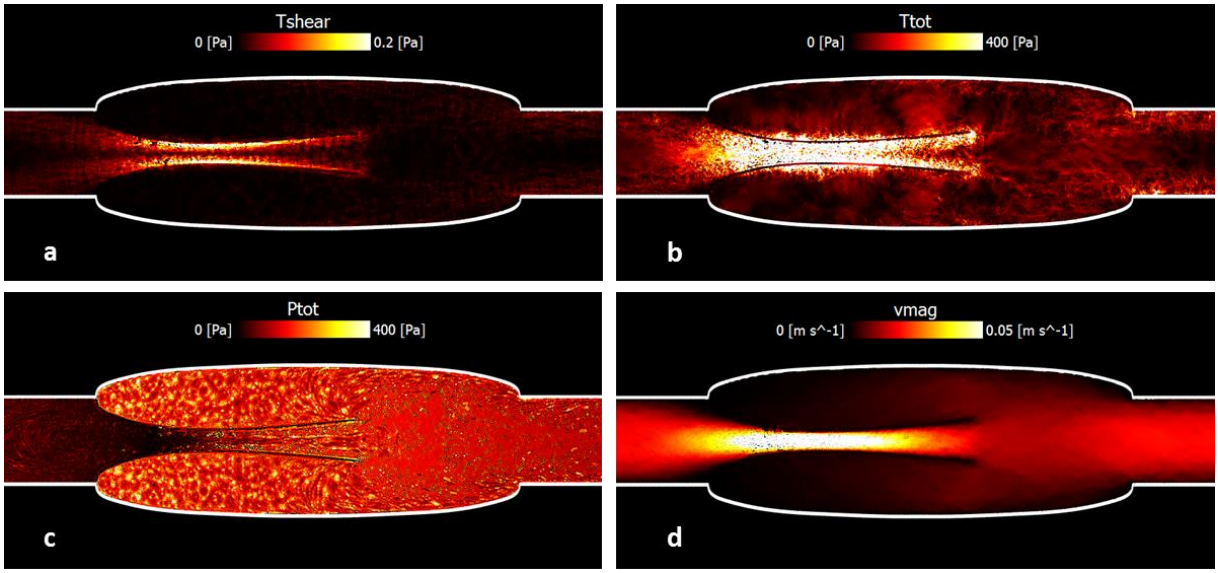

Fig. 4.2. Shear stress (a), total mechanical stress (b), pressure (c), and velocity magnitude (d) for L0.0256/V0.03/ka0.01.

4.4.1.2 Residence time in the sinus

In Lagrangian approach, displacement is used as a proxy for residence time and the following discussion is based on this parameter instead of residence time.

As shown in Fig. 4.2d, the velocity (Vmag) in the sinus region is low compared to that of the opening region; as a consequence, the residence time of fluid particles in this region is higher. Fig. 4.3 illustrates this point. We highlight the particles initially in the sinus in blue and we

track their position during the simulation. At the end of four cycles, a fraction of the particles has left the sinus, while the rest remains confined in this region. In Fig. 4.3, during the closing phase, the particles are coloured according to their *displacement,* defined as the distance travelled by each particle during the simulation. At t = 0 s, the system is at rest and therefore all selected particles are coloured in blue (corresponding to v = 0 m s^{-1}). During the diastole (flow moves in the left direction and closes the valve), blue particles do not move very much and are substantially stagnant; red particles have higher velocity and show higher displacement.

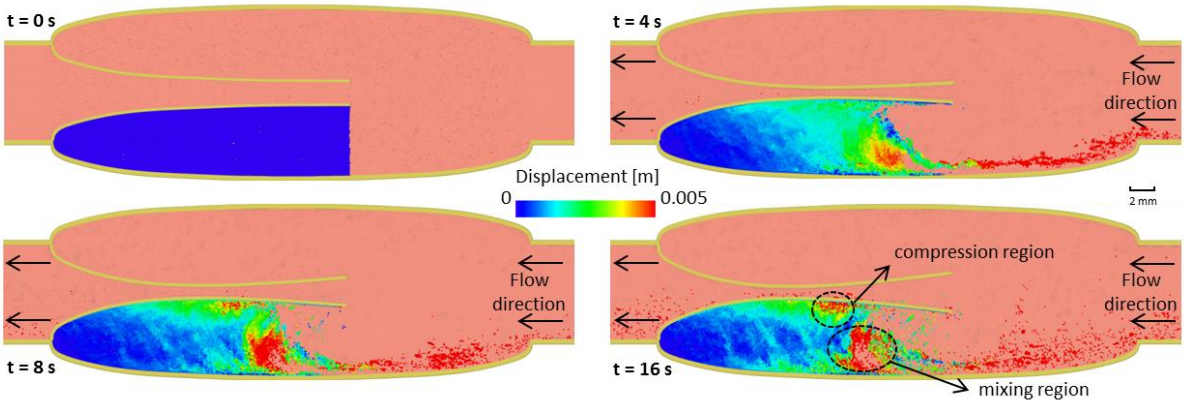

Fig. 4.3. Simulation snapshots illustrating the fluid motion of the particles initially in the sinus at different times (beginning of each new cycle): for L0.0256/V0.03/ka0.01; particles coloured according to their displacement.

In the sinus, we can identify two areas of high fluid displacement. The first (called 'mixing region' in Fig. 4.3) corresponds to the recirculation region created by the backflow (Fig. 4.4). The second (called 'compression region' in Fig. 4.3) is below the membrane and corresponds to the part of the fluid displaced by the oscillating movement of the membrane. There is a fundamental difference between the two regions. While in the mixing region the fluid

particles are actually moved out of the sinus by the backflow, in the compression region the particle only oscillates around the same point due to the alternate motion of the membrane.

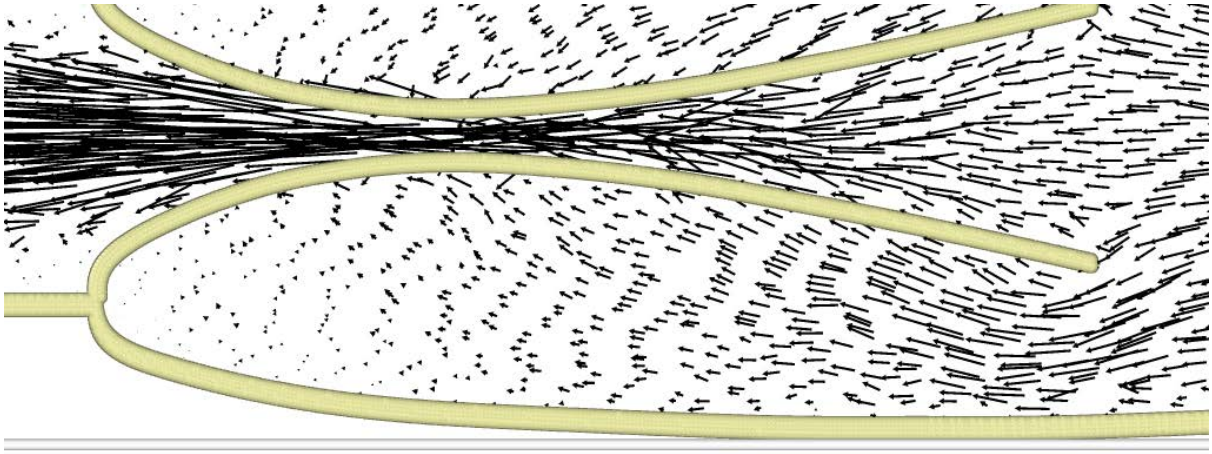

Fig. 4.4. Velocity profile in the sinus area (vectors) for L0.0256/V0.03/ka0.01.

Despite the fact that both regions show high displacement, the actual residence time is high only in the compression region.

Displacement alone, therefore, is not enough to distinguish between regions of low and high residence time. In order to account for this, in the next section, we introduce the time-averaged displacement as a more accurate proxy for the residence time.

4.4.2 Parametric study

In this section, we investigate how Ttot and displacement are affected by (i) membrane flexibility, (ii) leaflet length and (iii) level of physical activity (fluid velocity). According to our simulations, all of these three parameters are particularly significant for the performance of the valve. Comparing the effect of these parameters among different setups, however, is not straightforward because it changes in space and time. To compare results with respect to the same reference point, we identify the fluid particle in the sinus region with the highest

mechanical stress and for every setup, we measure stress and displacement at this location. In this way, we carry out all our measurements at the same relative position. However, as indicated in Fig. 4.5, displacement and Ttot also change with time. To account for this, in the case of displacement (Fig. 4.5a), we use the time-average instead of the instantaneous displacement. In the case of Ttot (Fig. 4.5b), we use the maximal rather than the average stress because agglomeration is more affected by the peak of the stress rather than its average.

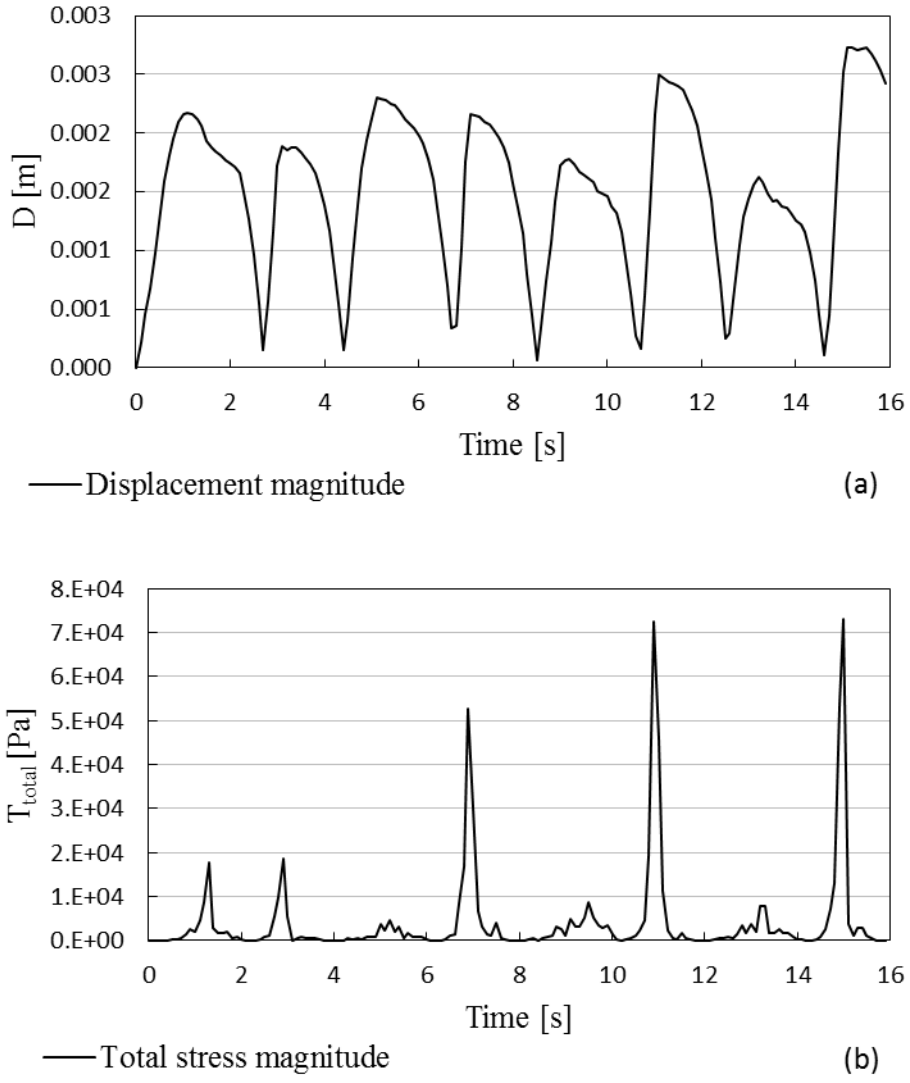

Fig. 4.5. Time evolution of the local fluid displacement (a) and total mechanical stress magnitude (b) for the particle of maximal stress (L0.0256/V0.03/ka0.01).

We can also quantify how both these parameters oscillate with time by calculating their standard deviation; in the subsequent figures, the error bars indicate the standard deviation.

4.4.2.1 Effect of membrane flexibility

The membrane is considered viscoelastic as a Kelvin–Voigt material and its flexibility depends on the flexural modulus. In Chapter 3, we showed that the flexural modulus is mostly affected by the k_a, for this reason, in this section we focus on how time-averaged displacement and maximal stress vary with this parameter.

In Fig. 4.6, both average displacement and Ttot decrease as the membrane flexibility increases to a value k_a = 0.02 J because mechanical deformation is lower for rigid membranes. However, the displacement of very rigid membranes (k_a = 0.05 J) increases. The reason for this can be understood by comparing Fig. 4.7a and b: at k_a = 0.05 J, the leaflets maintain a straight profile during the closure phase (Fig. 4.7a), while at k_a = 0.02 J they bend under the flow (Fig. 4.7b). When the leaflets bend, they partially shield the sinus region from the backflow and reduce the velocity (and therefore the displacement). Conversely, very flexible membranes (k_a < 0.005 J) highly deform and fluctuate under the flow (Fig. 4.7c). This explains the higher standard deviation in Fig. 4.6 and the irregular profile of Fig. 4.6b for k_a < 0.005 J.

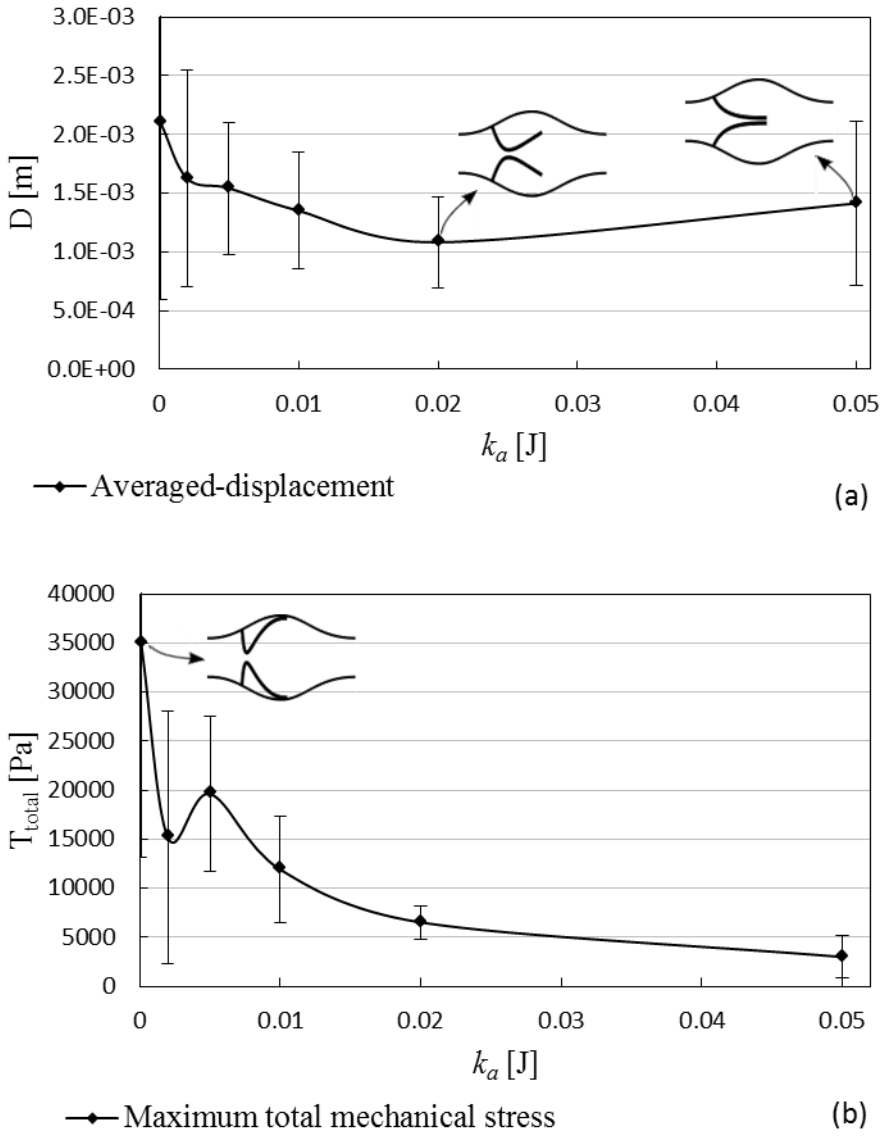

Fig. 4.6. Time-averaged displacement (a) and total mechanical stress (b) versus k_a (valve flexibility) for cases: L = 0.0256 m, V = 0.07 m s^{-1} and k_a from 0.0001J to 0.05J.

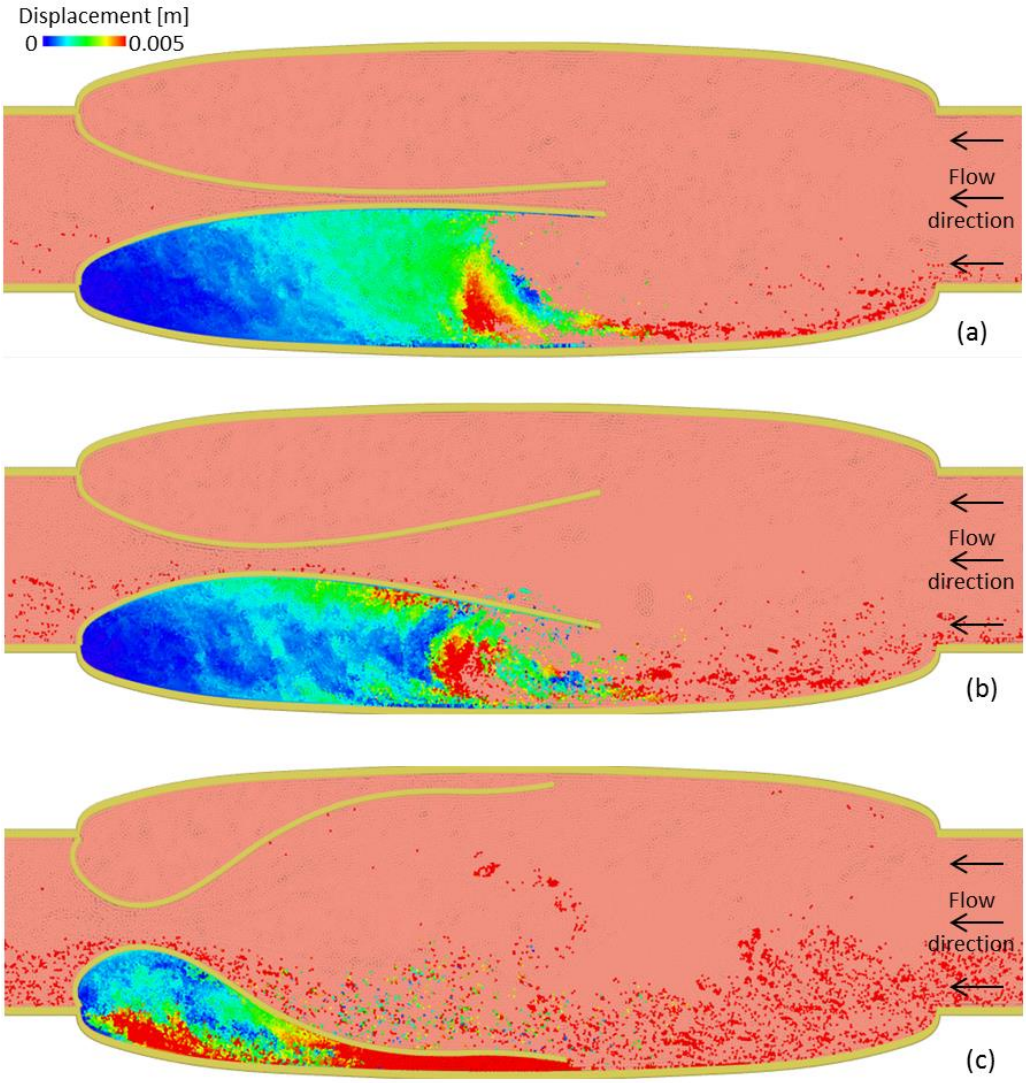

Fig. 4.7. Simulation snapshots illustrating the fluid motion of the particles initially in the sinus for long valve, V= 0.07 m s^{-1} and three flexibilities: (a) k_a = 0.05 J, (b) k_a = 0.02 J, and (c) k_a = 0.0001 J, particles coloured according to their displacement.

4.4.2.2 Effect of membrane length and inlet velocity

Fig. 4.8 shows the effect of the inlet velocity on the displacement and stress for three membrane sizes. For medium or long membranes, as expected, higher velocities are associated with higher stress and displacement. The short membrane, however, behaves differently.

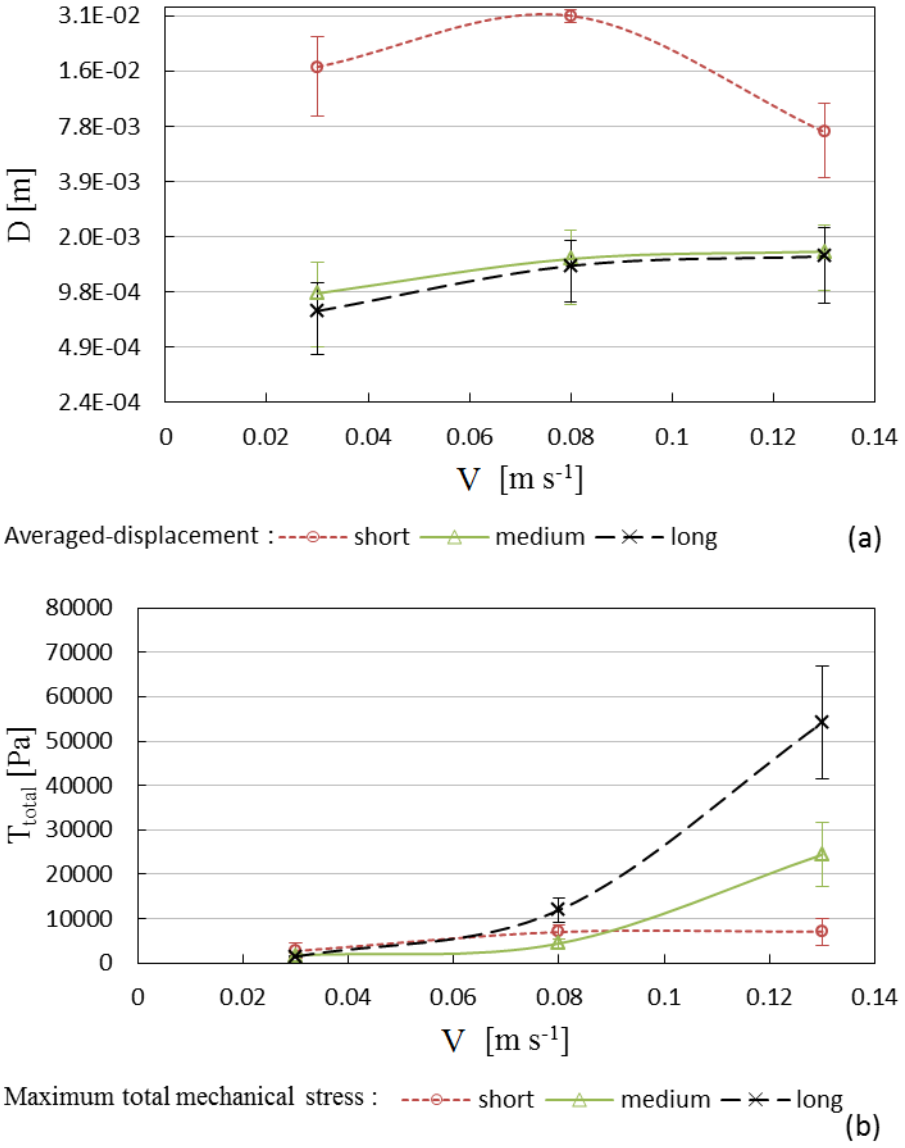

Fig. 4.8. Evolution of displacement (a) and total mechanical stress magnitude (b) with the maximum inlet velocity.

Contrary to the medium and long membrane (see Fig. 4.2), in short membranes, the highest stress (see Fig. 4.9) is located at the tip rather than the middle of the valve. At the tip, the motion of the particles depends on the hydrodynamics at the opening region rather than that at the sinus region and, therefore, they are easily transported away by the flow and the displacement increases significantly.

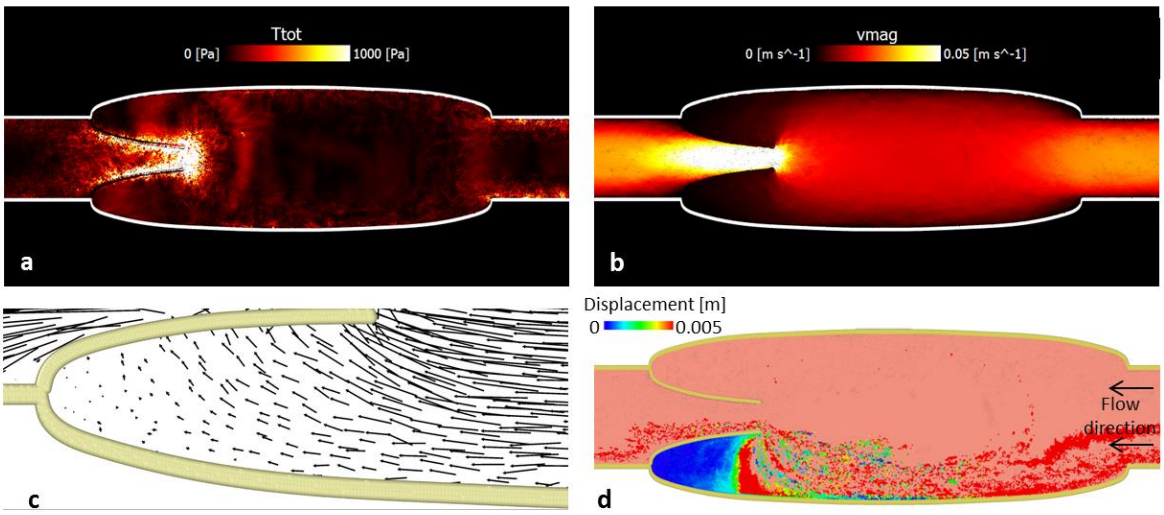

Fig. 4.9. Total mechanical stress (a), velocity magnitude (b), vector velocity (c), and displacement (d) in the short valve case for L0.01/V0.07/ka0.01.

4.4.3 Agglomeration

The main physical parameters that affect agglomeration are the residence time and mechanical stress. The simulations highlight two key locations: one at the sinus side of the membrane, where stress is the highest (point P_1 in Fig. 4.10), and the other at the valve/wall connection where the residence time is the highest (point P_2 in Fig. 4.10).

The higher mechanical stress at P_1 pushes particles closer, increasing the number of particles inside R_{MAX}; however, because the velocity is higher, these particles remain inside R_{MAX} only for a short time. At P_2, the opposite happens: the mechanical stress is lower, but also, because the velocity is low (and, therefore, the residence time is high) and the particles remain inside R_{MAX} for longer.

High stresses and high velocities, therefore, have opposite effects on agglomeration. Fig. 4.10 shows faster growth at P_2, suggesting that residence time may be more important for aggregation propagation in the venous valve than mechanical stress.

However, the algorithm remains qualitative rather than quantitative and only based on inter-particle distance. To provide a medical predictive tool, agglomeration process quantification needs the introduction of other parameters such as chemical phenomena and breakage (linked with stresses).

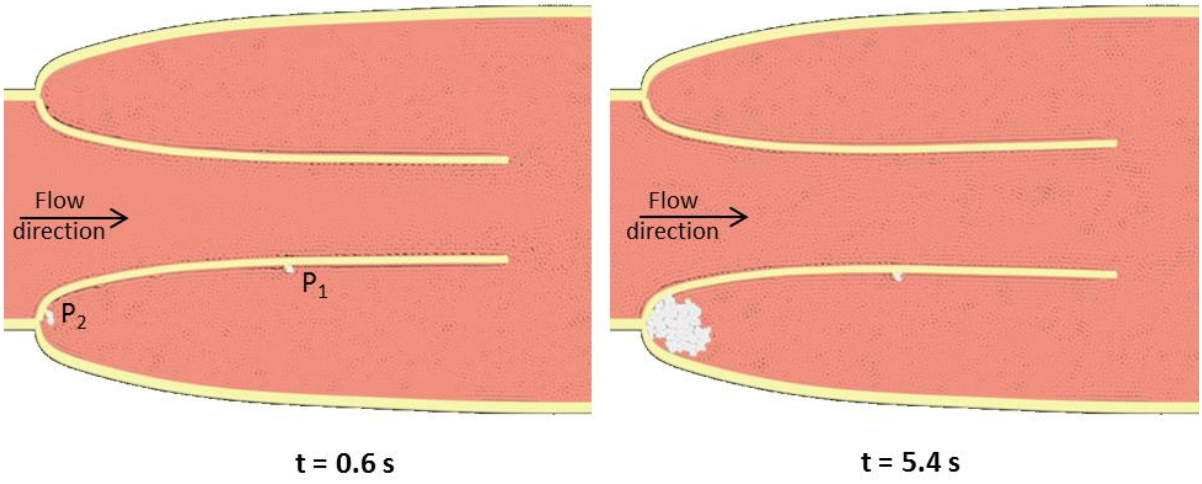

Fig. 4.10. Solid aggregates in the sinus region at two different times for L0.0175/V0.07/k_a0.01.

4.5 Conclusions

This chapter presents a Discrete Multi-Physics model for both blood dynamics and leaflets mechanics of a leg venous valve. In the simulations, we focused on mechanical stress and flow stagnation (high residence time) in the sinus region because these two factors have been linked to the onset of blood solid formation. The model is subsequently coupled with an agglomeration algorithm to account for the formation and propagation of solid aggregates in the flow.

The results show that the flexibility and the length of the membrane play a crucial role in both stress and flow stagnation. Rigid membranes do not close completely and, therefore, they may be inefficient in preventing blood reflux. However, they also allow for a larger flow exchange between the sinus region and the central flow reducing stagnation and, potentially, lowering the chances of thrombosis. Similarly, short membranes reduce the volume of the sinus region, which also decreases stagnation.

We also focused on the issue in venous valves and whether it is mechanical stress or stagnation that favours cell agglomeration which may lead to thrombosis.

In order to compare the role of these two factors, we identified the location in the sinus with the highest stress and that with the highest stagnation. We placed an agglomeration seed in each of these two locations and implemented our agglomeration algorithm.

The growth of the agglomerate at the point of maximum stagnation was considerably higher than that at the point of maximal stress. This implies that, in the case of the venous valve, stagnation can be more important than mechanical stress in thrombus formation and propagation.

This result, combined with the fact that membrane flexibility and length determine the level of stagnation in the sinus, highlights the potential for personalised diagnostics in the fight against deep venous thrombosis. In principle, length and stiffness could be evaluated in clinical settings using existing diagnostic methods. Currently, they are not evaluated but based on our results, if they were added, in the future, to the toolkit of physicians they could, potentially, help predict the likelihood of DVT.

These data, in fact, could be introduced into the Discrete Multi-Physics model to predict, for that particular valve, the location of maximum stagnation and provide information that, potentially, could be converted into a probability of thrombus formation for a specific individual.

4.6 Notation and abbreviations

Notation

Z	Channel radius, m
L	Length of the membrane, m
R	Radius of the valve chamber, m
Y	Length of the valve chamber, m
E	Young modulus, kg m^{-1} s^{2}
F	Flexural rigidity, kg m^{3} s^{-2}
k_a	Angular Hookean coefficient, J
k_b	Bond Hookean coefficient, J m^{-2}
k_v	Viscous damping coefficient, kg s^{-1}
g	Acceleration, m s^{-2}
t	Time, s
T	Period, s
f	Oscillation frequency, s^{-1}
V	Velocity m s^{-1}
r_0	Equilibrium distance, m

θ_0	Equilibrium angle, rad
Δr	Initial distance, m
r^*	Repulsive radius, m
ρ	Density, kg m^{-3}
h	Smoothing length, m
c_0	Artificial sound speed, m s^{-1}
Tshear	Shear Stress, Pa
Ttot	Total mechanical stress, Pa
Ptot	Pressure, Pa
Vmag	Velocity, m s^{-1}
Δt	Time step, t
P	Agglomeration probability, (-)
R_{max}	Distance, m
N	Number of time step, (-)

Abbreviations

DVT	Deep Venous Thrombosis
PE	Pulmonary Embolism

VTE	Venous ThromboEmbolism
FSI	Fluid Structure Interaction
DMP	Discrete Multi Physics
DMHS	Discrete Multi-Hybrid System
SPH	Smoothed Particle Hydrodynamics
MD	Molecular Dynamics
MSM	Mass and Spring Model

CHAPTER 5: EMBOLI DYNAMICS IN FLEXIBLE VENOUS VALVES

5.1 Abstract

Emboli, which are parts of blood clots, can be stuck in the vasculature of various organs (most frequently, lungs) and cause their malfunction or even death. In this work, using mathematical modelling, different types of emboli-like structures are studied in a double venous valve system. The model is implemented with a fully Lagrangian Discrete Multi-Physics technique and the flow is governed by flexible walls. The study shows the effect of different diameters and lengths of a free embolus in the flow surrounding the valve. The presence of an embolus strongly affects the dynamics of both the fluid and the leaflets in venous valves and the permanence of the embolus in the valve chamber is narrowly linked with its length.

5.2 Introduction

An embolus is generally formed when a section of a thrombus detaches and circulates in the cardiovascular system until reaching narrow vessels, most frequently, in the lungs (Tapson 2008, Reitsma et al. 2012, MacIver et al. 2016). When emboli are trapped, they can obstruct blood flow to the lungs leading to a potentially life-threatening complication known as pulmonary embolism (PE) or deep vein thrombosis (DVT). In the UK alone, around 25,000 deaths are caused by PE or DVT; this number is five times higher than those from breast cancer, AIDS and road accidents combined (Hunt 2009).

While medical research highlights the role of DVT on the hydrodynamics around venous valves (Esmon 2009), the actual physical interaction of the embolus with the valve remains unexplored. The literature provides a wide range of publications about venous and arterial thrombosis, but the majority of these studies focuses on thrombogenesis and clotting (Zhang et al. 2002, Narracott et al. 2005, Ouared and Chopard 2005, Harrison et al. 2008, Hou et al. 2015, Diamond 2016, Simão et al. 2016, Ariane et al. 2017b, Carrascal et al. 2017), rather than the dynamics of the embolus.

To circumvent the current limitations of in-vivo and in-vitro models, computer simulations (in-silico modelling) of the venous valve have been carried out but, with a few exceptions (Abolfazli et al. 2014, Simão et al. 2016, Aycock et al. 2017), emboli are not accounted for. For DVT however, this represents a serious limitation since the presence of the embolus changes considerably the hydrodynamics around the valve.

Previous studies (Abolfazli et al. 2014, Aycock et al. 2017) have shown that the diameter, the elasticity and the location of an embolus affect the flow in arterial bifurcations (Abolfazli et

al. 2014) or in Inferior Vena Cava (IVC) (Aycock et al. 2017). But the interaction of the embolus with more complex settings such as the flexible leaflets of the venous valve has not been investigated. Only Simão et al. (2016) consider the presence of solid particles in the venous valve, but these are simple Lagrangian point particles and the flow, therefore, is not fully resolved around them.

By modelling the physical interaction of emboli with different shapes and flexibilities with the soft leaflets of the venous valve and the change of hydrodynamics that this involves, this study fills a gap in the literature since the valve environment is probably the most critical for DVT and the presence of clots in the vicinity of the valve has been associated with the occurrence of new thrombosis activation sites (Esmon 2009).

5.3 Methodology

5.3.1 Modelling

A hybrid approach, based on a particle framework, is implemented to model haemodynamics and solid structure deformation. The technique, called Discrete Multi-Physics (DMP) (Alexiadis et al. 2017, Ariane et al. 2017a, Ariane et al. 2017b), associates Smoothed Particle Hydrodynamics (SPH) (Monaghan 1994, Morris et al. 1997, Liu and Liu 2003) and the Mass and Spring Model (MSM) (Alexiadis 2014, Alexiadis 2015a, Alexiadis 2015b) and has been used to model the fluid-structure interactions occurring in deep vein valves (Ariane et al. 2017b), cardiac valves (Ariane et al. 2017a) and the intestine (Alexiadis et al. 2017).

In this approach, the liquid is represented by SPH particles that interact with each other by viscous and pressure forces and the tissues by MSM particles inter-connected by means of computational springs (to model the elastic modulus) and dashpots (to model viscoelasticity). The essential ideas behind the DMP method are summarized in Chapter 2; the reader can refer to (Alexiadis 2014) for a more extensive explanation of the DMP theory and to (Alexiadis 2015a) for applications in different fields such as lava flows, cell dynamics and solid-liquid flow.

5.3.2 Geometry

In this study, we use a 2D schematic representation of a double leg venous valve system. The geometry is similar to the short valve model used in Chapter 4 but here it is used with two antagonist valves (Fig. 5.1). The channel radius is Z = 0.004 m, the membrane length is L = 0.01m, the radius of the valve chamber is R = 0.007 m and its length is Y = 0.04 m (Ariane et al. 2017b). The two valve systems are inter-connected and the total length between the two

chambers is C = 0.048 m (0.046 m in (Wijeratne and Hoo 2008)). The external walls are divided into four parts: two flexible sections where an external force is applied (Channel 1 and Channel 2 in Fig. 5.1), and two valve chambers (Valve chamber 1 and Valve chamber 2 in Fig. 5.1) that contain the leaflets. Since periodic boundary conditions are enforced, the fluid exiting from the channel opening on the right is reinserted to the channel opening on the left and vice versa. For the same reason, Channel 1 in Fig. 5.1 appears to be divided into two sections (one on the left and another on the right), but, computationally, the two ends are joined together by the periodic boundary conditions. A net fluid flow is achieved by means of external forces acting alternatively on Channel 1 and Channel 2 (Fig. 5.1). When a 'squeezing' force F (see Fig. 5.1) is applied to Channel 1, Valve 1 opens, Valve 2 closes, and the fluid flows from the left to the right. When F is applied to Channel 2, Valve 2 opens, Valve 1 closes, and the fluid maintains the same direction from the left to the right. This approach mimics the actual motion of blood in the legs' veins induced by the contraction of the surrounding muscles.

In the rest of the study, we refer to the regions between the leaflets (in both Valve 1 and Valve 2) as the 'opening regions' and to the regions between the walls and the leaflets (in both Valve chamber 1 and Valve chamber 2) as 'sinus regions' (Fig. 5.1).

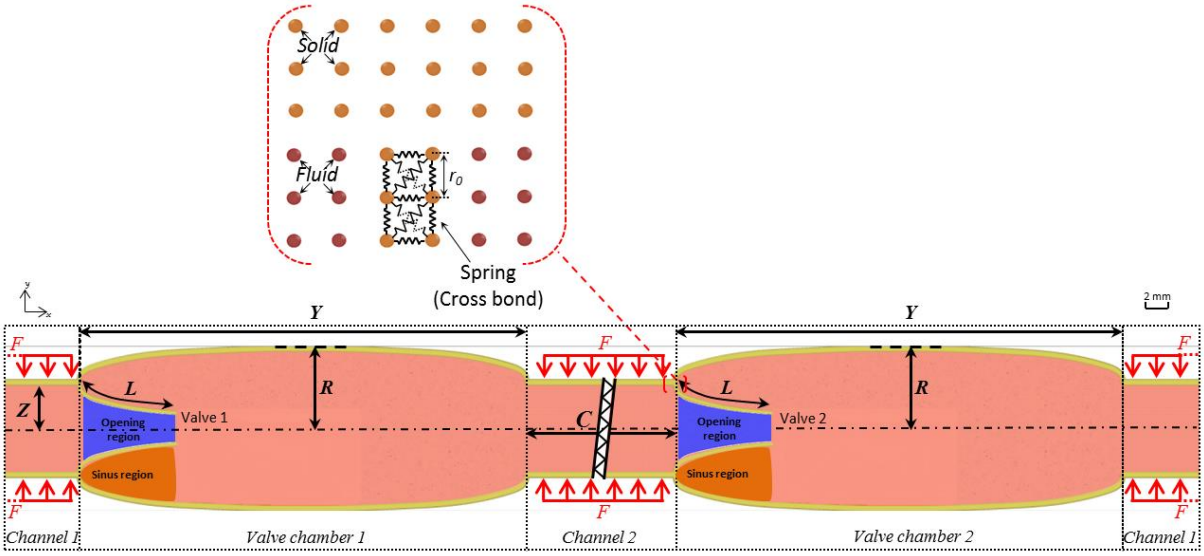

Fig. 5.1. Illustration of the double venous valve 2D geometry.

According to the DMP approach (see Chapter 2) both the fluid and the solid are represented by discrete computational entities, which we call 'fluid particles' and 'solid particles'. The different behaviour of fluid and solid particles depends on the type of forces the DMP algorithm applies to each computational particle. If these forces model the viscous and pressure forces commonly acting on fluids, the computational particle behaves like a fluid; if they model the viscoelastic forces acting on solid, the particle behaves like a solid. Computationally, the fluid forces are calculated with the SPH method while the solid forces particles by means of springs (MSM model) as detailed in section 2.4. The wall delimiting the valve chamber is considered stationary and, therefore, no forces are applied to the computational particle representing this part of the domain. Solid-liquid boundary conditions are also modelled by means of inter-particle forces that model no-penetration and no-slip conditions as explained in Chapter 2.

5.3.3 Model parameters

In our simulations, the geometry is divided into 168676 particles spaced of 10^{-4} m: 584 for the valves, 10722 for the walls, and 157370 for the fluid area. As mentioned, SPH particles are used for the fluid, stationary (solid) particles for the valve chamber walls and MSM particles for the flexible walls and the leaflets. Three layers of particles are used for the walls and two for each leaflet, with thicknesses of 3.10^{-4} m and 2.10^{-4} m, respectively. The flow is laminar and blood is here considered a Newtonian fluid. Table 5.1 gathers all the parameters used in the simulation.

Table 5.1. Model parameters used in the simulations.

SPH (Eqs. (2.12), (2.13), (2.14))	
Parameter	**Value**
Number of SPH wall particles (3 layers)	10722
Number of SPH valve particles (2 layers)	584 (146 particles/leaflet)
Number of SPH fluid particles	157370
Mass of each particle (fluid)	$1.05 \cdot 10^{-5}$ kg
Mass of each particle (solid)	$2 \cdot 10^{-5}$ kg
Initial distance among particles Δr	$1 \cdot 10^{-4}$ m
Smoothing length h	$2.5 \cdot 10^{-4}$ m
Artificial sound speed c_0	10 m s^{-1}
Density ρ_0	1056 kg m^{-3}
Viscosity μ_0	0.0035 Pa s
Time step Δt	10^{-6} s
Total time of each simulation*	32s (simulation), 48h (computation)
Force F	0.008 N
MSM (Eqs. (2.19), (2.21))	
Parameter	**Value**
Hookean coefficient k_b (Wall)	$1 \cdot 10^{5}$ J m^{-2}
Hookean coefficient k_b (membrane)	$5 \cdot 10^{6}$ J m^{-2}
Viscous damping coefficient k_v (Wall)	1 kg s^{-1}
Viscous damping coefficient k_v (membrane)	0.1 kg s^{-1}
Equilibrium distance r_0	$1 \cdot 10^{-4}$ m
BOUNDARIES (Eq. (2.28))	
Constant K	$4 \cdot 10^{-4}$ J
Repulsive radius r*	$1 \cdot 10^{-4}$ m
*dual-processor 8-core (16 cores/node, 2 nodes used) 64-bit 2.2 GHz Intel Sandy Bridge E5-2660	

5.3.4 Simulation parameters

The structure of the flexible tissue (wall and valve) and its elasticity are implemented with a spring model (section 2.4). The spring constant k_b has been chosen in order to model the different elastic properties of the leaflets and the walls (Table 5.1). A viscous coefficient (k_v) is also added to the MSM springs to confer viscoelastic properties to the valve and the flexible wall as in a Kelvin–Voigt material.

The inlet/outlet of the fluid in the x-direction is controlled using periodic boundary conditions. The flow is pulsed periodically and generates several opening and closing of the valves. Therefore, we use the term 'cycle' to define a single period including one opening and one closing of the same valve (Lurie et al. 2003, Wijeratne and Hoo 2008). For each cycle, we model the opening phase by applying a vertical force F (y-axis) on Channel 2 for 1.5 s while no force is applied to Channel 1 (Fig. 5.1). During the closing phase (1.5 s), Channel 2 is relaxed (F on Channel 2 is set to 0) and F is applied to Channel 1. The force F is constant and uniform for each cycle (Table 5.1). For all simulations, a total of 10 cycles (30 s) are calculated.

5.3.5 Emboli

A solid, embolus-like structure is introduced into the flow. The solid particles of the embolus are joined together by springs whose Hookean constant is reported in Table 5.2. Differently from the previous studies (Chapters 3 and 4) where the embolus grows due to an aggregation algorithm, here the embolus size is fixed during the simulation.

The effect of size, length and embolus' flexibility is investigated (Table 5.2). In the literature, no standard size or length for emboli is given and the shape mostly depends on the

surrounding flow, channel diameter and valve characteristics (Simão et al. 2016). In this work, to account for a variety of potential cases, the selected sizes are in the range used by (Aycock et al. 2017) and the lengths coincide with the length of (i) the sinus region (embolus L6 in Table 5.2), (ii) half of the valve chamber (embolus L19), (iii) the valve chamber (embolus L37) and (iv) the valve chamber + half of the channel (embolus L77).

Table 5.2. Simulation parameters used for the embolus aggregate.

Variation of the diameter of the embolus (spherical) with k_b = 1 10^4 J m^{-2}		
Diameter of the embolus [m]	Location at t = 0 s	Case
2.6 10^{-3} m	Centre of the tube	D26
5.2 10^{-3} m	Centre of the tube	D52
7.8 10^{-3} m	Centre of the tube	D78
Variation of the length of the embolus with height = 2.6 10^{-3} m and k_b = 1·10^4 J m^{-2}		
Length of the embolus [m]	Location at t = 0 s	Case
5.9 10^{-3} m	Sinus region	L6
19 10^{-3} m	Sinus region	L19
21 10^{-3} m	Centre of the tube	L21
37 10^{-3} m	Sinus region	L37
77 10^{-3} m	Sinus region	L77
Variation of the flexibility of the embolus (spherical) with diameter = 7.8 10^{-3} m		
Bond coefficient k_b [J m^{-2}]	Location at t = 0s	Case
1·10^3 J m^{-2}	Centre of the tube	F103

5.4 Results and discussion

5.4.1 Hydrodynamics

A typical simulation without the embolus is shown in Fig. 5.2. During the opening phase (of Valve 1), when *F* is applied to Channel 1, the pressure in Channel 1 increases; Valve 1 opens and Valve 2 closes (Fig. 5.2a and Fig. 5.2b). Part of the fluid leaves Channel 1 and accumulates in Channel 2, which dilates. During the closing phase (of Valve 1), the force *F* is applied to Channel 2 and Channel 1 relaxes (*F* is set to 0). Valve 1 closes while Valve 2 opens (Fig. 5.2c and Fig. 5.2d). The contraction and, therefore, the force applied to the vein walls account for the level of physical activity of a specific individual. The force used in this study generates a peak blood velocity around 0.035 m s^{-1} which corresponds to a low level of physical activity (Simão et al. 2016, Ariane et al. 2017b). This condition was chosen since the risk of DVT increases when the level of physical activity is low.

The valve opening-closing mechanism in relation to the contraction of the veins around the valve is confirmed by the available literature (Lurie et al. 2003, Wijeratne and Hoo 2008, Ariane et al. 2017b). At the time of maximal contraction, however, the vein assumes an asymmetrical shape shown in Fig. 5.2d. This is probably due to the fact that, in our model, the segments of veins (Channel 1 and Channel 2) connecting two valves are considerably shorter than in reality. The asymmetrical shape can neither be confirmed nor disproved by available visualization data. This circumstance, however, has little relevance to this work, which focuses on the dynamics of the valves rather than that of the veins.

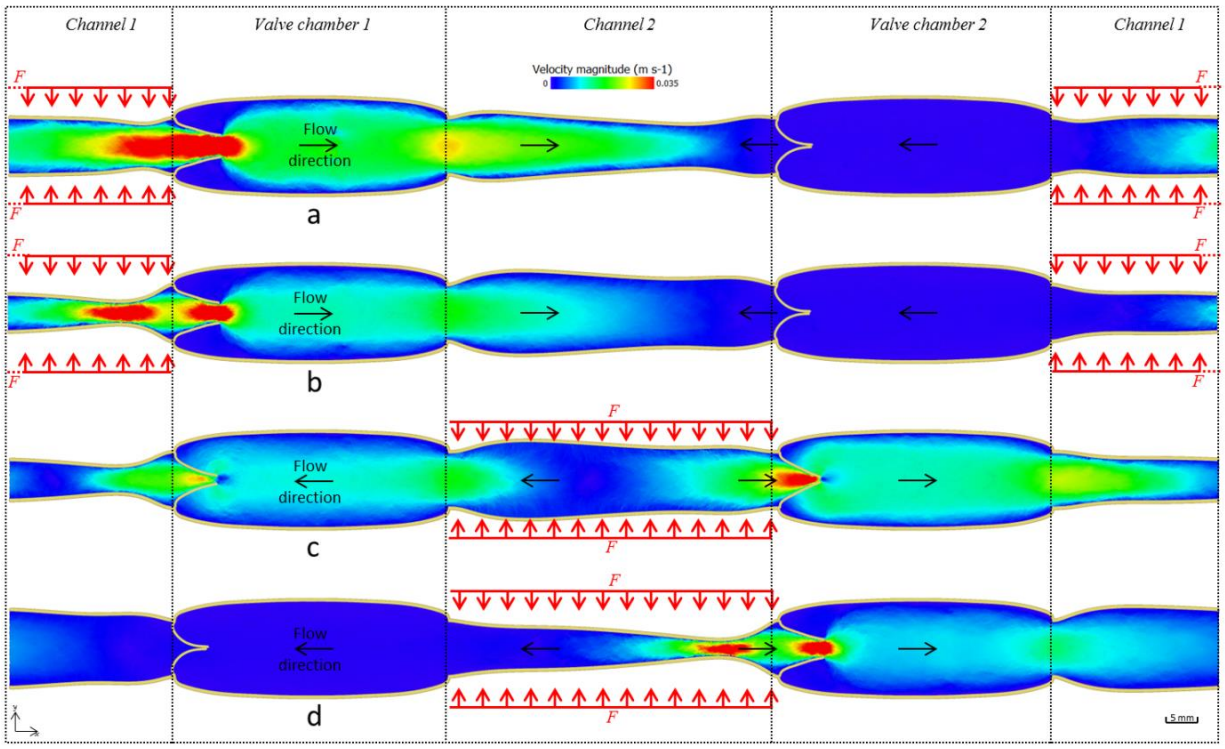

Fig. 5.2. Valve deformation and velocity magnitude of the system during a cycle: (a) t = 0 s, (b) t = 0.75 s, (c) t = 1.5 s, (d) t = 2.25 s, (e) t = 3 s.

In the next section, we introduce an embolus-like structure both in the main flow (opening region in Fig. 5.1) and behind the valve (sinus region in Fig. 5.1). The goal is to show how the presence of a free embolus impacts the flow in the vicinity of the valve.

As mentioned, three parameters are investigated in this case: size, length and flexibility of the aggregate (Table 5.2).

5.4.2 Embolus displacement in the opening region

Initially, three circular emboli with diameters of 2.6 10^{-3} m (Case D26 in Table 5.2), 5.2 10^{-3} m (D52) and 7.8 10^{-3} m (D78) are introduced into the flow (Fig. 5.3a). In the first case (Fig. 5.3b), the embolus is too small for impacting the flow and crosses the valve with no contact with the leaflets. No significant difference with the pure fluid case is observed.

In the second case (Fig. 5.3c), although the embolus diameter is bigger than the valve opening, it can cross the valve because of its flexibility and the deformation of the leaflets. The embolus is elastic (Abolfazli et al. 2014) and recovers its initial shape after the valve. However, contrary to the first case, the flow surrounding the embolus is considerably affected by the presence of the embolus and two vortexes form around the valve.

In the third case (Fig. 5.3d), the embolus is bigger than the inlet valve chamber and despite the large deformation of both the embolus and the valve, the embolus cannot cross the valve.

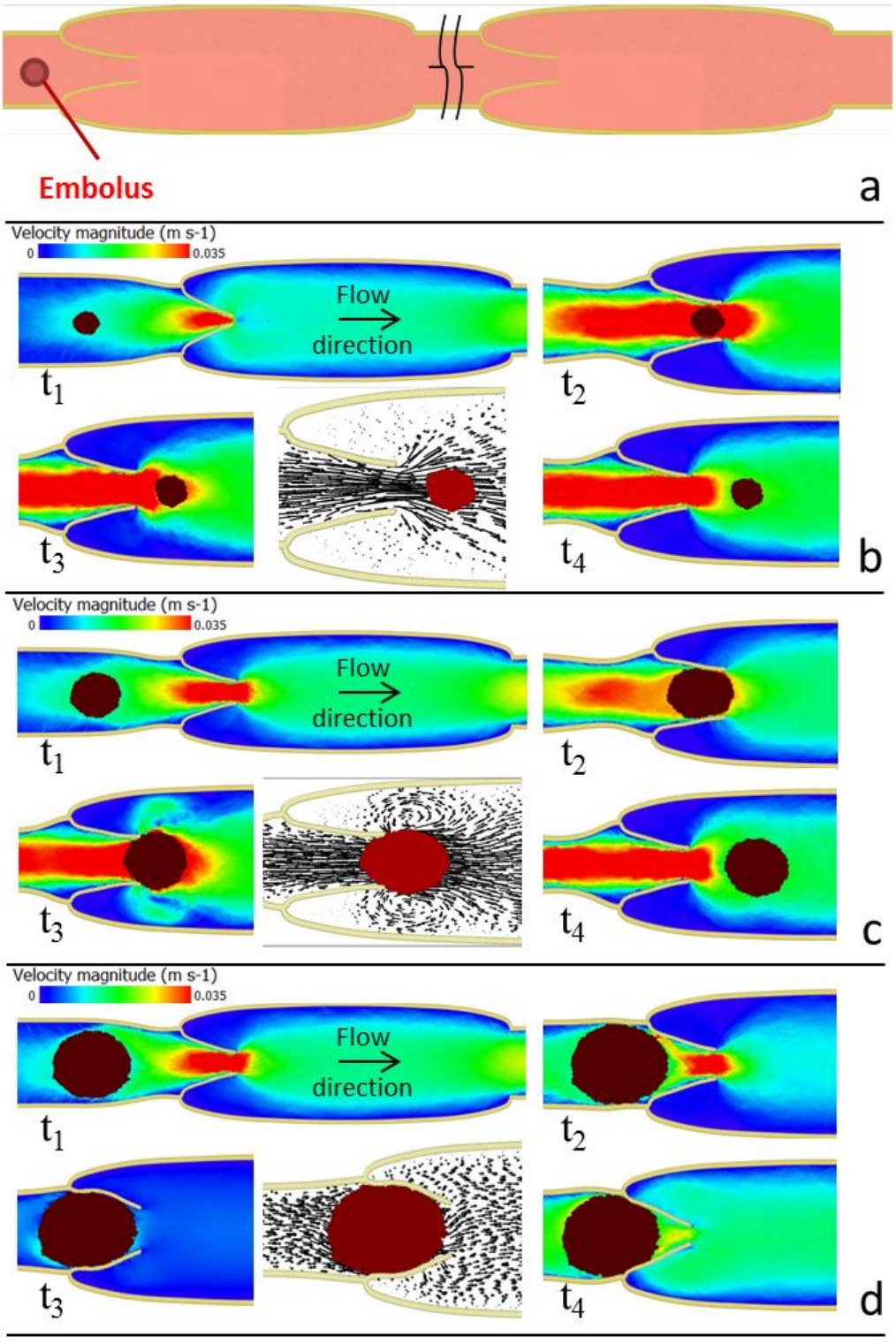

Fig. 5.3. Embolus position and velocity vectors at different times: a) t = 0 s for all emboli, b) embolus D26, c) embolus D52, and d) embolus D78.

In reality, the embolus obstruction observed in Fig. 5.3d would probably resolve itself after a certain time since, normally, the level of physical activity of individual changes during the day (Collins et al. 1988), while in our simulation we only considered low physical activity. In our simulations, a similar situation (i.e. an embolus, initially stuck, crosses the valve after several cycles) occurs when the flexibility of the embolus is higher (Fig. 5.4).

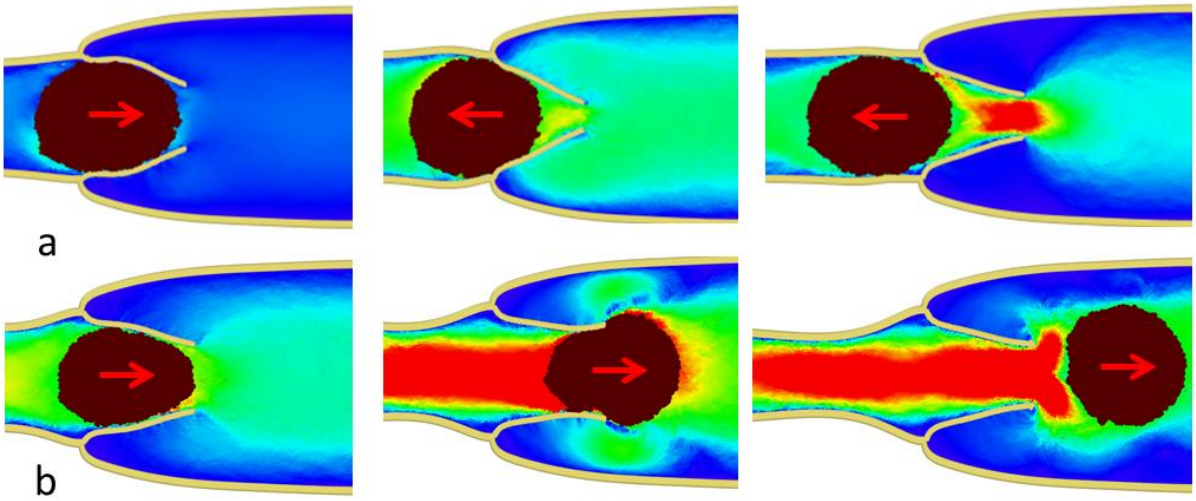

Fig. 5.4. Embolus of diameter 7.8 10^{-3} m with different elasticity: a) kb = 1 10^{4} J m^{-2} (D78) and b) kb = 1 10^{3} J m^{-2} (F103).

The vortexes observed in Fig. 5.3c and Fig. 5.4 are larger if the length of the embolus is longer as in Fig. 5.5. In this case, both the flow and the valve behaviour are considerably altered by the presence of the 'sausage-like' embolus.

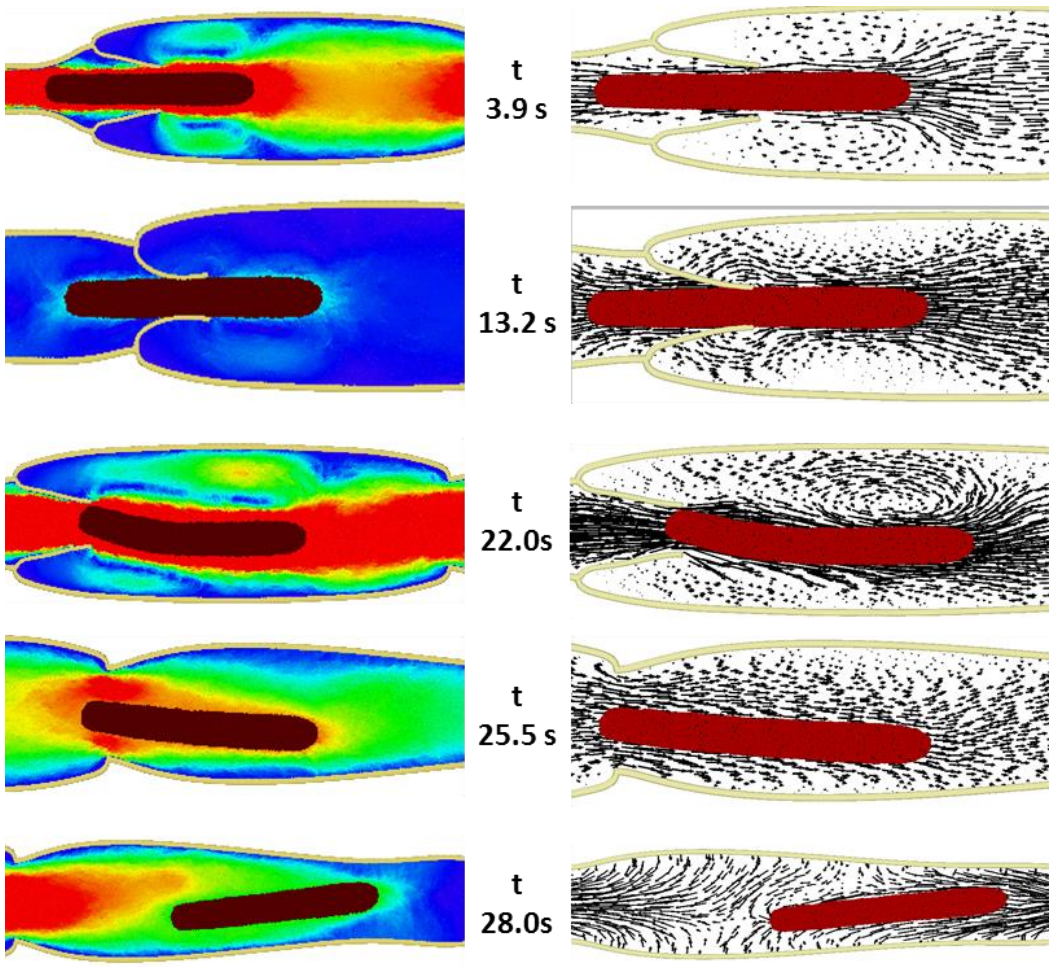

Fig. 5.5. Velocity magnitude and vectors of the flow and circulation of the embolus (L21) at different times.

5.4.3 Embolus displacement in the sinus region

In this section, an embolus is located behind Valve 1 (sinus region in Fig. 5.1). In the medical literature, it is not completely clear where emboli form, but they are often found in the sinus region. After they reach a certain size, they leave the sinus region and move in the cardiovascular system. In this section, we show how the length of the embolus can affect its permanence in the sinus region. Four emboli with different lengths are simulated (Table 5.2): 5.9 mm (L6 in Table 2), 19 mm (L19), 37 mm (L37) and 77 mm (L77) and located in the sinus region (Fig. 5.6a).

Fig. 5.6b and Fig. 5.6c show no significant displacement of embolus L6 and embolus L19 after 10 cycles while embolus L37 (Fig. 5.6d) and L77 (Fig. 5.6e) show a high displacement. In fact, each embolus interacts with the fluid in a different way. The longer the embolus, the higher the drag force that the liquid exchange with the embolus. This force, however, is not simply proportional to its length, but it also depends on the local velocity at the location of the embolus.

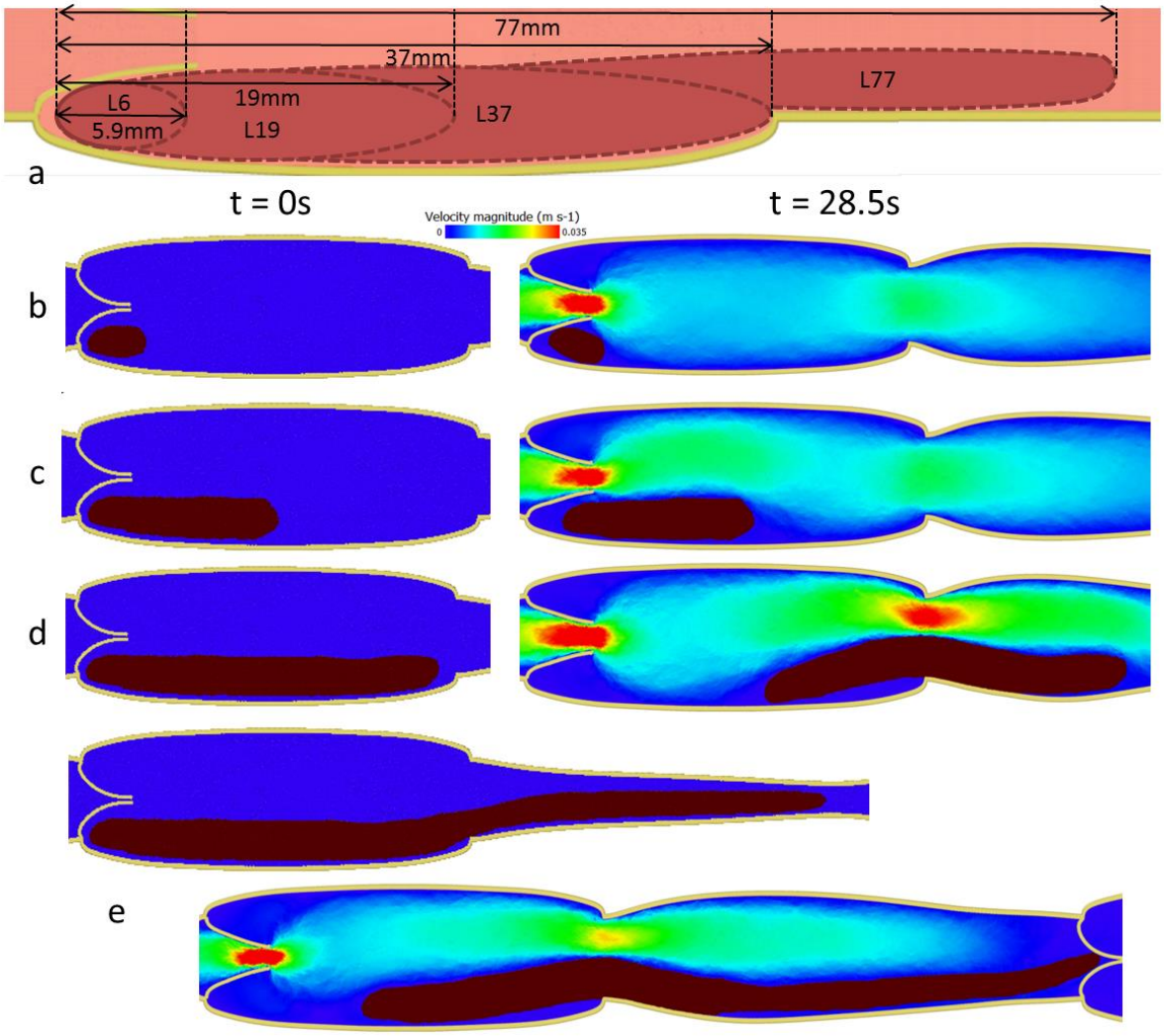

Fig. 5.6. Embolus position at t = 0 s and t = 28.5 s for a) L6, b) L19, c) L37, d) L77.

In Fig. 5.7, embolus displacement versus the simulation time indicates that the displacement values oscillate every cycle (forward and backward embolus motion). Embolus L6 never moves and only spins around itself (Fig. 5.6b) due to its 'circular' shape. While embolus L19 begins to move slowly after 20 s. In both cases, the emboli remain in the low flow area (Fig. 5.8) where the flow velocities are the lowest. On the other extreme, embolus L77 continually moves because the most of the embolus is located in the main flow area (Fig. 5.8). The displacement of L37 is initially smaller than L77 because a lower fraction is in contact with the high velocity area. However, once it is dragged away from the left end of the sinus it is more easily captured by the main flow due to its smaller size.

The different results show that the flexibility of emboli can play a paramount role in the localisation of embolism diseases. If the embolus is flexible enough, it can cross successive valve sections without any resistance and therefore, the embolism phenomena are likely located in very small channels like in the lungs (so-called pulmonary embolism). Conversely, if the embolus is rigid, the embolism phenomena are likely located in the valve environment, in particular, where the flow is minimal. Additionally, according to medical observations (Chueh et al. 2011), the rigidity of the embolus increases with its lifetime in the vein system, and in cases of a very long lifetime, the embolus can also disaggregate itself with contact with valve and generate smaller emboli which will reach the lung network more easily.

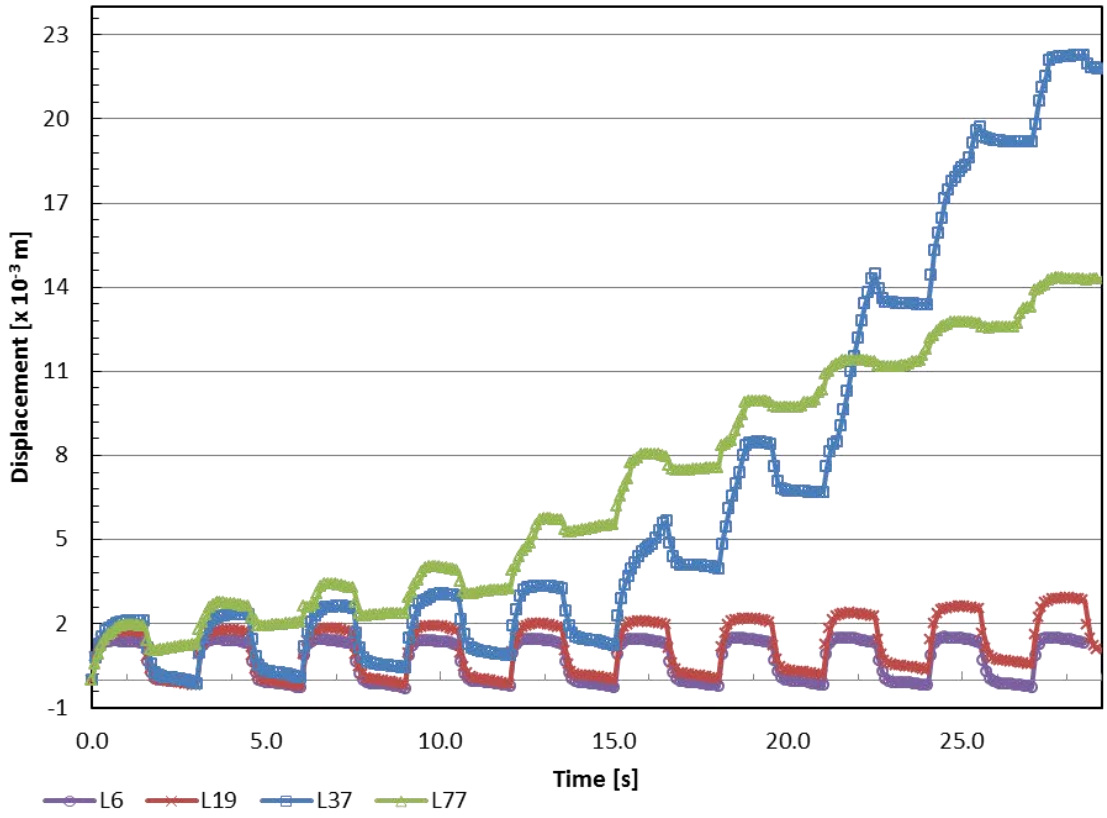

Fig. 5.7. Time evolution of the local displacement for embolus L6, L19, L37, and L77.

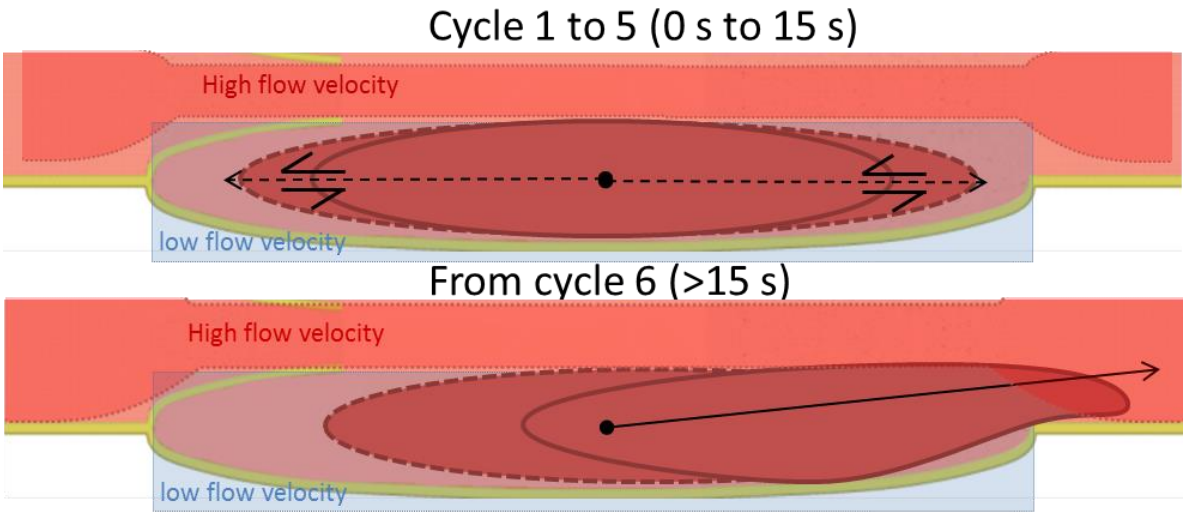

Fig. 5.8. Schematic of embolus L37 movement in low flow region and high flow region before and after 15s.

5.5 Conclusions

Free emboli circulation in a valve environment has been studied using the Discrete Multi-Physics approach. We modelled both fluid and emboli dynamics as well as the leaflets deformation. In the previous studies (Chapters 3 and 4), an inlet fluid velocity was used to ensure the blood motion within the rigid channel, while here, the flow is governed by muscle contractions.

The results show that emboli with a size bigger than the valve can still cross the valve if they are flexible enough. This observation can be linked with the age of emboli in the body since the elasticity of an embolus depends on its lifetime in the blood system (Chueh et al. 2011), and the older the embolus the lower its flexibility.

The embolus length plays also a paramount role. In the main flow (opening region), the embolus can potentially generate new vortex area that can further favour platelets aggregation. In the low flow (sinus region), the length of the embolus determines how long it takes for the embolus to detach from the sinus region and move within the main flow.

The main conclusion of this work is that the presence of an embolus strongly affects the dynamics of both the fluid and the leaflets in venous valves. Therefore, computer simulations designed to support fundamental research in DVT should account for emboli if they aim at a more realistic description of reality.

5.6 Notation and abbreviations

Notation

Z	Channel radius, m
L	Length of the membrane, m
R	Radius of valve chamber, m
Y	Length of valve chamber, m
C	Channel length between the two valve system, m
ρ_0	Density, kg m^{-3}
U_{bond}	Interatomic bond potential, N
k_b	Bond Hookean coefficient, J m^{-2}
k_v	Viscous damping coefficient, kg s^{-1}
F	Force applied to walls, N
h	Smoothing length, m
Δr	Initial distance among particles, m
r_0	Equilibrium distance, m
c_0	Artificial sound speed, m s^{-1}
Δt	Time step, s

μ_0	Fluid viscosity, Pa s

Abbreviations

PE	Pulmonary Embolism
DVT	Deep Vein Thrombosis
VTE	Venous Thromboembolism
IVC	Inferior Vena Cava
DMP	Discrete Multi-Physics
SPH	Smoothed Particle Hydrodynamics
MSM	Mass and Spring Model

CHAPTER 6: DIFFUSIVE AND CONVECTIVE MASS TRANSFER IN BOUNDARY LAYERS CONTAINING MOTILE CILIA IN LUNGS

6.1 Abstract

In this chapter, the mass transfer coefficient (permeability) of boundary layers containing motile cilia is investigated by means of Discrete Multi-Physics. The idea is to understand the main mechanisms of mass transport occurring in a ciliated-layer; one specific application being inhaled drugs in the respiratory epithelium. The effect of drug diffusivity, cilia beat frequency and cilia flexibility is studied. Our results show the existence of three mass transfer regimes. A low frequency regime, which we called shielding regime, where the presence of the cilia hinders mass transport; an intermediate frequency regime, which we have called diffusive regime, where diffusion is the controlling mechanism; and a high frequency regime, which we have called convective regime, where the degree of bending of the cilia seems to be the most important factor controlling mass transfer in the ciliated-layer. Since the flexibility of the cilia and the frequency of the beat changes with age and health conditions, the knowledge of these three regimes allows prediction of how mass transfer varies with these factors.

6.2 Introduction

Motile cilia are hair-like structures present on the surface of a variety of cells. They are in large numbers in the human body and beat in coordinated waves to perform a number of different functions. For instance, in the conducting and central airways of the lungs, cilia are surrounded by mucus that traps particulate materials and pathogens. The coordinated motion of the cilia propels these materials towards the pharynx where they are swallowed or expelled via coughing, a phenomenon known as mucociliary clearance or mucociliary escalator (Agnew et al. 1986). Mathematical modelling of this phenomenon has attracted the interest of various researchers in material, biological and pharmaceutical sciences. The main motivation is to understand the factors controlling the effectiveness of mucociliary clearance since this is important in the context of environmental exposure (see (Smith et al. 2008) for a detailed review). For instance, Barton and Raynor (1967) introduced an analytical model of a mucus layer with cilia motion. Their findings suggested that the mucus flow in contact with the airway is governed by a viscosity gradient in the mucus layer, but in their work, the cilia were only considered as rigid rods. Later, Blake (1984) implemented a more realistic cilia motion model including effective and recovery stroke in a two layers system. The outcomes highlighted the role of the cilia penetration (in the mucus layer) on the mucus transport effectiveness. At the beginning of the new century, Mauroy et al. (2011) focused their researches on the mucus draining in an idealised rigid bronchial tree with an air flow effect. Their model showed the viscosity-dependence of the mucus transport as well as the important role of the geometry. The emergence of the Immersed Boundary Method (IBM) has allowed a significant enhancement in mucociliary clearance modelling. Lee et al. (2011) investigated the effects of the velocity, the viscosity, the beat cilia frequency, the number of cilia and the depth

of the periciliary layer. The main results showed that (i) the velocity of the periciliary fluid is linearly proportional to the cilia beat frequency, (ii) the mucus viscosity plays a little role on the mucus flow rate contrary to the number of cilia which increases the mucus transport, and (iii) a minimum depth of periciliary layer is needed to generate a mucociliary transport. Jayathilake et al. (2012) extended the two-dimensional (Lee et al. 2011) model to a three-dimensional representation and thus were able to capture the cilia motion in the normal direction; they confirmed the previous results. Additionally, the same authors in another publication (Jayathilake et al. 2015), focused on cilia dysfunction and malformation. They emphasized the negative effects of too elastic and too rigid cilia beat patterns on the mucus transport. Then, a method coupling IBM with a lattice Boltzmann method was used by (Sedaghat et al. 2016) to implement an Oldroyd-B model and to simulate a viscoelastic fluid. They found that an increase of the mucus viscosity accelerates the motion of the mucus layer. Chatelin et al. (2017), with a penalty technique, also concentrated their researches on genetic cilia diseases and defective mucus clearance using a non-Newtonian model. They correlated, in the case of cystic fibrosis, the mucus velocity and rheology with a mucus maturation model and spotted that shear-thinning mucus can accentuate agglomeration phenomena in regions with ineffective clearance. Most of the previous studies have focused on the altered effectiveness of mucociliary clearance under disease states, for example in primary or acquired ciliary dyskinesia. Here, we also take a look how impairments to the ciliary function can modify the speed with which pollutants, irritants and toxic agents can reach the airway epithelium.

While mucociliary escalator is one of the major defence mechanisms protecting the lungs, it has a significant role in pulmonary drug delivery. In the case of inhaled aerosolized medicines, mucociliary clearance competes with the particle dissolution and absorption that

eventually determines the lung bioavailability of the inhaled drugs (Olsson et al. 2011). Smaller particles trapped in the mucus layer progressively dissolve and diffuse towards the epithelium and the drug gets absorbed (Fig. 6.1a). On the other hand, larger or slowly dissolving particles are incompletely cleansed by the cilia, hence decreasing the absorption rate of the drug (Fig. 6.1b). Mucociliary clearance concerns the mass transfer of particles trapped in the mucus layer to the pharynx for clearance, whilst the drug absorption depends on the diffusion of particles towards the epithelium through the mucus and the ciliated-layer. The role that the cilia beat pattern plays as part of the mucociliary clearance mechanism has been studied in the past. While the cilia beat is also likely to affect mass transfer, to the best of our knowledge, it has received no attention in the literature from this perspective.

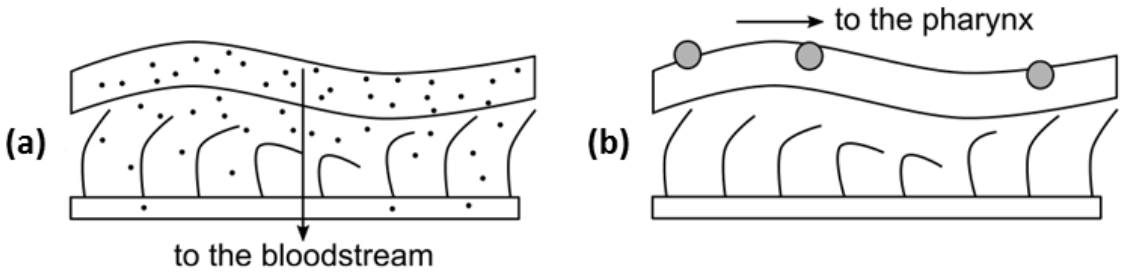

Fig. 6.1. Drug absorption (a) versus mucociliary clearance (b).

In this work, we use a modelling technique called Discrete Multi-Physics (Alexiadis 2014, Alexiadis 2015a, Alexiadis 2015b, Alexiadis et al. 2017, Ariane et al. 2017a, Ariane et al. 2017b) to investigate how the motion of the cilia affects mass transfer conditions in the ciliated-layer. By means of Discrete Multi-Physics, the following research questions are addressed. Does the presence of the cilia enhance or hinder the mass transfer in the ciliated layer? For example, it is known that smoking, age, and health conditions affect the frequency of the cilia beat (Leopold et al. 2009). Thus, it is of interest to understand how drug

absorption is sensitive to the frequency of the beat. Finally, does the flexibility of the cilia, which also depends on age and health conditions (Boucher 2007), play a role too?

Answering these questions can provide insights not only to the development of inhalation medicines , or to the dynamics of harmful chemicals during environmental exposure, but also the design of artificial cilia needed for lab-on-a-chip or organ-on-a-chip applications (Wang et al. 2015).

6.3 Preliminary considerations and background

6.3.1 Cilia beat

In the past, several studies (Aiello and Sleigh 1977, Sanderson and Sleigh 1981, Marino and Aiello 1982, Gheber and Priel 1997, Chilvers and O'Callaghan 2000, Chilvers et al. 2003b, Chilvers et al. 2003a) have investigated the cilia motion in the respiratory epithelium. The results are not always fully consistent with each other (e.g. Fig. 6.2), but in general, the cilia motion is divided into two phases: an ‘effective stroke’, in which the cilia move forward and propel the mucus layer in the same direction; and a ‘recovery stroke’, in which the cilia recover their initial position.

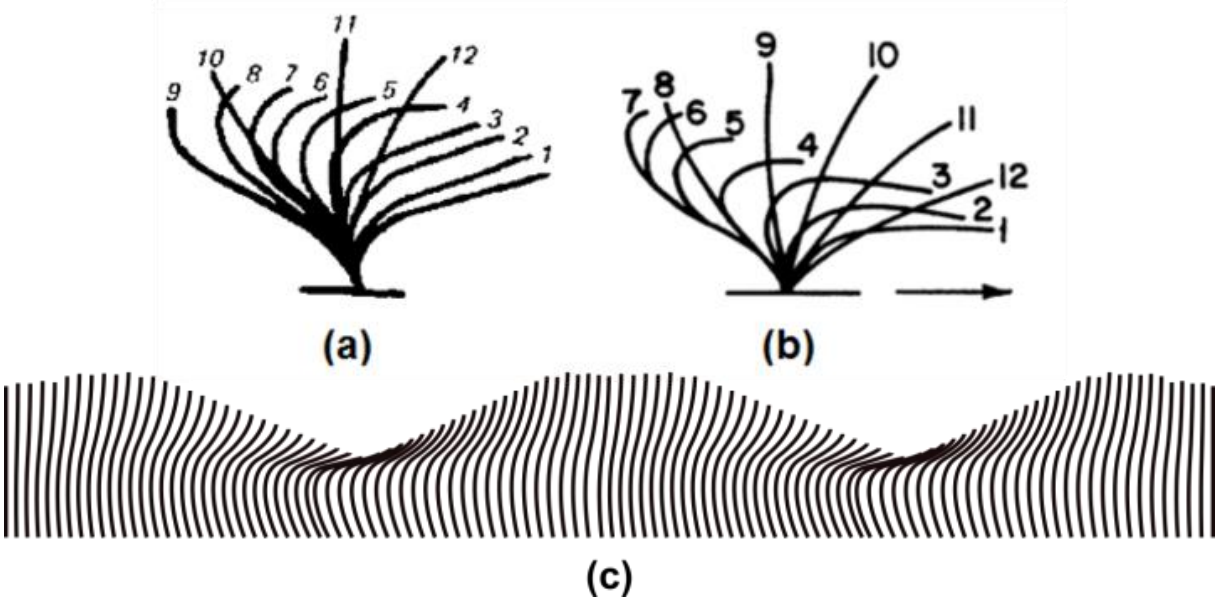

Fig. 6.2. Cilium's motion according to (a) Sanderson and Sleigh (1981) and (b) Aiello and Sleigh (1977) and (c) metachronal wave.

Moreover, the movement of each cilium (Fig. 6.2) is coordinated with that of the others producing a wave-like overall motion known as a metachronal wave. A variety of cilia beat frequencies in the range between 3 and 20 Hz have been observed in the respiratory epithelium, with the frequency being a function of temperature, age and health conditions. Artificial cilia used in lab-on-a-chip applications, on the other hand, can reach higher frequencies in the order of 50 Hz (Fahrni et al. 2009).

6.3.2 Membrane permeability and mass transfer

In the case of certain drugs, the absorption rate depends on the permeability P_{me} of the cellular membrane to that specific drugs. In experiments, the drug's flux through the membrane J is measured and the permeability calculated from

$$J = P_{me}(c_1 - c_2), \tag{6.1}$$

where $c_2 - c_1$ is the difference of drug's concentration across the membrane (Fig. 6.3a).

If before permeating the membrane, the drug diffuses through an additional mass transfer resistance (e.g. the layer of mucus), the total permeability P_{TOT} of the mucus + the membrane layer is given by

$$\frac{1}{P_{TOT}} = \frac{1}{P_{me}} + \frac{1}{P_{mu}}, \tag{6.2}$$

where P_{mu} is the drug's permeability of the mucus layer.

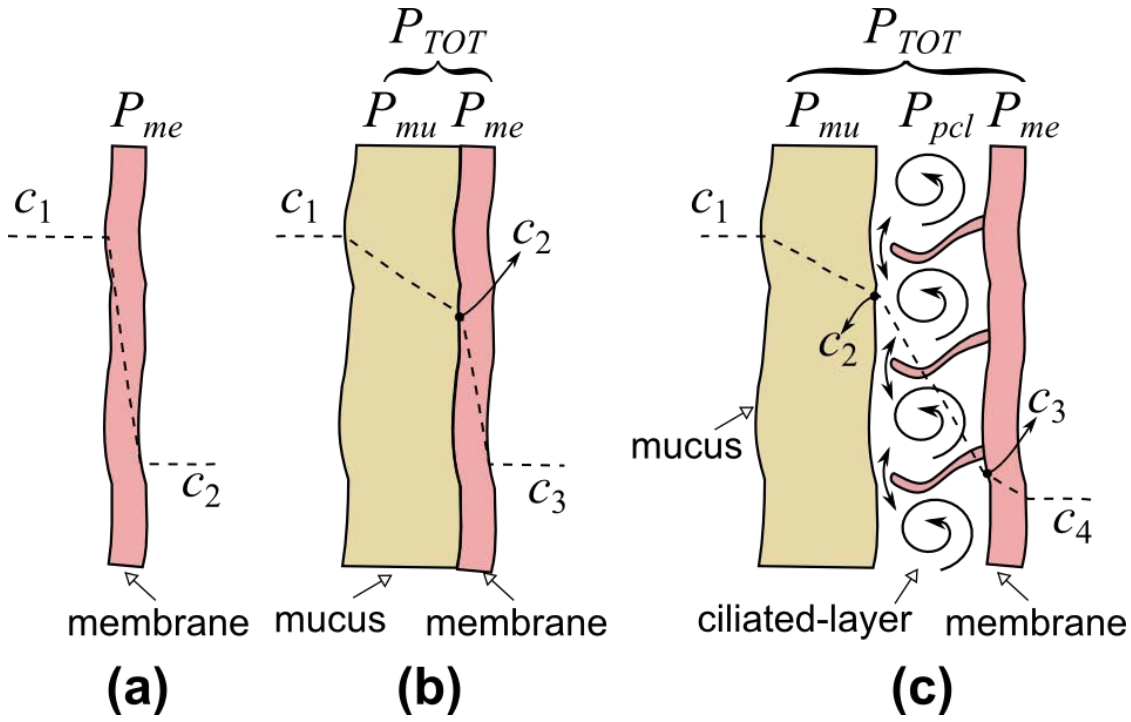

Fig. 6.3. Permeability through a membrane (epithelium), (b) permeability through a membrane + a mucus, (c) permeability through a membrane + a mucus + a ciliated-layer.

In the respiratory epithelium, between the mucus layer and the membrane, there is a third layer, the periciliary layer (PCL), where a low-viscosity fluid is agitated by motile cilia. The overall permeability of the mucus + ciliated + membrane layer is, therefore,

$$\frac{1}{P_{TOT}} = \frac{1}{P_{me}} + \frac{1}{P_{mu}} + \frac{1}{P_{pcl}}, \tag{6.3}$$

where P_{pcl} is the permeability of the ciliated−layer.

Permeability is the term mostly used in biology and medicine; in physics and engineering, it is often replaced by the molecular diffusivity D, which is linked to permeability by the relation

$$P = \frac{D}{\delta}, \tag{6.4}$$

where δ is the thickness of the layer where the drug diffuses. There is, however, a fundamental difference between mass transfer in the membrane or in the mucus layer, and in the PCL. The diffusivities D_{me} (membrane) and D_{mu} (mucus) originate from hydrodynamically static layers and only depend on the molecular interaction between the diffusing drug and the diffusive medium; they can be measured from standard experiments, which do not depend on hydrodynamics. The PCL, on the other hand, is hydrodynamically active since the motion of the cilia generates recirculation regions where mass transfer depends on convection rather than diffusion. Under certain conditions, discussed in Section 6.4.3, however, the dynamics can be considered pseudo-diffusive and an apparent diffusivity coefficient D_{pcl} can be used to model the mass transport in the ciliated-layer. This means that Eq. (6.3) can be rewritten as

$$\frac{\delta_{TOT}}{D_{TOT}} = \frac{\delta_{me}}{D_{me}} + \frac{\delta_{mu}}{D_{mu}} + \frac{\delta_{pcl}}{D_{pcl}}, \tag{6.5}$$

While D_{me} and D_{mu} are real diffusivities, which are constant for a given drug, D_{pcl} is a pseudo-diffusivity, which also depends on the motion of the cilia. The goal of this study is to determine how the pseudo-diffusivity D_{pcl} is affected by the three parameters: (i) the molecular diffusivity D of the drug in the periciliary fluid, (ii) the frequency f of the cilia beat, and (iii) the flexibility of the cilia measured as bending length s covered by the cilia during bending.

6.3.3 Soluble versus insoluble particles

Inhalation devices release medicines to the airways in the form of fine solid particles (typically in the range of 2 to 6 μm) or liquid droplets (aerosols). Particles that dissolve in the mucus gradually diffuse and reach the epithelium (Section 6.3.2). As discussed earlier, the fate of insoluble particles depends on their size. For particles larger than 6 μm, the mucociliary clearance process is active and the mucus layer traps and eliminates these particles. Particles smaller than 6 μm, instead, can penetrate the mucus layer and diffuse similarly to molecules of soluble drugs. Their diffusivity D_B is the result of Brownian motion and can be calculated according to the Stokes-Einstein relation

$$D_B = \frac{k_B T}{3\pi\mu a}, \tag{6.6}$$

where k_B is the Boltzmann constant, T the temperature, μ the viscosity of the fluid and a the diameter of the particle. Based on Eq. (6.6), in our analysis, we can treat soluble particles and

small insoluble particles in the same way. The only difference being that the latter case requires the Brownian diffusivity D_B instead of the molecular diffusivity D.

6.4 Methodology

6.4.1 Modelling

To determine how the pseudo-diffusivity D_{pcl} depends on the molecular diffusivity, the beat frequency and the flexibility of the cilia, we use a computational approach called Discrete Multi-Physics (DMP) that links various discrete (i.e. particle based) modelling techniques in order to reach results not attainable with each technique separately. This method has been successfully tested for both solid-liquid flows (Alexiadis 2014, Alexiadis 2015a, Alexiadis 2015b) and fluid-structure interaction (Alexiadis et al. 2017, Ariane et al. 2017a, Ariane et al. 2017b). In this study, Smoothed Particle Hydrodynamics (SPH) is used to simulate the fluid, and the Mass and Spring Model (MSM) to simulate the membrane. A brief introduction to SPH and MSM is given in Chapter 2 and more details can be found in the aforementioned publications.

6.4.2 Geometry

Many modelling works on mucociliary clearance follows a 2D representation of the ciliated-layer (see (Smith et al. 2008) for a review); in this study, we also follow this approach. The computational domain (Fig. 6.4a) is divided into four regions: the mucus, the PCL, the cilia and the membrane. SPH particles are used to model the mucus and the PCL, MSM particles are used to model the cilia, while static SPH particles are used for the membrane. In the following, we refer to the particles used for the cilia as cilia-particles, to the particles used to model the mucus layer as mucus-particles and so on. The computational box is shown in Fig.

6.4b. There are 36 cilia with length L_{pcl} = 5 μm each, the distance between cilia is l = 0.5 μm and the total length of the section investigated is W = 20 μm; since periodic boundary conditions in the x-direction are considered, each particle whose position is $x < 0$ or $x > W$ is reintroduced on the other side of the computational box. The actual computational domain, therefore, is defined as an infinite replica in the x-direction of the computational box illustrated in Fig. 6.4b. The thickness of the mucus layer in the simulation is H_{mu} = 2 μm, which is lower than the actual mucus layer (typically 3-5 μm (Eixarch et al. 2010)). In this study, this is not a limitation since we are mostly interested in the mass transport in the PCL and the mucus layer is only used for the concentration at the boundary conditions. A smaller mucus layer requires less computational particles and allows faster simulations.

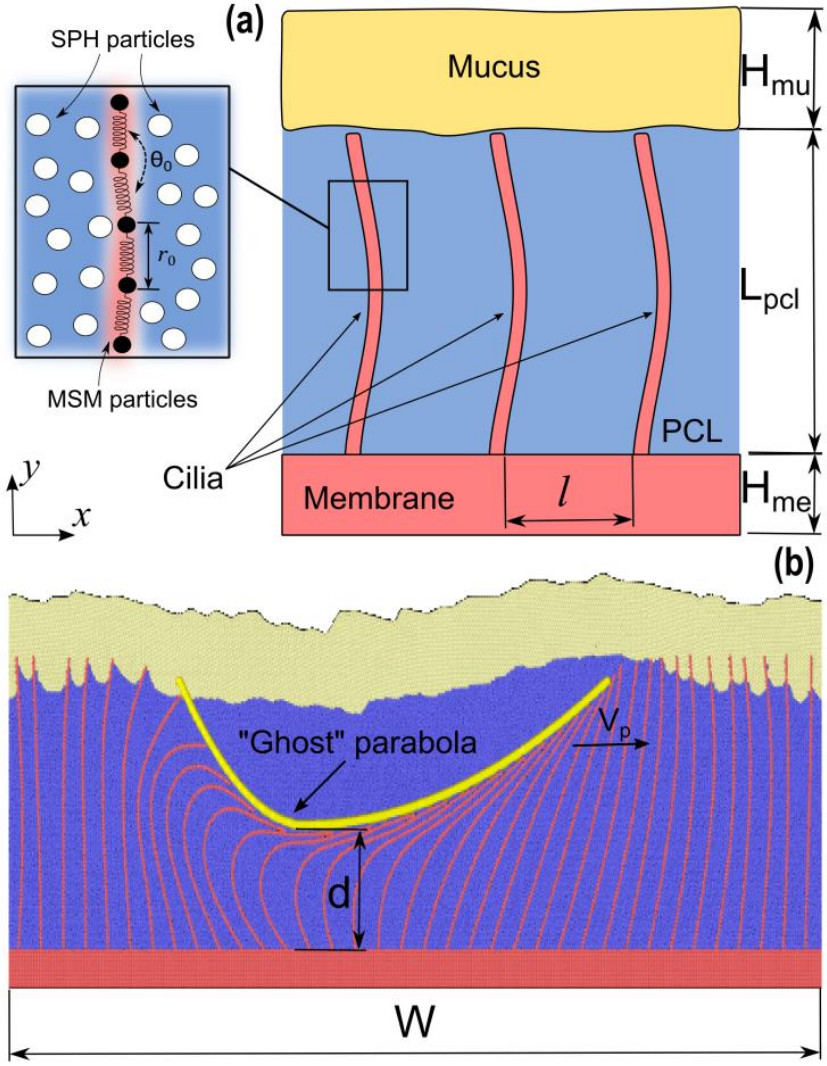

Fig. 6.4. The geometry of the PCL (a) and the computational box used in the simulations (b).

Modelling the metachronal wave of the cilia turned out to be a challenging task. If only a few cilia are considered, a series of time-dependent forces can be imposed on the cilia-particles resulting in an approximately correct bending and straigtening motion of each cilium. When the number of cilia is above four or five, however, the interaction with the fluid produces a gradual loss of coordination among the cilia that, as time progresses, breaks the metachronal rhythm. We have tried a number of different strategies to overcome this problem; the best

solution we found consists of using a fifth type of 'ghost' particles that only interact, by means of a soft repulsive force with the cilia as

$$f(r) = K_s\left[1 + cos\left(\frac{\pi.r}{r^*}\right)\right], \tag{6.7}$$

With K_s a constant chosen arbitrarily according to the simulations.

These particles are arranged in a parabolic shape that moves horizontally (see Fig. 6.4b). The PCL fluid and the mucus do not feel the presence of these 'ghost' particles (no interaction forces), but if the parabola comes into contact with a cilium, the cilium bends and follows the outline of the parabola (interaction forces). When the parabola moves away, the cilium gradually recovers its original shape. In this way, the coordination of the metachronal wave is maintained for all duration of the simulation and the shapes obtained are consistent with those observed in the literature (Fig. 6.2). Given the periodic boundary conditions explained above, when the parabola exits the domain from $x = W$, it is re-introduced at $x = 0$. The velocity of the parabola v_P and the length of the domain W determine the frequency of the beat (i.e. $f = v_P/W$). The 'ghost' parabola is also used to investigate the effect of the flexibility of the cilia. During their motion, the cilia periodically bend and straighten and the degree of bending is an indication of how flexible the cilia are. By varying the distance d between the minimum of the parabola and the epithelium (Fig. 6.4b) we can vary the bending length and simulate cilia with different flexibilities. In the rest of the study, we refer at the distance $s = L_{pcl} - d$ as the bending length.

6.4.3 Dimensionless analysis

Our aim is to determine how the pseudo-diffusivity D_{pcl} depends on D, f and s. Dimensionless analysis indicates that the system can be described by only two dimensionless groups. The Sherwood number is defined as

$$Sh = \frac{D_{pcl}}{D}, \tag{6.8}$$

which expresses the ratio between the molecular and the apparent diffusivity; and the Péclet number that, here, works as a dimensionless frequency

$$Pe = \frac{s^2 f}{D}. \tag{6.9}$$

In our results, therefore, we seek correlations of the type

$$Sh = KPe^n, \tag{6.10}$$

where K and n are two constants to be determined from the simulation data.

In the following sections, we will also use the geometric ratio

$$\lambda = \frac{s}{L_{pcl}}, \tag{6.11}$$

which is not a fundamental dimensionless group, but it will be used, during the discussion, to highlight some specific aspects that depend on the cilia flexibility.

6.5 Results and discussion

There are two types of parameters required for the simulations: model parameters and simulation parameters. Model parameters define the SPH, MSM and DMP structures and are fixed in all the simulations (Table 6.1).

Table 6.1. Model parameters used in the simulations.

SPH (Eqs. (2.12), (2.13), (2.14),	
Parameter	**Value**
Number of membrane particles (10 layers)	3270
Number of PCL particles	19788
Number of mucus particles N_{mucus}	7050
Number of cilium particles (36 cilia)	2592 (72 particles/cilium)
Length of the membrane L_{me}	$0.6\ 10^{-6}$ m
Number of Ghost parabola particles (1 layer)	343
Mass of each particle	$4.3.\cdot10^{-12}$ kg
Initial distance among particles Δr	$6.6\cdot10^{-8}$ m
Smoothing length h	$1.98\cdot10^{-7}$ m
Artificial sound speed c_0	0.25 m s^{-1}
Density of PCL ρ	1000 kg m^{-3}
Density of mucus ρ	1000 kg m^{-3}
Dynamic viscosity of PCL μ	$1\ 10^{-3}$ Pa s
Dynamic viscosity of mucus μ	20 Pa s
Time step Δt	10^{-8} s
Total time of each simulation*	0.08s (simulation), 36h (computation)
MSM (Eqs. (2.19) and (2.20))	
Parameter	**Value**
Angular coefficient k_a	$1.0\ 10^{-12}$ J
Hookean coefficient k_b	20 J m^{-2}
Equilibrium distance r_0	$6.6\cdot10^{-8}$ m
BOUNDARIES (Eq. (2.28) and (6.7))	
Constant K	$5\ 10^{-16}$ J
Constant Ks	$8\ 10^{-15}$ J
Repulsive radius r*	$1.65\ 10^{-7}$ m
*dual-processor 8-core (16 cores/node, 2 nodes used) 64-bit 2.2 GHz Intel Sandy Bridge E5-2660	

Simulation parameters such as D, f and s, represent the operative conditions and are varied as indicated in Table 6.2.

Table 6.2. List of simulations with diffusivities, frequencies and bending lengths parameters.

Case	D [m^2 s^{-1}]	f [Hz]	s [µm]	λ [-]	Pe [-]	D_{PCL} [m^2 s^{-1}]	Sh [-]
D10v05H3	$1\ 10^{-10}$	2.5	1.3	0.27	0.04	$3.08\ 10^{-11}$	0.31
D10v05H4	$1\ 10^{-10}$	2.5	1.9	0.38	0.09	$3.00\ 10^{-11}$	0.30
D10v05H5	$1\ 10^{-10}$	2.5	2.5	0.50	0.16	$3.04\ 10^{-11}$	0.30
D10v05H6	$1\ 10^{-10}$	2.5	3.1	0.62	0.24	$3.14\ 10^{-11}$	0.31
D10v1H3	$1\ 10^{-10}$	5.0	1.3	0.27	0.09	$3.06\ 10^{-11}$	0.31
D10v1H4	$1\ 10^{-10}$	5.0	1.9	0.38	0.18	$2.98\ 10^{-11}$	0.30
D10v1H5	$1\ 10^{-10}$	5.0	2.5	0.50	0.32	$3.01\ 10^{-11}$	0.30
D10v1H6	$1\ 10^{-10}$	5.0	3.1	0.62	0.47	$3.14\ 10^{-11}$	0.31
D10v2H3	$1\ 10^{-10}$	10.0	1.3	0.27	0.18	$3.05\ 10^{-11}$	0.30
D10v2H4	$1\ 10^{-10}$	10.0	1.9	0.38	0.36	$2.97\ 10^{-11}$	0.30
D10v2H5	$1\ 10^{-10}$	10.0	2.5	0.50	0.63	$3.03\ 10^{-11}$	0.30
D10v2H6	$1\ 10^{-10}$	10.0	3.1	0.62	0.95	$3.21\ 10^{-11}$	0.32
D11v05H3	$1\ 10^{-11}$	2.5	1.3	0.27	0.45	$3.59\ 10^{-12}$	0.36
D11v05H4	$1\ 10^{-11}$	2.5	1.9	0.38	0.90	$3.81\ 10^{-12}$	0.38
D11v05H5	$1\ 10^{-11}$	2.5	2.5	0.50	1.58	$4.21\ 10^{-12}$	0.42
D11v05H6	$1\ 10^{-11}$	2.5	3.1	0.62	2.37	$4.46\ 10^{-12}$	0.45
D11v1H3	$1\ 10^{-11}$	5.0	1.3	0.27	0.89	$3.57\ 10^{-12}$	0.36
D11v1H4	$1\ 10^{-11}$	5.0	1.9	0.38	1.79	$3.88\ 10^{-12}$	0.39
D11v1H5	$1\ 10^{-11}$	5.0	2.5	0.50	3.16	$4.41\ 10^{-12}$	0.44
D11v1H6	$1\ 10^{-11}$	5.0	3.1	0.62	4.75	$4.92\ 10^{-12}$	0.49
D11v2H3	$1\ 10^{-11}$	10.0	1.3	0.27	1.79	$3.77\ 10^{-12}$	0.38
D11v2H4	$1\ 10^{-11}$	10.0	1.9	0.38	3.59	$4.00\ 10^{-12}$	0.40
D11v2H5	$1\ 10^{-11}$	10.0	2.5	0.50	6.32	$4.52\ 10^{-12}$	0.45
D11v2H6	$1\ 10^{-11}$	10.0	3.1	0.62	9.50	$5.21\ 10^{-12}$	0.52
D12v2H3	$1\ 10^{-12}$	10.0	1.3	0.27	17.88	$5.31\ 10^{-13}$	0.53
D12v2H4	$1\ 10^{-12}$	10.0	1.9	0.38	35.87	$5.75\ 10^{-13}$	0.58
D12v2H5	$1\ 10^{-12}$	10.0	2.5	0.50	63.15	$6.94\ 10^{-13}$	0.69
D12v2H6	$1\ 10^{-12}$	10.0	3.1	0.62	94.99	$8.58\ 10^{-13}$	0.86
D11v10H3	$1\ 10^{-11}$	50.0	1.3	0.27	8.94	$3.90\ 10^{-12}$	0.39
D11v10H4	$1\ 10^{-11}$	50.0	1.9	0.38	17.94	$4.41\ 10^{-12}$	0.44
D11v10H5	$1\ 10^{-11}$	50.0	2.5	0.50	31.58	$5.27\ 10^{-12}$	0.53
D11v10H6	$1\ 10^{-11}$	50.0	3.1	0.62	47.49	$6.33\ 10^{-12}$	0.63
D10v0H3	$1\ 10^{-10}$	0.0	1.3	0.27	0.00	$3.12\ 10^{-11}$	0.31
D10v0H4	$1\ 10^{-10}$	0.0	1.9	0.38	0.00	$3.06\ 10^{-11}$	0.31
D10v0H5	$1\ 10^{-10}$	0.0	2.5	0.50	0.00	$3.06\ 10^{-11}$	0.31
D10v0H6	$1\ 10^{-10}$	0.0	3.1	0.62	0.00	$3.17\ 10^{-11}$	0.32
D11v0H3	$1\ 10^{-11}$	0.0	1.3	0.27	0.00	$3.61\ 10^{-12}$	0.36
D11v0H4	$1\ 10^{-11}$	0.0	1.9	0.38	0.00	$3.71\ 10^{-12}$	0.37
D11v0H5	$1\ 10^{-11}$	0.0	2.5	0.50	0.00	$3.86\ 10^{-12}$	0.39
D11v0H6	$1\ 10^{-11}$	0.0	3.1	0.62	0.00	$3.99\ 10^{-12}$	0.40
D12v0H3	$1\ 10^{-12}$	0.0	1.3	0.27	0.00	$6.38\ 10^{-13}$	0.64
D12v0H4	$1\ 10^{-12}$	0.0	1.9	0.38	0.00	$6.53\ 10^{-13}$	0.65
D12v0H5	$1\ 10^{-12}$	0.0	2.5	0.50	0.00	$6.48\ 10^{-13}$	0.65
D12v0H6	$1\ 10^{-12}$	0.0	3.1	0.62	0.00	$6.32\ 10^{-13}$	0.63
D12v10H3	$1\ 10^{-12}$	50.0	1.3	0.27	89.38	$7.65\ 10^{-13}$	0.76
D12v10H4	$1\ 10^{-12}$	50.0	1.9	0.38	179.36	$9.10\ 10^{-13}$	0.91
D12v10H5	$1\ 10^{-12}$	50.0	2.5	0.50	315.76	$1.17\ 10^{-12}$	1.17
D12v10H6	$1\ 10^{-12}$	50.0	3.1	0.62	474.94	$1.67\ 10^{-12}$	1.67
D10v10H3	$1\ 10^{-10}$	50.0	1.3	0.27	0.89	$3.36\ 10^{-11}$	0.34
D10v10H4	$1\ 10^{-10}$	50.0	1.9	0.38	1.79	$3.61\ 10^{-11}$	0.36
D10v10H5	$1\ 10^{-10}$	50.0	2.5	0.50	3.16	$3.97\ 10^{-11}$	0.40
D10v10H6	$1\ 10^{-10}$	50.0	3.1	0.62	4.75	$4.22\ 10^{-11}$	0.42
D10v5H3	$1\ 10^{-10}$	25.0	1.3	0.27	0.45	$3.05\ 10^{-11}$	0.30
D10v5H4	$1\ 10^{-10}$	25.0	1.9	0.38	0.90	$3.10\ 10^{-11}$	0.31
D10v5H5	$1\ 10^{-10}$	25.0	2.5	0.50	1.58	$3.36\ 10^{-11}$	0.34
D10v5H6	$1\ 10^{-10}$	25.0	3.1	0.62	2.37	$3.61\ 10^{-11}$	0.36

6.5.1 Metachronal wave and velocity profiles

The focus of this work is on mass transfer, but, since convection, which depends on the local velocity pattern, is an important means of mass transfer, in this section, we discuss the typical velocity profiles obtained from the simulations. Fig. 6.5a shows the shape of the metachronal wave obtained in the simulations by using the 'ghost parabola' approach. Concerning the velocity profile (Fig. 6.5b), the most important feature for convective mass transport is the large recirculation region occurring where the cilia bend. Higher velocities appear in other regions, but these are confined within adjacent cilia and, as explained in Section 6.5.2, they do not significantly increase mixing in the ciliated-layer. The penetration of the cilia in the mucus layer is approximately 0.5 μm, which is consistent with values in the literature (Sanderson and Sleigh 1981). The velocity of the mucus layer in our calculations is around 10 μm s^{-1}, which is consistent with the values reported in the literature (typically ranging from 10 − 60 μm s^{-1}) (Oldenburg et al. 2012).

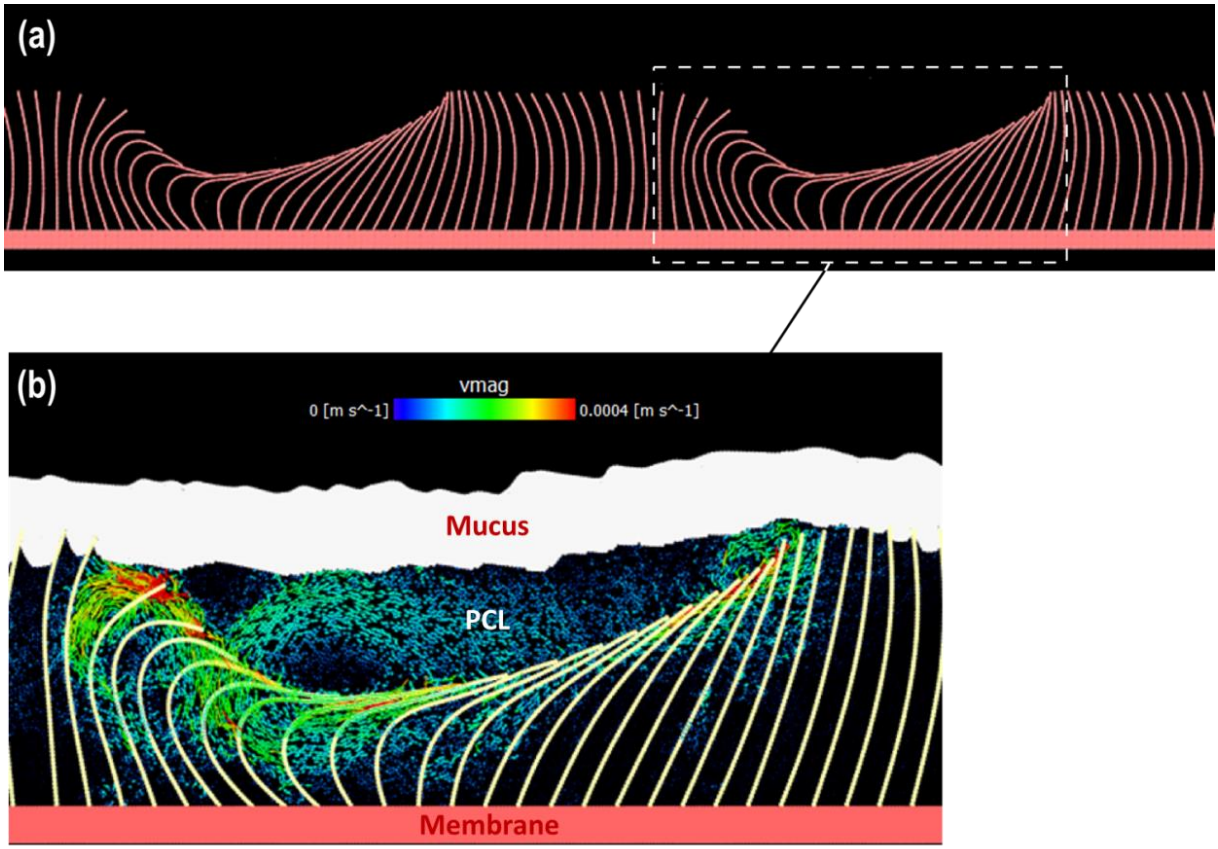

Fig. 6.5. Metachronal wave (a) and velocity profiles (b) for $D = 10^{-11}$ m^2 s^{-1}, $f = 10$ Hz and $s = 2.5$ μm.

6.5.2 Concentration profiles

In order to study the mass transfer within the PCL, we include in our model the equation of mass conservation of a chemical species A. How this is introduced in the Discrete Multi-Physics model is explained in Chapter 2 (additional details are given in (Alexiadis 2015a)). A typical concentration profile is shown in Fig. 6.6.

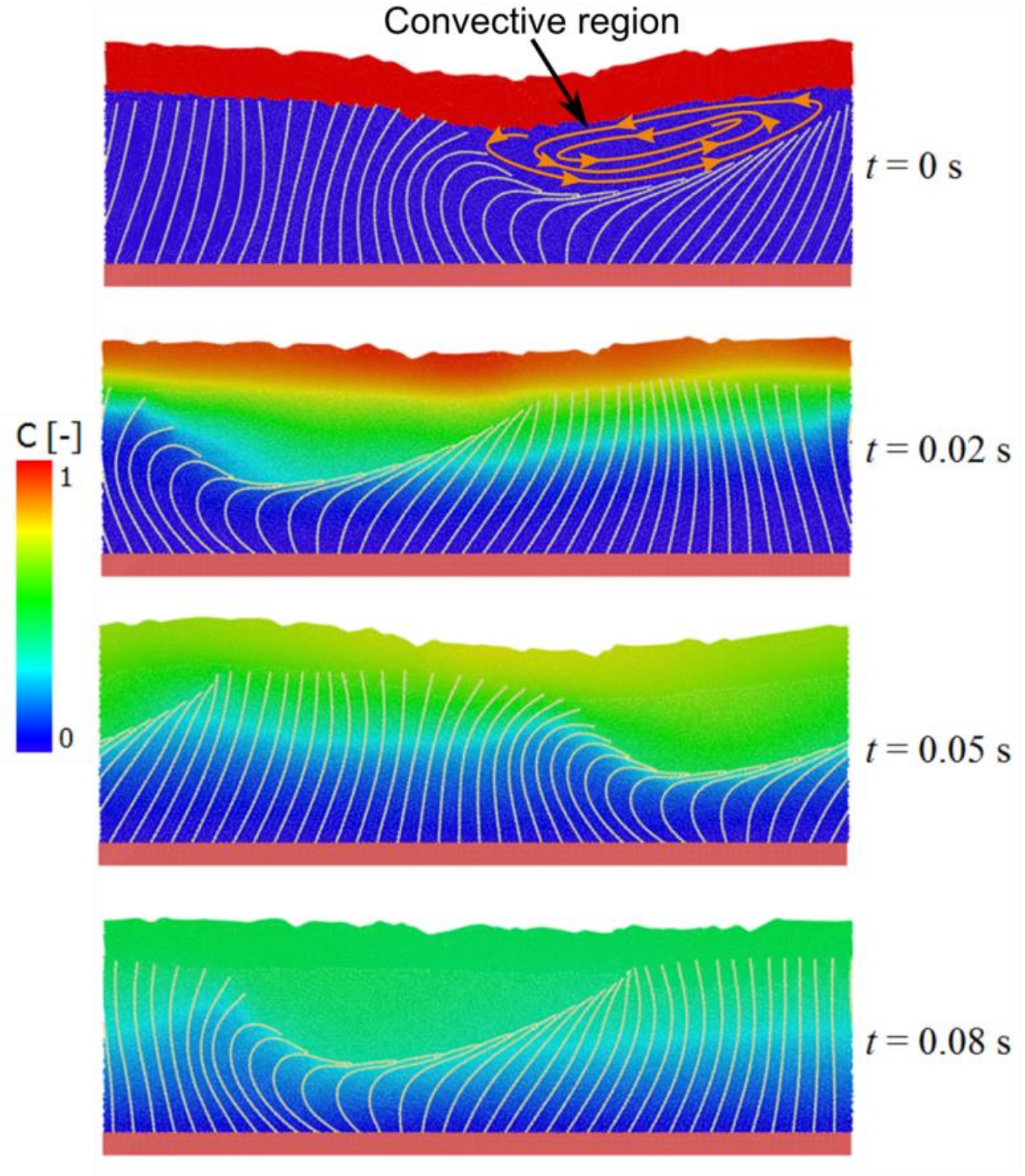

Fig. 6.6. Concentration profiles of the chemical species A at different time steps ($D = 10^{-11}$ m^2 s^{-1}, $f = 10$ Hz, $s = 2.5$ μm).

As the *metachronal wave* moves in the PCL, the bending of the cilia generates an empty region (free of cilia), called 'convective region' in Fig. 6.6, with characteristic size s, below

the mucus layer. This region has a large recirculation pattern that increases convective mass transport. Fig. 6.6 shows the effect of convection on a typical concentration profile. Initially, we assume all the drug is fully dissolved in the mucus layer and diffused in the PCL layer from there. The initial (dimensionless) drug concentration, therefore, is zero in the PCL and 1 in the mucus layer. The diffusivity of the drug is arbitrarily considered 10 times faster in the mucus than in the PCL, while the membrane is considered a passive wall with no mass exchange with the PCL. These boundary conditions allow for an effective calculation of D_{pcl} as explained in the next section.

6.5.3 Calculation of D_{pcl}

In order to calculate D_{pcl}, we need the instantaneous concentration profiles in the y-direction, which are calculated by averaging the concentration over the x-coordinate (Fig. 6.7a). Mass transfer in the PCL depends on a combination of diffusion and convection, however, under certain conditions the dynamics can be considered pseudo-diffusive and an apparent diffusivity coefficient D_{pcl} can be used to model mass transport in the ciliated-layer. We also assume that diffusivity of the drug is substantially larger than in the PCL and we stop our simulation before the drug reaches the membrane. The usefulness of these assumptions can be understood from Eq. (6.3) and Fig. 6.3. From our simulations, we can only measure the total permeability P_{TOT} of the system. However, we want to calculate the permeability of the ciliated layer P_{pcl}. If we arbitrarily set the permeability in the mucus high, $1/P_{mu}$ in Eq. (6.3) can be neglected and, if we stop the simulation before the drug reaches the membrane, $1/P_{me}$ can neglect. Under these circumstances, therefore, $P_{TOT} \sim P_{pcl}$ and, by measuring P_{TOT} we estimate P_{pcl}. This is a sort of numerical 'trick', it has nothing to do with the real drug diffusion in the mucus but allows to correctly estimate P_{pcl}. Once P_{pcl} is known, realistic

values of P_{TOT} can be calculated from Eq. (6.3) by introducing the actual values of P_{me} and P_{mu}.

Under the assumptions discussed above, the time-dependent concentration profiles in the PCL follow the formula (Bird et al. 2002)

$$c = c_{max} e^{-\frac{y^2}{4D_{pcl}t}}, \tag{6.12}$$

where c_{max} is the (time-dependent) concentration at $y = 0$, which depends on the total mass of drug dissolved in the mucus at the beginning of the simulation and decays with time as $t^{0.5}$.

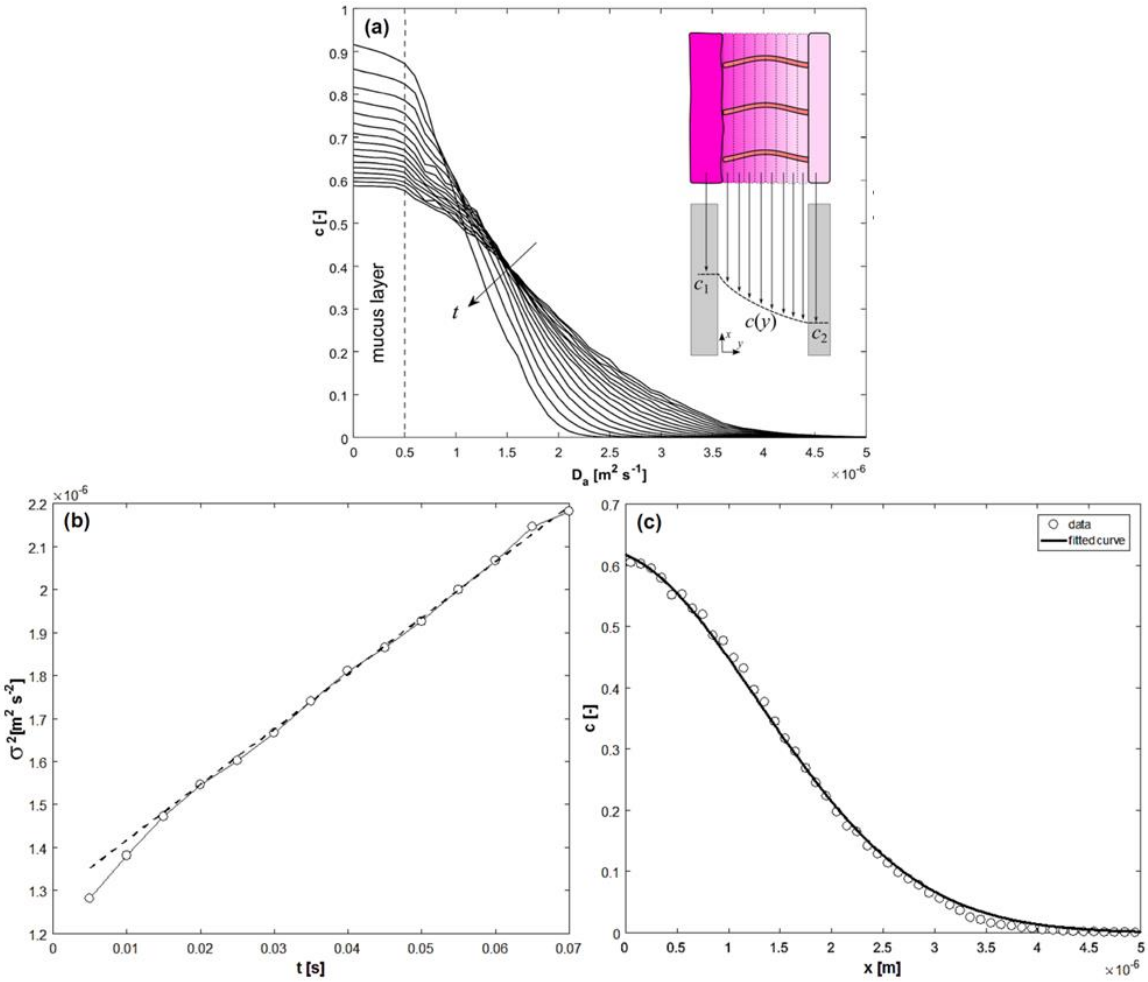

Fig. 6.7. Instantaneous concentration profiles in the *y*-direction (a), variance of the concentration versus time (b) and Gaussian fitting of the concentration profile at $t = 0.08$ s (c) for the case $D = 10^{-11}$ m^2 s^{-1}, $f = 10$ Hz, $s = 2.5$ μm.

Given Eq. (6.12), we can calculate the value of D_{pcl} from the concentration profiles of Fig. 6.7a. We compute the (time-dependent) variance σ^2 of each concentration profile, which, if the assumptions behind Eq. (6.12) are valid, should change linearly with time (Fig. 6.7b). The slope of Fig. 6.7b, therefore, gives the numerical value of D_{pcl}. The pseudo-diffusive hypothesis implies that the concentration profiles are approximately Gaussian, this is verified

in Fig. 6.7c for the specific case of $D = 10^{-11}$ m^2 s^{-1}, f = 10 Hz, s = 2.5 μm. The same procedure for the calculation of D_{pcl} is used for all the cases calculated in Table 6.2.

6.5.4 Shielding

Fig. 6.8 shows how the Sherwood number changes with f and λ in the case of $D = 10^{-11}$ m^2 s^{-1}. $Sh < 1$ implies that the pseudo-diffusivity in the PCL is lower than the drug's molecular diffusivity. This behaviour may look surprising at a first glance since convection can only increase mixing and, therefore, it is not clear how the pseudo-diffusivity of the PCL can be lower than the drug's molecular diffusivity.

The presence of the cilia, however, creates obstacles to the free motion of the drug in the fluid and, therefore, reduces the apparent mass transfer in the PCL. We have named this phenomenon shielding and indicate with D_{0pcl} the lowest apparent diffusivity, which occurs at $f \rightarrow 0$ where no convective mixing is present. As f increases, the convective motion enhances mass transfer and compensates the shielding effect as discussed in the next section

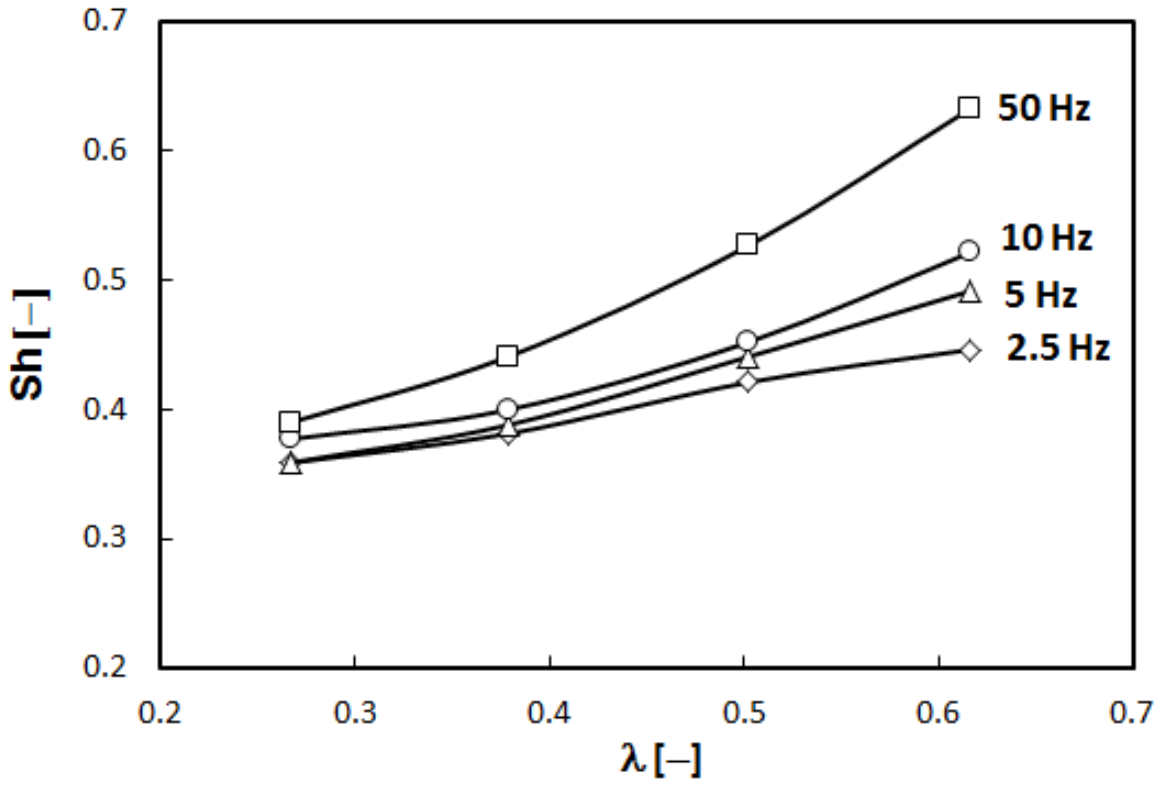

Fig. 6.8. Sherwood number for $D = 10^{-11}$ m^2 s^{-1} and various values of f and λ.

6.5.5 Mass transfer regimes

In Fig. 6.9 (*Sh* vs. *Pe*), we can distinguish three regions. Each of these regions is characterized by different values of K and n in Eq. (6.10). We are interested, in particular, in the exponent n and, therefore, we rewrite Eq. (6.10) as

$$D_{PCL} \propto s^{2n} f^n D^{1-n}. \tag{6.13}$$

Each value of n can be associated with a different mass transfer dynamics.

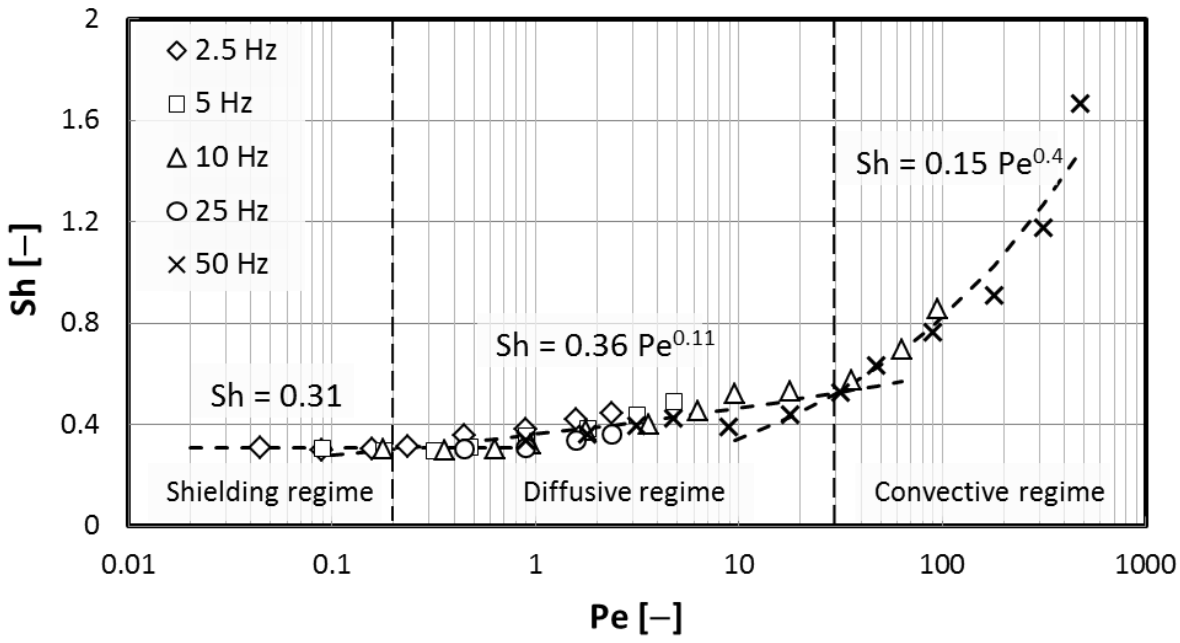

Fig. 6.9. Sherwood number versus Peclet number for all the simulations in Table 6.2.

Shielding regime ($Pe < 0.2$): the beat frequency is low and the shielding effect prevails. The mass transfer only depends on the diffusivity since the frequency of the cilia beat is very slow, but the pseudo-diffusivity is only one-third of the molecular diffusivity due to the shielding effect. The value 0.31 would probably change in three-dimensional simulations, but the general principle would remain valid. Considering Eq. (6.13) with $n = 0$,

$$D_{pcl} \propto D, \tag{6.14}$$

which confirms that the pseudo-diffusivity is proportional to the molecular diffusivity.

Diffusive regime ($0.2 < Pe < 30$): the cilia beat begins to 'open' the structure and allow higher mass transfer in the ciliated-layer. Sh increases, but shielding is still high ($Sh < 1$). Considering Eq. (6.13) with $n = 0.1$,

$$D_{pcl} \propto s^{0.2} f^{0.1} D^{0.9}, \tag{6.15}$$

which shows that diffusion is still the main mass transfer mechanics as, in Eq. (6.15), D has the highest exponent.

Convective regime ($Pe > 0.3$): the cilia beat creates significant recirculation regions that increase Sh. Considering Eq. (6.13) with $n = 0.4$,

$$D_{pcl} \propto s^{0.8} f^{0.4} D^{0.6}, \tag{6.16}$$

which indicates that the role of the frequency becomes more significant (its exponent is now 0.4). However, Eq. (6.16) also suggests that the size of the recirculation region (the exponent of s is 0.8) is even more important than the actual frequency.

6.6 Conclusions

In this chapter, we have used the Discrete Multi-Physics approach to simulate diffusive and convective mass transfer in boundary layers containing motile cilia. Fluids (mucus and PCL) and static solid (membrane) are implemented with the Smoothed Particle Hydrodynamics while flexible cilia are structured with the Mass and Spring Model.

Metachronal wave is mimicked by means of 'ghost parabola' particles and a mass transfer algorithm is introduced for modelling concentration diffusion between the mucus and the membrane through the PCL.

The aim of the present study is to quantify the effects of the ciliated layers on the PCL flow (convection) and mass transfer. Specifically, we have examined the role of the cilia beat frequency, the flexibility of the cilia and the initial diffusivity of the mucus.

Mass transfer in the ciliated-layer is hindered by the presence of cilia and the apparent diffusivity reduces to one-third of the molecular diffusivity. As the frequency of the cilia beat increases, recirculation regions appear in the velocity profile. In these regions, mass transfer increases due to convective mixing. However, the size of the convective regions seems to affect mass transfer more than the actual frequency. As a consequence of this, we suggest the possibility that the capacity of the respiratory epithelium to absorb inhaled drugs may be more strongly correlated with the flexibility of the cilia rather than the frequency of its beat. The current results could also have implications for our understanding of the mechanisms that lead to repeated infections and chronic respiratory syndrome in patients with ciliopathies. In patients with primary pulmonary ciliary dyskinesia or the more common form of acquired (secondary) ciliary dyskinesia the altered or completely suppressed function of the cilia reduces the effectiveness of the mucociliary "conveyor belt". As seen in this work, it also has important implications on the speed with which both drugs and toxic agents can reach the airway epithelium.

6.7 Notation and abbreviations

Notation

P_{TOT}	Total permeability, m s^{-1}
P_{me}	Permeability of the membrane, m s^{-1}
P_{mu}	Permeability of the mucus, m s^{-1}
P_{pcl}	Permeability of PCL, m s^{-1}
J	Drug's flux, kg m^{-2} s^{-1}
c	Mass concentration, kg m^{-3}
δ_{TOT}	Total thickness, m
δ_{me}	Thickness of the membrane, m
δ_{mu}	Thickness of the mucus, m
δ_{pcl}	Thickness of PCL, m
D	Molecular diffusivity, m^2 s^{-1}
D_{TOT}	Total diffusivity, m^2 s^{-1}
D_{me}	Diffusivity of the membrane, m^2 s^{-1}
D_{mu}	Diffusivity of the mucus, m^2 s^{-1}
D_{pcl}	Diffusivity of PCL, m^2 s^{-1}

D_B	Brownian diffusivity, $m^2\ s^{-1}$
v_p	Velocity of the parabola, $m^2\ s^{-1}$
f	Frequency, s^{-1}
k_b	Boltzmann constant, $kg\ m^2\ s^{-2}\ K^{-1}$
T	Temperature, K
μ	viscosity, Pa s
a	Diameter of the inhaled particle, m
H_{mu}	Thickness of the mucus, m
H_{me}	Thickness of the membrane, m
L_{pcl}	Length of cilium, m
l	Distance inter-cilium, m
W	Total length of the section, m
d	Distance parabola-membrane, m
s	Distance mucus-parabola, m
λ	Dimensionless ratio, (-)
σ^2	Variance, $m^2\ s^{-2}$
Sh	Sherwood number, (-)

Pe	Péclet number (-)

Abbreviations

PCL	Periciliary Layer
DMP	Discrete Multi-Physics
SPH	Smoothed Particle Hydrodynamics
MSM	Mass and Spring Model

CHAPTER 7: WALL COLLISION AND DRUG-CARRIER DETACHMENT IN DRY POWDER INHALERS: USING DEM TO DEVISE A SUB-SCALE MODEL FOR CFD CALCULATIONS

7.1 Abstract

In this study, the Discrete Element Method (DEM) is used to simulate the dispersion process of Active Pharmaceutical Ingredients (API) after a wall collision in dry powders inhaler for lung delivery. A three-dimensional model is implemented with one carrier particle and 882 drug particles. The effect of the impact velocity, angle of impact and the carrier rotation are investigated for both elastic and sticky walls. The dispersion process shows a preferential area of drug detachment located in the southern hemisphere of the carrier. The angle of impact with the highest dispersion is 90° for the velocities over 9 m s^{-1} and between 30° and 45° for lower velocities. The rotation of the carrier before the impact, on the other hand, for velocities higher than 7 m s^{-1}, plays little role on the dispersion performance. The DEM results are finally 'distilled' into a simplified analytic model that could be introduced as a sub-scale model in CFD calculations linking hydrodynamics with the detachment ratio of APIs in the inhaler.

7.2 Introduction

Dry powder inhalers (DPIs) are used for drug delivery to the respiratory tracts. The drug particles, the so-called Active Pharmaceutical Ingredient (API), need to be small enough (around 1 to 5μm) in order to reach the lungs. However, high cohesion inter-particle forces in these fine powders lead generally to the formation of agglomerates (Tong et al. 2015, Tong et al. 2016) which negatively affect the dispersion of APIs in the airflow (Reychler et al. 2007). To avoid this issue, larger particles (around 50 and 100 μm) called carrier particles are normally used; the surface of the carrier particle is coated with API particles and conveyed with the flow through the inhaler. Under normal conditions, high turbulence and contact with the wall of the device ensure the detachment of the API particles and a effective delivery to the lungs (Chan 2006). Despite the abundance of DPIs in the worldwide market, however, the percentage of APIs that actually reach the lungs is only between 20 and 40%. Various techniques for increasing the efficiency of inhalation devices, therefore, have been proposed: (i) narrower inlet sections that increase air velocity and the probability of particle-wall impact (Zhou et al. 2013) and (ii) grid insertion that concentrates turbulence in the inhaler swirl chamber (Chan 2006, Zhou et al. 2013). In addition, the formulation of the powders can also play an important role in the penetration of the particles in the airway and the presence of high ratios of porous or elongated particles has been shown to be beneficial (Chan 2006, Kaialy et al. 2012).

Other investigations have focused on the understanding of the mechanisms induced by flow and particle dynamics in inhaler chambers. Cui et al. (2014) and Sommerfeld and Schmalfuss (2016) simulated the flow dynamics in a complete inhaler system and showed that the highest velocity and turbulent kinetic energy magnitudes are located in the swirl chamber. Milenkovic

et al. (2013), Milenkovic et al. (2014) studied the particle flow dynamics in turbuhalers and focused on the location of the preferential particle deposition according to their sizes and the flow velocity. Tong et al. (2015) quantified the energy generated by the inter-particle collisions and the particle-wall impact and showed that the particle-wall collision energy is the predominant factor.

For ensuring an efficient drug delivery in the lungs, the API detachment from the carrier during the inhalation also needs to be maximised. Therefore, in recent years, micro-scale modelling of API-API and API-carrier interactions has gained interest. Cui et al. (2014) simulated one APIs-carrier agglomerate under a flow with different velocities and directions and highlighted three mechanisms of detachment: lift-off, rolling and sliding. Cui and Sommerfeld (2015) focused on the fluid dynamic forces acting on API particles with different properties such as their numbers, positions and the degree of coverage APIs-carrier. They showed that the normal and the tangential forces on the APIs varied with the API position on the carrier and that the fluid dynamics forces acting on APIs are lower with smaller drug particles. Sommerfeld and Schmalfuss (2016) studied the fluid dynamics of the flow in the vicinity a carrier particle and quantified the fluid stresses such as the velocity, the shear rate and the turbulent kinetic energy. Their findings show the importance of the fluid forces, in particular, the transverse lift forces, on the particle velocity.

However, although all these studies give important information on the fluid and the particle motion, APIs dispersion induced by wall impact remains limited to a few studies. (Tong et al. 2009, Tong et al. 2016) investigated the breakage of an APIs agglomerate (without carrier support) under different velocities, impact angles and agglomerate strengths. Using different geometries, these studies highlight the weak API-API cohesion after an impact and confirmed

the key role of the wall in term of impact energy. In the same way, (Tong et al. 2015, Yang et al. 2015), with an API-carrier model, investigated a number of parameters which play a role on the number of APIs detaching from the carrier after a wall impact. They showed, in particular, that the dispersion of APIs increases with the translational velocity and the angle of impact, and that the normal component of the impact velocity is the dominant factor. They also approximated the APIs dispersion performance with a cumulative distribution function of the impact energy and the adhesion energy. van Wachem et al. (2017), with a multi-scale approach, simulated the APIs dispersion with different adhesion forces. Their findings highlight the link between the properties of particles and the performance of the inhalers. They also demonstrate the relevance of using micro-scale results (APIs-carrier impact mechanisms) in a large macro-scale simulation (inhaler device).

The aim of this work is to fill the gap between micro- and macro-scale simulations. Micro-scale models calculate the fraction of APIs detaching from the carrier given a certain impact energy, but do not relate this information to the actual hydrodynamic conditions occurring in the inhaler. Macro-scale simulations (e.g. CFD), on the other hand, describe the hydrodynamics of the flow in the inhaler and, by means of Lagrangian particle-tracking, the trajectories of the carrier particles, but do not convert this information in a fraction of detaching APIs and, ultimately in the performance of the device.

In this work, the collision between the APIs-carrier agglomerate and the wall is modelled at the micro-scale by means of the Discrete Element Method (DEM) and the effect of impact velocity, angle of impact and angular velocity is investigated. The DEM results are then ‘distilled’ into a simplified analytic model that can be introduced as a sub-scale model in CFD calculations linking hydrodynamics with the detachment ratio of APIs in the inhaler.

7.3 Methodology

7.3.1 Modelling

In DEM, the particles move and rotate according to the Newtonian equations of motion (Tong et al. 2016)

$$m_i \frac{dv_i}{dt} = m_i \frac{d^2 r_i}{dt^2} = \sum_{i \neq j} \mathrm{F}_{i,j} + \sum \mathrm{F}_E, \tag{7.1}$$

$$I_i \frac{dw_i}{dt} = \sum_{i \neq j} \mathrm{R}_i \, \mathrm{F}_{i,j}, \tag{7.2}$$

where m_i is the mass of particle i, v_i its velocity, r_i its position, F_E the external forces, and $F_{i,j}$ the internal or inter-particle forces. I_i, w_i, and R_i, are respectively, the moment of inertia, the angular velocity and the radius of the particle i.

In this work, the internal forces $F_{i,j}$ are the contact forces and account for (i) the non-adhesive elastic contact after a collision particle-particle or particle-wall based on the Hertzian theory and (ii) the adhesive contact between 2 spherical particles based on the Bradley model.

The Hertzian model consists of a normal contact force f^n and a tangential contact force f^t (Zhang and Makse 2005)

$$f^n = \sqrt{\delta}\sqrt{R_{eff}}(k_n\delta - m_{eff}\gamma_n v_n), \tag{7.3}$$

$$f^t = -\sqrt{\delta}\sqrt{R_{eff}}(k_t\xi + m_{eff}\gamma_t v_t), \tag{7.4}$$

where $R_{eff} = R_iR_j/(R_i+R_j)$, is the effective radius of the colliding particles i and j with radius R_i *and* R_j, k_n and k_t are the normal and tangential stiffness of the contact, δ and ξ the overlap and the displacement between the particles in, respectively, the normal and the tangential direction, γ_n and γ_t the normal and tangential damping coefficients and $m_{eff} = m_im_j/(m_i+m_j)$ the effective mass of the colliding particles with mass m_i and m_j. The concepts of displacement ξ and, in particular, of overlap δ are abstract ideas that allow the DEM to calculate the tangential and normal forces occurring during collision. In reality, two colliding particles deform rather than overlap, but the idea is conceptually practical and is going to be used also in the discussion section.

By considering elastic materials, k_n and k_t can be defined as (Brilliantov et al. 1996, Zhang and Makse 2005)

$$k_n = \frac{2E_{i,j}}{(1+\upsilon_{i,j})(1-\upsilon_{i,j})}, \tag{7.5}$$

$$k_t = \frac{4E_{i,j}}{(2-\upsilon_{i,j})(1+\upsilon_{i,j})}, \tag{7.6}$$

with $E_{i,j}$ and $v_{i,j}$ are, respectively, Young's modulus and Poisson's ratio of particles i and j.

The adhesive contact between 2 spherical particles is modelled after Bradley (Bradley 1932)

$$\begin{cases} F_B(z) = F_c, & \text{for } z \le z_0 \\ F_B(z) = \dfrac{R_i R_j}{R_i + R_j} \dfrac{16\psi\pi}{3} \left[\dfrac{1}{4} \left(\dfrac{z}{z_0} \right)^{-8} - \left(\dfrac{z}{z_0} \right)^{-2} \right], & \text{for } z > z_0 \end{cases} \quad (7.7)$$

where F_B *is* the surface force between the particles i and j at a distance z, F_c is the maximum surface force when particles i and j are in contact ($z = z_0$), 2ψ the total surface energy of both surfaces per unit area and z_0 the equilibrium separation of the particles i and j. In our simulations, z_0 is equal to 4 10^{-10} m (Popov 2010), ψ is deduced from Eq. (7.7) for $z = z_0$, and F_c is equal to 2.58 10^{-7}N (Cui et al. 2014).

7.3.2 Geometry and model setup

A three-dimensional model is implemented and consists of one carrier particle with a diameter of 100 µm and 882 of mono-sized API particles with a diameter of 5 µm agglomerated around the carrier (Fig. 7.1).

In API-carrier simulations, a degree of coverage is often used to define the number of APIs in contact with the carrier (Cui et al. 2014). In the case of a mono-layer with mono-sized particles, the degree of coverage α is defined as the cross-section area of all API particles divided by the area of the sphere 'API + carrier' (Cui et al. 2014)

$$\alpha = \frac{n_{API} \dfrac{\pi}{4} d_{API}^2}{\pi \left(d_c + d_{API} \right)^2}, \quad (7.8)$$

with n_{API} the number of API particles, d_{API} and d_c the diameter of one API particle and the carrier particle, respectively. In our simulations, we use a degree of coverage of 50 % at $t = 0$ (Cui et al. 2014), which correspond to 882 API particles attached on the surface of the carrier.

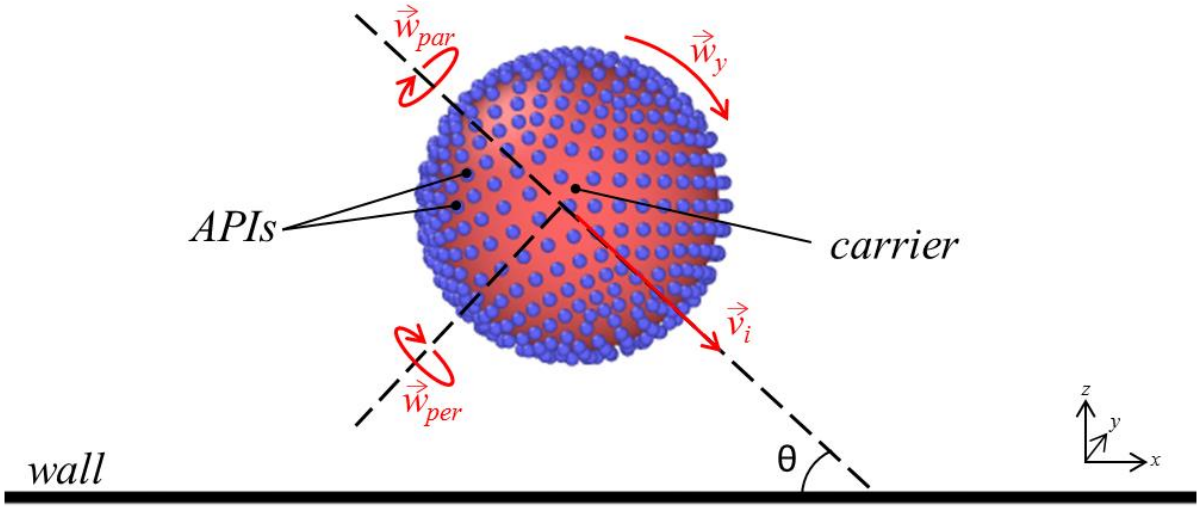

Fig. 7.1. Illustration of the API-carrier agglomerate.

The APIs and the carrier are considered elastic and their material properties are summarised in Table 7.1 (Cui et al. 2014). Additionally, the wall property effect is also investigated and, by modifying the damping coefficients (γ_n and γ_t in Eqs. (7.3) and (7.4)), different types of wall can be implemented (Table 7.1). Two walls are used: an '*elastic*' wall where both APIs and carrier have the same damping coefficients and can rebound after impacting the wall and a '*sticky*' wall where the APIs remain in attached to the wall after impact.

Table 7.1. Model parameters used in the simulations.

Model parameter	**Value**
Diameter of the carrier particle, d_c	100 μm
Diameter of one API particle, d_{API}	5 μm
Mass of the carrier particle, m_c	$1.31\ 10^{-9}$ kg
Mass of the API particle, m_{API}	$8.44\ 10^{-14}$ kg
Young's modulus of the carrier particle, E_c	63 GPa
Young's modulus of the API particle, E_{API}	2.15 GPa
Poisson's ratio of the carrier particle, ν_c	0.24
Poisson's ratio of the API particle, ν_{API}	0.3
Normal damping coefficient of carrier γ_{nc}	(1) 0.3 (2) 0.3
Tangential damping coefficient of carrier γ_{tc}	(1) 0.15 (2) 0.15
Normal damping coefficient of API γ_{nAPI}	(1) 0.3 (2) $6\ 10^{14}$
Tangential damping coefficient of API γ_{tAPI}	(1) 0.15 (2) $6\ 10^{20}$
Time step	10^{-9} s
Total time of each simulation*	10^{-2}s (simulation), 90s (computation)
(1) '*elastic*' wall, (2) '*sticky*' wall	
*1 core/node, 1 node used) 64-bit 1.9 GHz Intel Core i3-40300	

7.3.3 Simulation parameters

In this study, four variables are investigated: the translational and angular velocity v and w of the API-carrier, the axes of rotation, and the impact angle θ.

In our simulations, we vary the translational velocity from 1 m s^{-1} to 20 m s^{-1} (every 1 m s^{-1}) and we select 8 angles of impact between 5° to 90°. Moreover, three axes of rotation are chosen for the carrier: a rotation around the axis y (w_y in Fig. 7.1); a rotation around the axis perpendicular to the translational velocity $\vec{v}$ (w_{per} in Fig. 7.1); and a rotation around the axis parallel to the translational velocity $\vec{v}$ (w_{par} in Fig. 7.1). For these three axes of rotation, a variation of the angular velocity magnitude of $2\ 10^5$ rad s^{-1} is used between $-1\ 10^5$ rad s^{-1} and $1\ 10^5$ rad s^{-1}.

The implementation of these series of variations including the '*elastic*' and the '*sticky*' wall conditions brings it to a total number of simulations of 9600 simulations.

7.4 Results

In the following sections, the dispersion ratio η, defined as the number of detached APIs (after impact) over the total number of APIs, is calculated for each simulation. For literature comparison, we use the same API and carrier material properties of (Yang et al. 2015): the APIs and carrier are made of the same material with a density of 2650 kg m^{-3}, Young's modulus of 24 GPa, Poisson's ratio of 0.3 and an adhesion force of 2.99 10^{-9} N.

A snapshot of a typical simulation is shown in Fig. 7.2. During the impact, the particles located in the southern hemisphere tend to detach more easily than those located in the northern hemisphere. The reason of this behaviour, which also has been reported, but not explained, elsewhere (Yang et al. 2015), is discussed in Section 7.5.

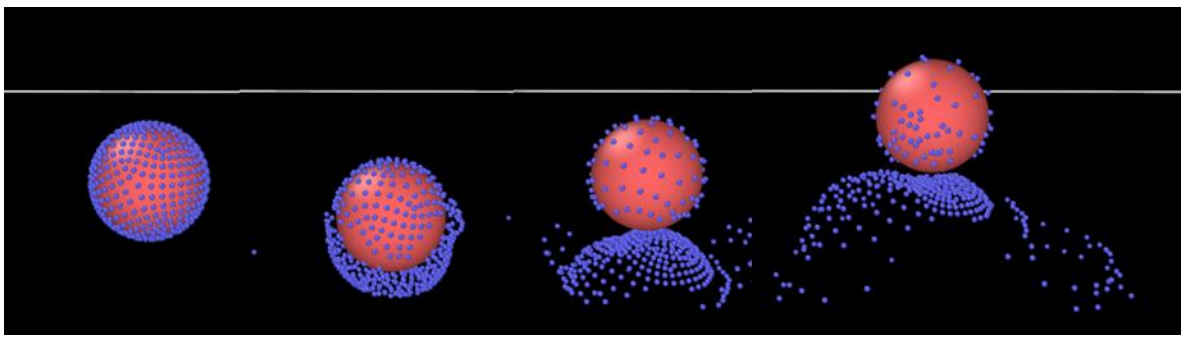

Fig. 7.2. Snapshots of the impact API-carrier with the wall at different times for $v = 0.1$ m s^{-1}, $\theta = 45°$, $F_c = 2.99\ 10^{-9}$ N and $\alpha = 15\%$.

In the following section, we use the properties presented in Table 7.1.

7.4.1 Effect of translational velocity

The effect of the impact angle and translational velocity on the dispersion ratio is shown in Fig. 7.3. In these simulations, the angular velocity is set to zero. For velocities above 9 m s^{-1}, the dispersion ratio is maximal at 90° (Yang et al. 2015), while for lower velocities is located between 30° and 45°. This behaviour has also been observed by (Tong et al. 2015), but not explained. More details on this are given in section 7.5.

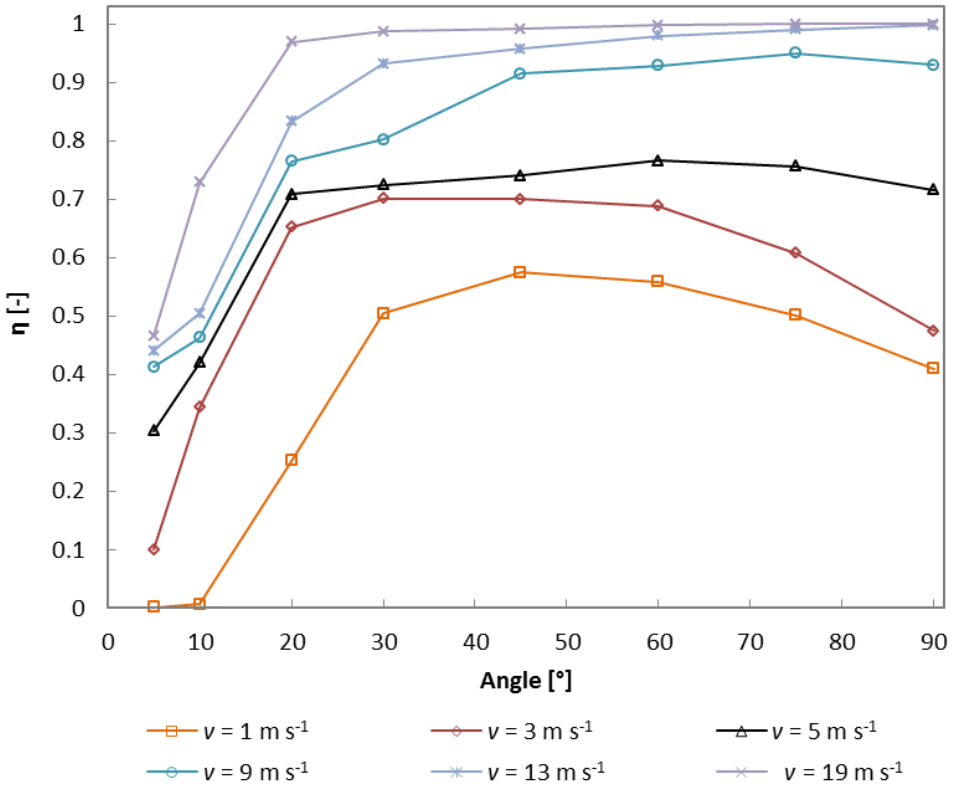

Fig. 7.3. Effects of the impact angle and the translational velocity on the dispersion ratio for the case of '*elastic*' wall and $w = 0$.

7.4.2 Effect of rotational velocity

In this section, the effect of the carrier rotation is investigated. In order to highlight the specific effect of each axis of rotation, we implement separately the angular velocities w_y, w_{par} and w_{per} as explained in section 7.3.3. The DEM results show that, above $v = 7$ m s^{-1}, the dispersion is not significantly affected by the angular velocity (in any direction). Below 7 m s^{-1}, differences are only observed for angular velocities in the y-direction. Fig. 7.4 shows how the initial angular velocity of the carrier affects the dispersion at $v = 5$ m s^{-1}. The fact that only w_y affects the dispersion depends on the fact that, given our coordinate system (Fig. 7.1), during the collision the tangential forces transfer part of the linear momentum in the x-direction into angular momentum in the y-direction. This does not occur with w_{par} and w_{per} that remain approximately constant during the collision. Therefore only w_y causes an actual acceleration of the carrier that can affect the detachment. Fig. 7.5 provides an example of how v_x and w_y are linked. If w_y is positive (Fig. 7.5a), v_x increases during the impact. If w_y is negative, v_x decreases during the impact and, in the case of (Fig. 7.5b), the carrier even bounces backwards after the collision (a similar effect is known as 'sidespin' in cue sports). This circumstance plays a role in the detachment, but it is not always easy to anticipate its effect on the detachment without the actual DEM simulation as discussed in section 7.5.

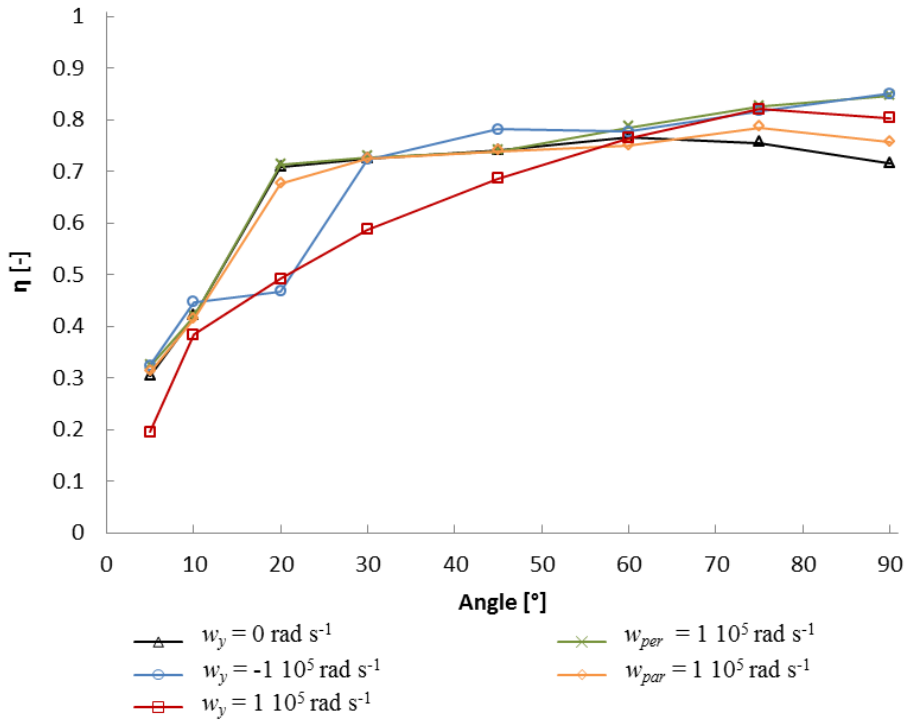

Fig. 7.4. Effects of the impact angle and the angular velocity magnitude on the dispersion ratio for the case of '*elastic*' wall and v = 5 m s^{-1}.

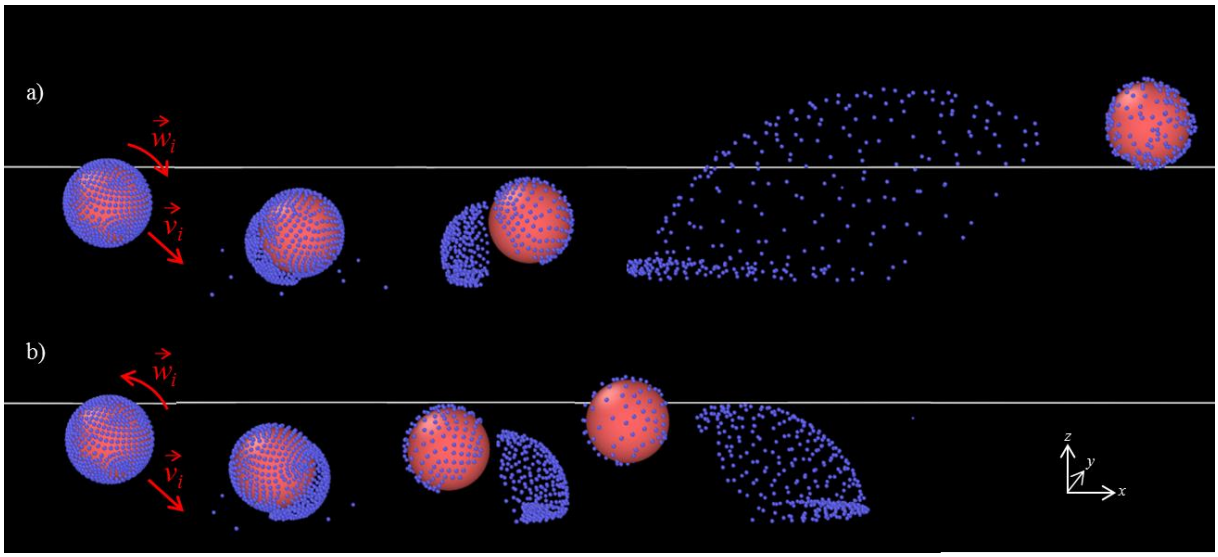

Fig. 7.5. Snapshots of the impact API-carrier on '*elastic*' wall at different times for v=1 m s^{-1}, θ=45° and an initial rotation in the y-direction (a) w=1 10^5 rad s^{-1} and (b) w=-1 10^5 rad s^{-1}.

7.4.3 Effect of wall properties

The rebound of the API-carrier agglomerate after impact with two different walls is shown in Fig. 7.6. The detachment process is similar in both cases with a preferential detachment located in the southern hemisphere. A difference is observed on the motion of the detached APIs after impact. In the case of '*elastic*' wall (Fig. 7.6a), detached APIs maintain a certain velocity and rebound with the carrier. In the case of '*sticky' wall* (Fig. 7.6b), after detachment, the APIs remain attached on the wall (Fig. 7.6b).

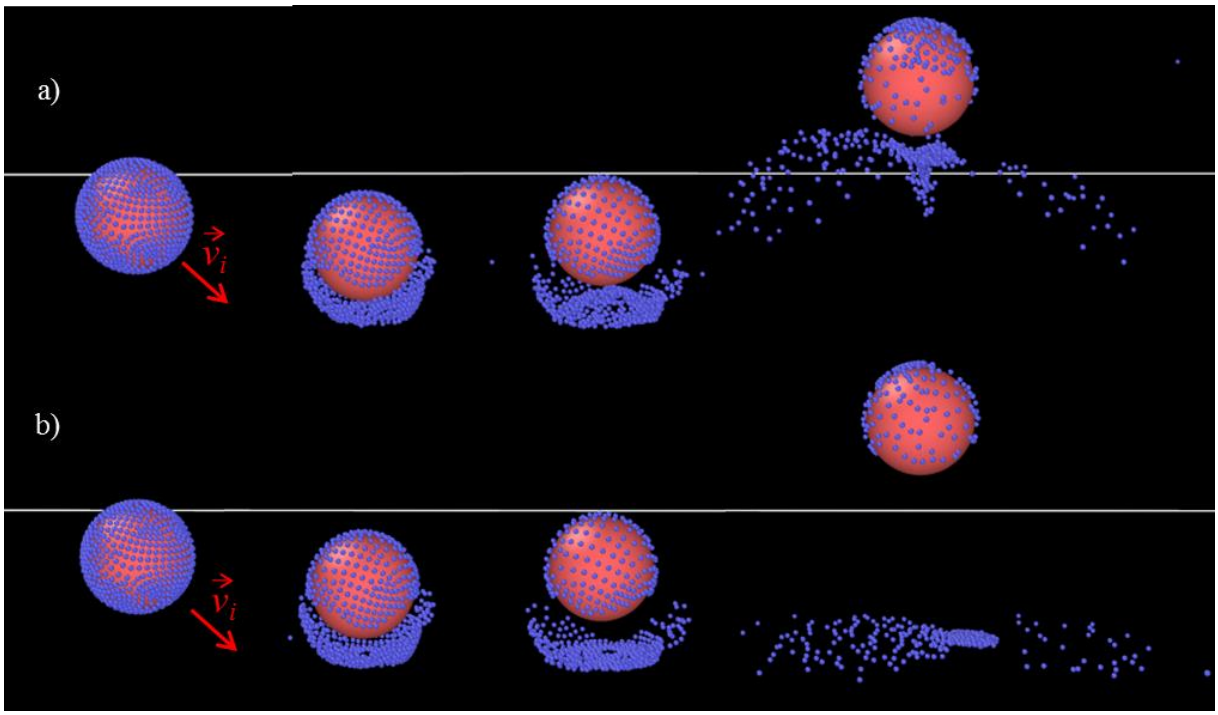

Fig. 7.6. Snapshots of the impact API-carrier at different times for $v = 1$ m s^{-1}, $\theta = 45°$ for (a) '*elastic*' wall (a) versus '*sticky*' wall (b).

Similarly, Fig. 7.7 indicates that the detachment ratio is not particularly affected by the nature of the wall and the only significant difference occurs at $v = 19$ m s^{-1} and for angles below 20°.

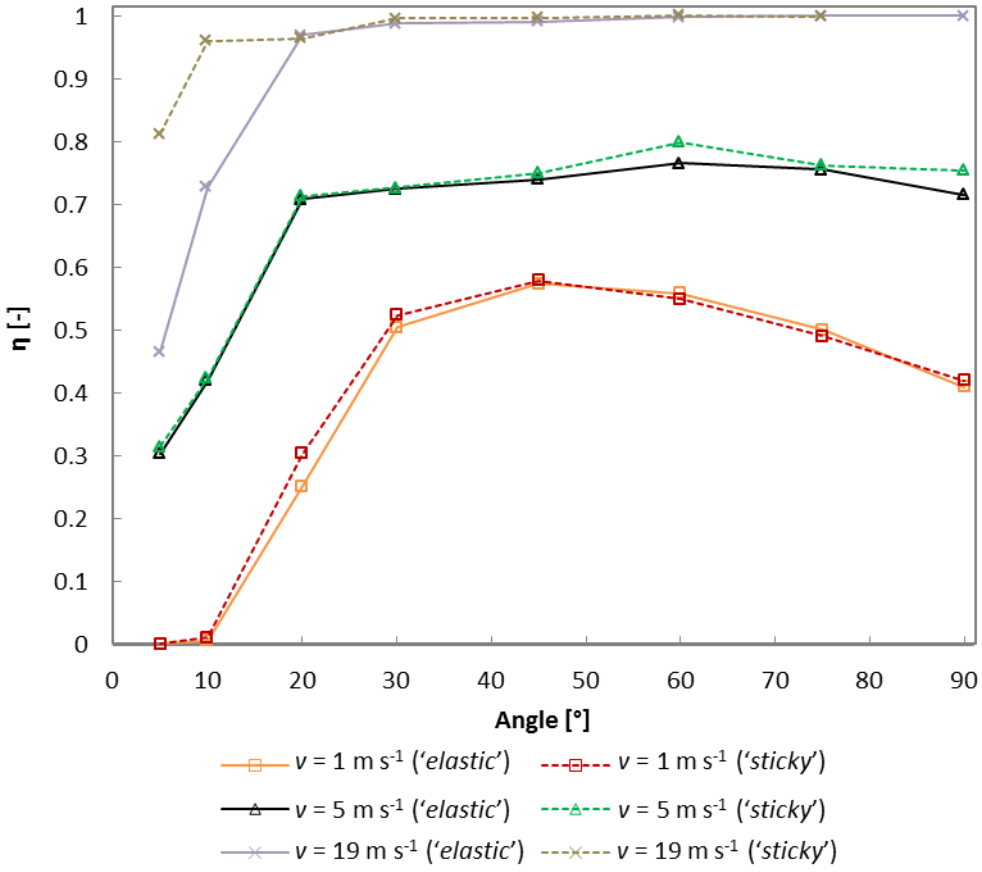

Fig. 7.7. Effects of the impact angle and the translational velocity on the dispersion ratio in the case of '*elastic*' wall and '*sticky*' wall.

When the carrier moves with very small angles close to the wall, even if the impact energy is not enough to detach the APIs, the '*sticky*' wall can capture the small particles trapped between the carrier and the wall like a sort of flypaper. This occurs, in particular, at higher velocities when the overlap δ is larger and, therefore, there are more APIs caught in between the carrier and the wall.

7.5 Discussion

7.5.1 Preliminary considerations

7.5.1.1 Collision between carrier and wall

Initially, we look at the collision of the carrier with the wall and we can simplify the collision process in three main steps (Fig. 7.8). When the particle hits the wall, its angular velocity is w and its translational velocity is v with its perpendicular and parallel (to the wall) components respectively

$$v_{\perp} = v\sin\theta, \tag{7.9}$$

$$v_{//} = v\cos\theta, \tag{7.10}$$

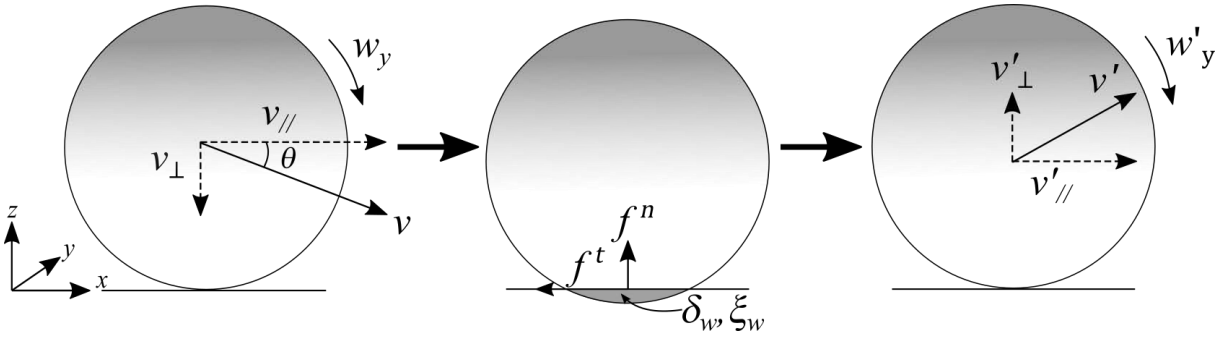

Fig. 7.8. Schematic representation of the carrier collision.

During the collision, the DEM simulation calculates the overlap δ_w and the displacement ξ_w between the wall and the carrier. The overlap and the displacement do not actually occur in a real collision, but, as mentioned, are abstract concepts used by the DEM solver to calculate the contact normal and tangential forces f^n and f^t (Eqs. (7.3) and (7.4)).

The collision is fully elastic and there is not dissipation. However, the value of v changes before and after the collision. Due to f^t, in fact, part of the tangential kinetic energy is transformed in rotational kinetic energy. The parallel velocity $v_{//}$ does not remain constant

(becomes $v'_{//}$) and part of the linear kinetic energy lost (or gained) goes into the angular velocity w (that becomes w'). In theory, if the collision is elastic, this should affect only the parallel velocity. The situation, however, is considerably complicated by the presence of a layer of APIs between the carrier and the wall and, usually, there is also a (smaller) change of perpendicular velocity $v_{\perp}$ that becomes $v'_{\perp}$.

7.5.1.2 API's Escape velocity

Initially, the APIs move with the carrier. At equilibrium, the overlap δ between the carrier and the API can be calculated from the balance of forces

$$f^n\delta - F_B\delta = 0. \tag{7.11}$$

In the case of Hertzian contact, Eq. (7.11) gives

$$\delta = \left(\frac{F_B}{\sqrt{R_{eff}}k_n} \right)^{\frac{2}{3}}. \tag{7.12}$$

After the carrier hits the wall, the relative velocity between the two particles suddenly changes. We can distinguish two cases (Fig. 7.9). If the relative velocity of the API is above a certain critical velocity (i.e. the escape velocity v_e), the kinetic energy overcomes the work done by the adhesion force and the particle detaches from the carrier. If the velocity is below v_e, the overlap between the two particles diminishes during the contact, but, after the carrier wall collision, it returns to its initial value while the relative velocity ($\Delta v = v_{API} - v_{carrier}$) returns to zero (Fig. 7.9). Only particles whose relative velocity is higher than v_e detach from the particle. In principle, there is not a simple way to determine the relative velocity without

the DEM simulation. In the following sections, however, we discuss two typical detachment scenarios (or modes) and, based on these, a simplified model, which can estimate the dispersion ratio without the need of carrying out a DEM simulation, is proposed.

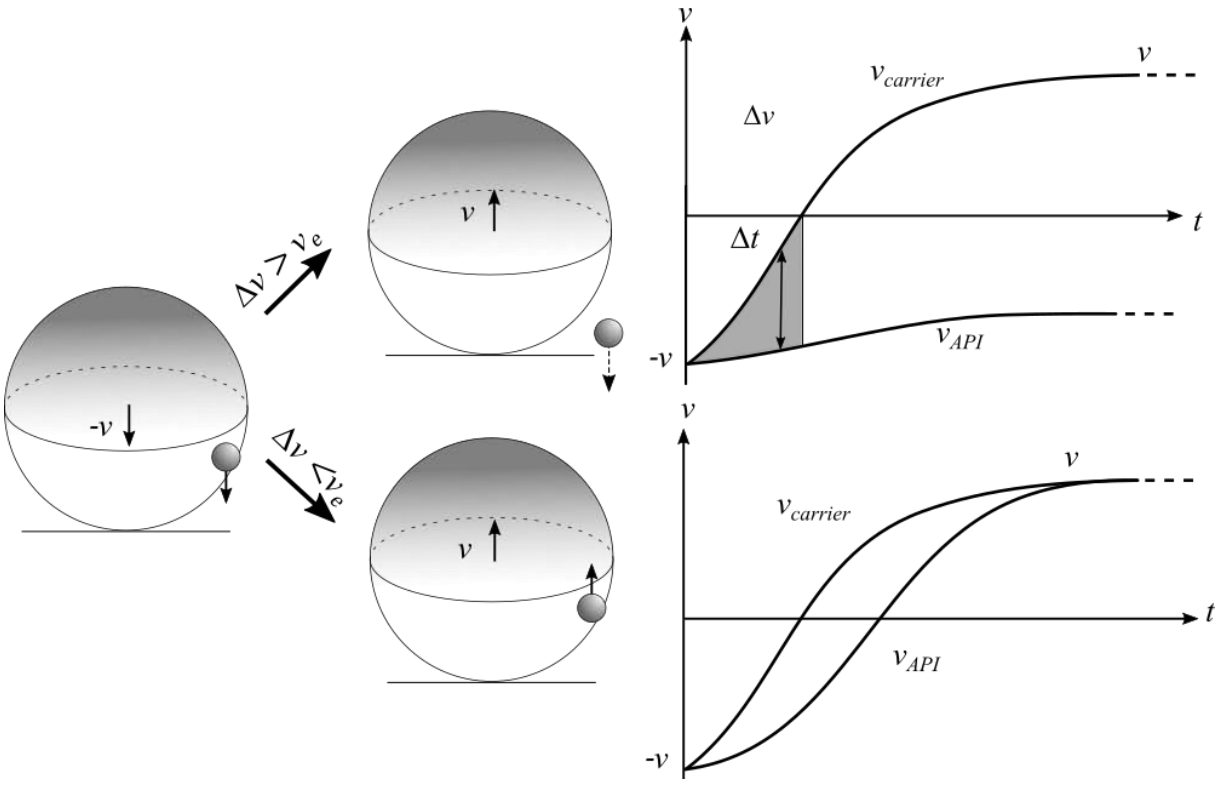

Fig. 7.9. Relative velocity between API and carrier and escape velocity.

7.5.2 Detachment modes

Initially, we neglect the angular velocity. This means that no energy is transferred from the linear to the rotational velocity and, since the collision is elastic, $v = v'$, $v_{//} = v'_{//}$, and $v_{\perp} = v'_{\perp}$ in Fig. 7.8. The carrier and the APIs, therefore, have, at all times, the same parallel velocity $v_{//}$ and the detachment only depends on the perpendicular velocity. In this case, the dynamics differs if the API is located at the northern or the southern hemisphere of the carrier. We propose two simplified models of detachment one for the northern hemisphere and another for the southern hemisphere.

7.5.2.1 Southern hemisphere detachment

The collision with the wall reduces abruptly the perpendicular component of the carrier velocity. As a consequence, the relative velocity of an API located on the southern hemisphere increases as shown in Fig. 7.10. As mentioned, since the collision is elastic and, for the moment, we neglect the angular velocity, the parallel velocity of both particles is not affected by the collision and, therefore, the relative velocity Δv has only a perpendicular component (Fig. 7.10).

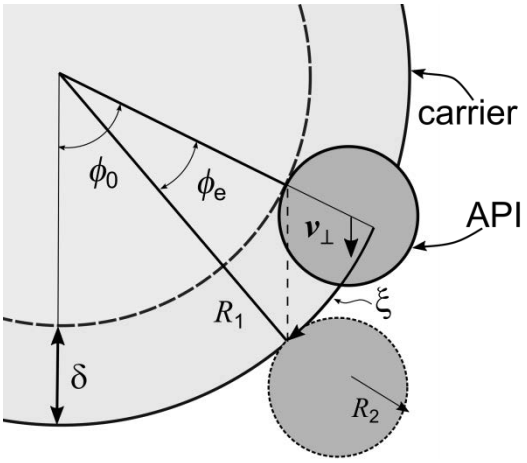

Fig. 7.10. The Southern hemisphere detachment (overlap oversized for explanation purposes).

The kinetic energy of the API is

$$E_K(t) = \frac{1}{2} m \left[\Delta v_\perp(t)\right]^2 . \tag{7.13}$$

The relative velocity $\Delta v_\perp$, however, changes with time. Eq. (7.13) can be simplified by considering an average relative velocity $<\Delta v_\perp>$ during the detachment process. The DEM simulations show that the detachment occurs during the first part of the collision (Δt in Fig. 7.9, the time required for the carrier to stop before the rebound) As a first approximation, we

can use $<\Delta v_{\perp}> = \frac{1}{2} v_{\perp}$ (averaging over the 'almost triangular' grey area in Fig. 7.9) and, accounting for Eq. (7.9), an estimate of the kinetic energy of the API during detachment, therefore, is

$$E_K \approx \frac{1}{8} m v^2 \sin^2 \theta. \tag{7.14}$$

During the detachment, the work done by the adhesion force can be calculated as

$$E_B = \int_{-\delta}^{\infty} F_B(z) dz, \tag{7.15}$$

where F_B is given by Eq. (7.7). An estimate of E_B, which does not require the calculation of the integral is

$$E_B \approx F_C(z_0 + \delta + \frac{z_{cut-off}}{2}), \tag{7.16}$$

where $z_{cut-off}$ is a cut-off distance, after which adhesion force is negligible and is calculated to approximate Eq. (7.16) with Eq. (7.15); here $z_{cut-off} = 10^{-9}$ m.

The work done by f^n can be calculated by

$$E_n = \sqrt{R_{eff}} k_n \int_0^{\delta} z^{\frac{3}{2}} dz = \frac{2}{5} \sqrt{R_{eff}} k_n \delta^{\frac{5}{2}}, \tag{7.17}$$

where the displacement δ is calculated from Eq. (7.12).

The tangential force acting on the particle is $\min(f^t, \mu f^n)$, where μ is the static friction coefficient and f^t is given by Eq. (7.4). To simplify our calculations, we estimate the work

done by the tangential force only on the basis of μf^n since, only when the tangential force reaches this value, the API begins to move relatively to the carrier

$$E_t \approx \mu\sqrt{R_{eff}}k_n\delta^{\frac{3}{2}}\xi. \tag{7.18}$$

The tangential displacement can be estimated as Fig. 7.10

$$\xi \approx R_1\phi_e, \tag{7.19}$$

where R_1 is the radius of the carrier and ϕ_e the escape angle (Fig. 7.10). Geometric considerations bring to

$$(R_1-\delta)\sin\phi_0 = R_1\sin(\phi_0-\phi_e), \tag{7.20}$$

and

$$\phi_e = \phi_0 - \sin^{-1}\left(\frac{R_1-\delta}{R_1}\sin\phi_0\right), \tag{7.21}$$

where ϕ_0 is the angle of the initial position of the API on the carrier surface. Since $R_1>>\delta$, Eq. (7.21) can be expanded in Taylor series as

$$\phi_e = \frac{\delta}{R_1}\tan\phi_0 + O(\delta^2), \tag{7.22}$$

and Eq. (7.18) becomes

$$E_t \approx \mu\sqrt{R_{eff}}k_n\delta^{\frac{5}{2}}\tan\phi_0, \tag{7.23}$$

By writing the energy balance of the API, we can determine that detachment is only possible if

$$E_k \geq E_B - E_n + E_t. \tag{7.24}$$

The symbol '≥' becomes '=' when the API's velocity is exactly the escape velocity (i.e. $v = v_e$). By combining together Eqs. (7.15), (7.16), (7.23) and (7.24), we can estimate the escape velocity as

$$v_e \approx \sqrt{\frac{F_c(\delta + z_{cut-off}) - \frac{2}{5}\sqrt{R_{eff}}k_n\delta^{\frac{5}{2}} + \mu\sqrt{R_{eff}}k_n\delta^{\frac{5}{2}}\tan\phi_0}{\frac{1}{8}m\sin^2\theta}}, \tag{7.25}$$

Eq. (7.25) tells us that if the initial velocity of the API particle is higher than v_e, the particle detaches otherwise it remains on the carrier. However, the detachment velocity is not everywhere the same. Since Eq. (7.25) depends on $\tan\phi_0$, v_e is minimal at the south pole and maximal at the equator of the carrier. By rearranging Eq.-(7.25), we can determine the critical angle ϕ_0, below which, given an initial velocity v, detachment occurs

$$\phi_0 \approx \tan^{-1}\left(\frac{\frac{1}{8}mv^2\sin^2\theta - F_c(\delta + z_{cut-off}) + \frac{2}{5}\sqrt{R_{eff}}k_n\delta^{\frac{5}{2}}}{\mu\sqrt{R_{eff}}k_n\delta^{\frac{5}{2}}}\right), \tag{7.26}$$

Assuming the initial particle API distribution is uniform on the carrier surface (Fig. 7.11), from ϕ_0, we can calculate the dispersion ratio as

$$\eta_{SOUTH} = \frac{\text{Detachment Area}}{\text{Total Area}} = \begin{cases} \frac{1-\cos\phi_0}{2} & \text{if } \phi_0 > 0 \\ 0 & \text{if } \phi_0 \le 0 \end{cases} \tag{7.27}$$

The maximum dispersion ratio occurs when $\phi_0 = \pi/2$ and the APIs on whole southern hemisphere detach.

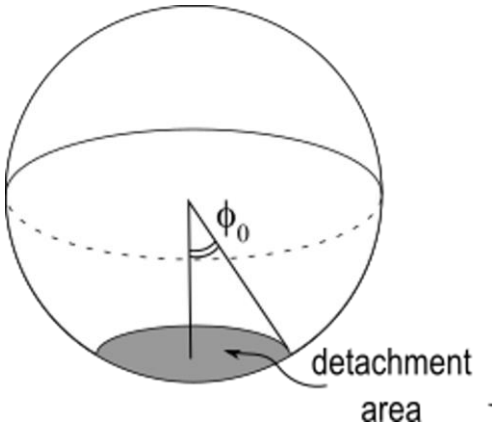

Fig. 7.11. Detachment area in the southern hemisphere.

7.5.2.2 Northern hemisphere detachment

The same logic, however, does not apply to the northern hemisphere (Fig. 7.12).

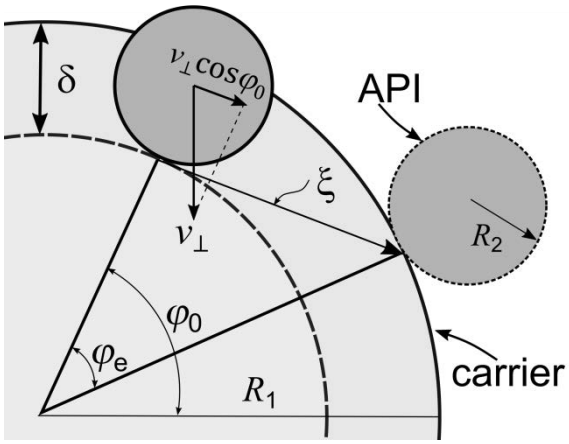

Fig. 7.12. The Northern hemisphere detachment.

In this case, the API cannot move in the perpendicular direction, but only in the direction tangential to the carrier surface. This means that the relative velocity is $\Delta v = v_{\perp} \cos\varphi_0 = v \cos\varphi_0 \sin\theta$. The displacement ξ, on the other hand, can be calculated by

$$\xi = \sqrt{R_1^2 - (R_1 - \delta)^2} \approx \sqrt{2R_1\delta}. \tag{7.28}$$

The energy balance, in this case, is obtained by

$$\frac{1}{2}mv^2 \cos^2\varphi_0 \sin^2\theta = F_c(\delta + z_{cut-off}) - \frac{2}{5}\sqrt{R_{eff}}k_n\delta^{\frac{5}{2}} + \mu\sqrt{R_{eff}}k_n\delta^{\frac{3}{2}}\sqrt{2R_1\delta}. \tag{7.29}$$

The critical angle φ_0 below, which detachment occurs, now satisfies the relation

$$\cos\varphi_0 = \sqrt{\frac{F_c(\delta + z_{cut-off}) - \frac{2}{5}\sqrt{R_{eff}}k_n\delta^{\frac{5}{2}} + \mu\sqrt{R_{eff}}k_n\delta^{\frac{3}{2}}\sqrt{2R_1\delta}}{\frac{1}{2}mv^2\sin^2\theta}}. \tag{7.30}$$

From $\cos\varphi_0$, we can calculate the dispersion ratio in the northern hemisphere as

$$\eta_{NORTH} = \frac{1 - \cos\varphi_0}{2}. \tag{7.31}$$

Finally, the overall dispersion ratio can be calculated by

$$\eta = \eta_{NORTH} + \eta_{SOUTH} \tag{7.32}$$

The simple model in Eq. (7.32) is based on several simplifications and approximations and gives a crude estimate of the actual dispersion ratio. Fig. 7.13 shows the comparison between

DEM results and the simple model. The simple model is more accurate for velocities higher than 7 m s^{-1}. The 'composite' look of some of the profiles generated by the simple model in Fig. 7.13 depends on the fact that Eq. (7.32) is the result of the two components η_{NORTH} and η_{SOUTH}.

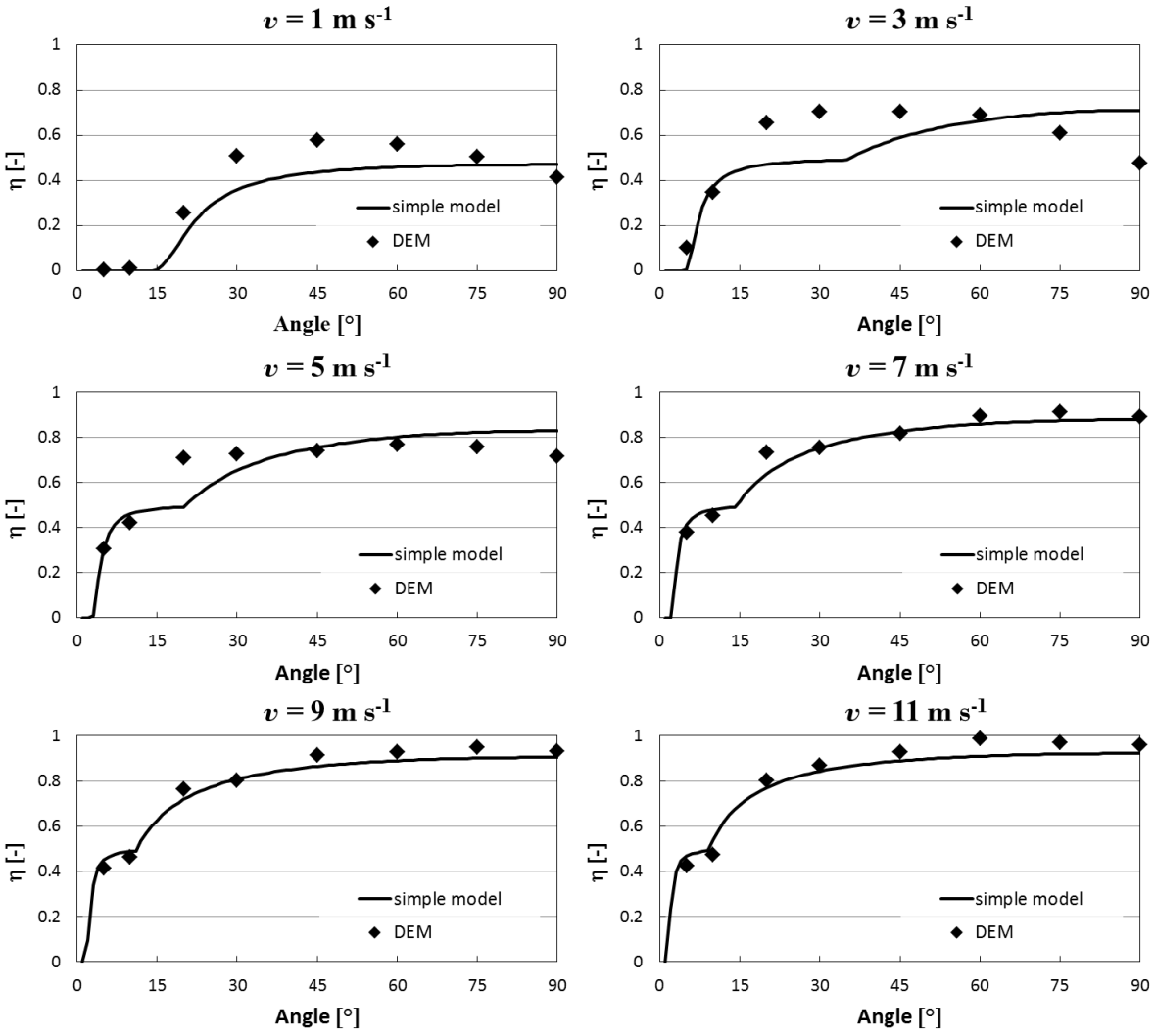

Fig. 7.13. Comparison between the simple analytic model and the DEM results.

Fig. 7.14 exemplifies this point. The maximum possible value of both η_{NORTH} and η_{SOUTH} is 0.5 since each of them only refers to an hemisphere. The final dispersion ratio η is the sum of η_{NORTH} and η_{SOUTH}.

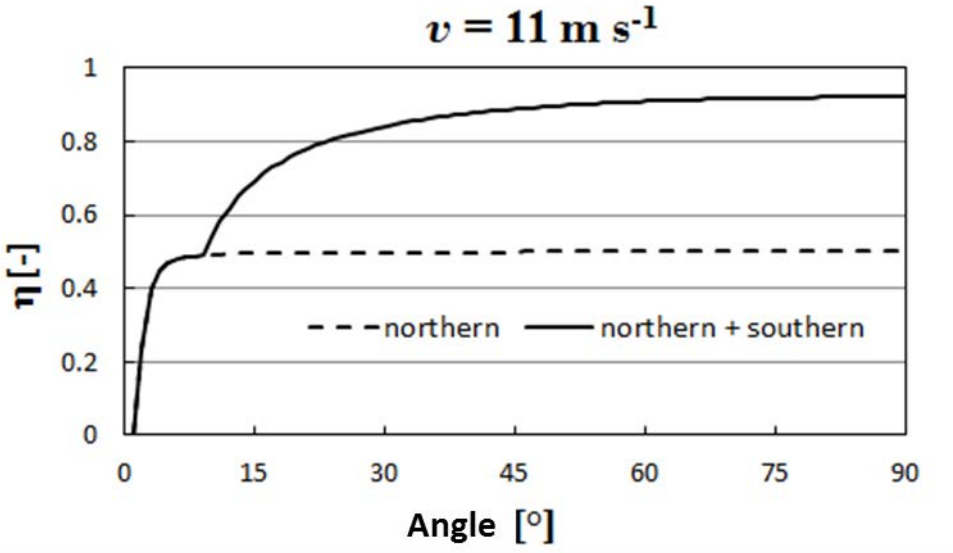

Fig. 7.14. η_{NORTH} and η_{SOUTH} components of the total dispersion ratio η.

7.5.3 Rotating particle

The simplified model derived in the previous section does not account for the rotation of the carrier. This is not a problem for higher impact velocities, since above $v = 7$ m s^{-1}, the DEM results show that the initial angular rotation does not significantly affect the results. At lower velocities, however, the effect of the angular velocity, and in particular w_y, can be perceived even if initially $w_y = 0$. This happens because the carrier starts rotating during the collision as an effect of the tangential force f^t. The maxima (Fig. 7.13) at $v = 1$ m s^{-1} and $v = 3$ m s^{-1}, for instance, depend on the change of parallel velocity $v_{//} \rightarrow v'_{//}$ (Fig. 7.8), which, in turn, depends on the change of angular velocity from $w_y \rightarrow w'_y$ as explained in Section 7.4.2.

Fig. 7.15 shows, for $v = 5$ m s^{-1} and different initial angular velocities, the absolute value of the variation of v_x during the collision. Since in this case v_x changes, the API particles (besides accelerating in the z-direction as explained in Sections 7.5.2.1 and 7.5.2.2) also accelerate in the x-direction. The magnitude of the acceleration can be expressed as

$$a_x = \frac{|\Delta v_x|}{\Delta t}. \tag{7.33}$$

where Δt is the duration of the collision. Δt changes for each θ, but if we compare $|\Delta v_x|$ at the same θ, we can notice a correspondence between Fig. 7.15 and Fig. 7.4: the case among w_y = 0, w_y = 10^5 rad s^{-1} and w_y = -10^5 rad s^{-1}, that has the highest $|\Delta v_x|$ has also the highest dispersion and, vice versa, the case that has the lowest $|\Delta v_x|$ has also the lowest dispersion.

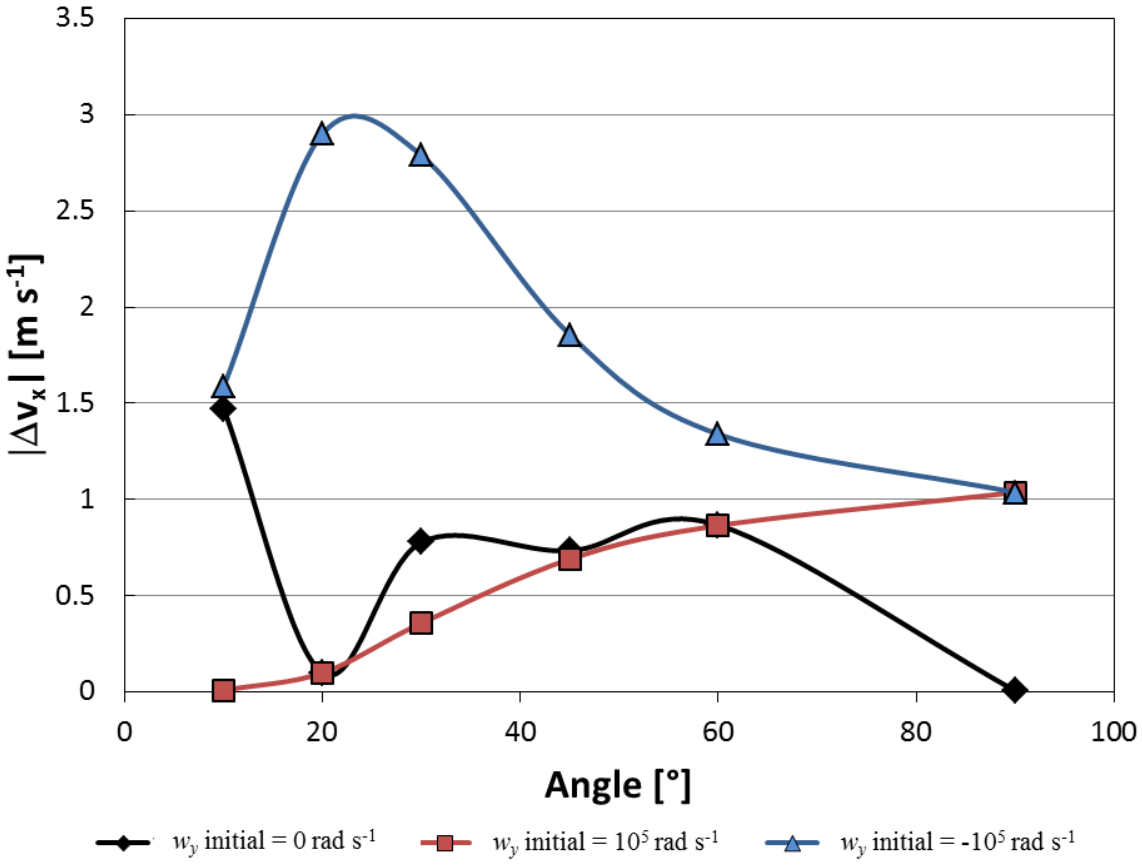

Fig. 7.15. Absolute value of the change of v_x during collision for different initial angular velocities (v = 5 m s^{-1}).

The only exception is $\theta = 20°$ that seems to behave differently both in terms of dispersion and $|\Delta v_x|$. Looking at the DEM simulation and data, we could not understand the reasons that make this specific case different from the others.

7.6 Conclusions

In this study, we used the DEM to simulate the collision of a drug-carrier with the walls of a dry powder inhaler device and the consequent detachment of the APIs. The objective is to evaluate the influence of the impact velocity, angle and angular velocity of the carrier.

Based on the DEM data, we propose a simplified analytic model, which provides a good approximation of the DEM results at high impact velocities (v > 7 m s^{-1}). The simplified model does not account for the change of angular velocity during the impact, and the data show that, above 7 m s^{-1}, the angular velocity does not particularly affect the dispersion.

The aim of the simplified model is twofold. First, it helps to highlight the main physical mechanisms behind the detachment of the APIs. In particular, we identified two modes of detachment, which we called, respectively, the northern hemisphere detachment mode and the southern hemisphere detachment mode. Secondly, the simplified model can be used as a sub-scale model in CFD studies. These studies calculate the hydrodynamics and, by means of Lagrangian particle-tracking, the trajectories of the carrier particles in the inhaler. Coupling particle-tracking with our simplified model will allow new CFD models to also predict the actual number of APIs released and, therefore, the actual efficiency of dry powder inhalers.

7.7 Notation and abbreviations

Notation

m_i	Mass of particle *i*, kg
v_i	Velocity, m s^{-1}
r_i	Position, m
w_i	Angular velocity, rad s^{-1}
θ	Impact angle, rad
R_i	Radius, m
R_{eff}	Effective Radius, m
I_i	Moment of inertia, kg m^2
F_E	External forces, N
$F_{i,j}$	Internal or inter-particle forces, N
F_B	Surface force, N
z	Distance, m
Ψ	Total energy per unit area, J m^{-2}
z_0	Equilibrium separation, m
F_c	Maximum surface force, N

f^n	Normal contact force f^n, N
f^t	Tangential contact force, N
k	Stiffness constant, (-)
δ	Overlap between 2 particles at normal direction, m
ξ	Displacement between 2 particles at tangential direction, m
δ_w	Overlap between carrier and wall, m
ξ_w	Displacement between carrier and wall, m
γ	damping coefficient, (-)
$E_{i,j}$	Young's modulus, Pa
$v_{i,j}$	Poisson's ratio, (-)
m_{eff}	Effective mass of 2 colliding particles, m
α	Degree of coverage, %
d	Diameter of a particle, m
η	Dispersion ratio, (-)
n	Number of particles, (-)
E_k	Kinetic energy, J
Φ	Angle, rad

μ	Static friction coefficient, (-)
φ	Angle, rad
Δt	Duration of collision, s
a	Acceleration, $m^2\ s^{-1}$

Abbreviations

DEM	Discrete Element Method
CFD	Computational Fluid Dynamics
API	Active Pharmaceutical Ingredient
DPIs	Dry Powder Inhalers

CHAPTER 8: CONCLUSIONS AND FURTHER WORK

8.1 Conclusions

In this thesis, we adopted a hybrid approach called the Discrete Multi-Physics combining the method of Smoothed Particle Hydrodynamics to model physiological fluids, the Mass and Spring Model to simulate solid bio-structure and the Discrete Element Method to implement contact mechanisms. These are Lagrangian mesh-free techniques and share a common particle-based framework. Moreover, the use of a unique set of equations and potentials eased high solid deformations which are characteristic of the human tissue.

The technique applied to biological valves highlighted the importance of the mechanical properties of the leaflets as well as the membrane size on the surrounding fluid and their effects on the mechanical stress and stagnation site location. The results showed for instance that rigid and short membranes may be inefficient in preventing blood reflux, but reduce the volume of stagnant blood potentially lowering the chances of thrombosis. Moreover, the addition of a solid formation algorithm in the model emphasised the negative impact of clot-like structures in the hydrodynamics (thrombosis and embolism) and their key role in valve disorder (calcification). Similarly, in respiratory epithelium system, the model correlated the lung cilia motion with the drug diffusion profile in the periciliary layer and suggested the existence of three mass transfer regimes which are a function of drug diffusivity, cilia beat frequency and cilia flexibility. Finally, in respiratory drug delivery system, with the investigation of the release of APIs in dry powder inhalers, a simplified analytic model has been proposed and could be introduced as a sub-scale model in CFD.

With the Discrete Multi-Physics, we have demonstrated that the method is more than an alternative approach and can cover a wide range of applications with relative ease.

Additionally, traditional domains of investigation which are usually considered challenges can now be investigated with this methodology.

However, despite the fact that the Discrete Multi-Physics has the potential to be a support in-silico research tool (e.g. in medicine), further work is still required. Indeed, the limitations of the thesis remain the lack of comparison with experimental studies and a better definition of physical and chemical properties. Finally, the time of calculation remains higher than the standard mesh-based method and consequently should be taken into consideration for scale-up modelling.

8.2 Further work

The implementation and the dissemination of the Discrete Multi-Physics have brought several collaborations with other international research groups which are currently underway. Besides the articles already published or submitted, there are a number of cases that have been studied. In the next sections, we briefly describe some of them.

8.2.1 Three-dimensional metal intra-stent geometry

The work is in collaboration with the Université Euro-Méditerranéenne de Fès in Morocco. The idea in this study is to use the Discrete Multi-Physics to implement a three-dimensional stent model including blood hydrodynamics, stent mechanics and to quantify the impact of potential agglomeration phenomena which can be initiated in the vicinity of the stent.

The model simulates the blood dynamics in a three-dimensional channel similar to a coronary artery (internal radius = 1.5 10^{-3} m) including a stent of 4 struts (x-direction) and 2 struts (z-direction) (Fig. 8.1a). The geometry is similar to the two-dimensional stent model used by

(Chesnutt and Han 2015Chesnutt and Han 2015). The inlet/outlet boundary conditions in the *x*-direction are periodic and we use two symmetrical planes in the *y*-direction and the *z*-direction.

The velocity profile (Fig. 8.1b) shows that the symmetry is properly represented with a parabolic shape from the centre to the border (Laminar and Newtonian flow). The velocity magnitude (*Vmag*) and velocity vectors (Fig. 8.1c) are also consistent with the literature (Chesnutt and Han 2015).

Moreover, in this case, by using a non-rigid stent (solid stent particles are linked with each other using a cross bond methodology (see Chapter 5)), stress (*T shear*) inside the stent can be quantified (Fig. 8.1d).

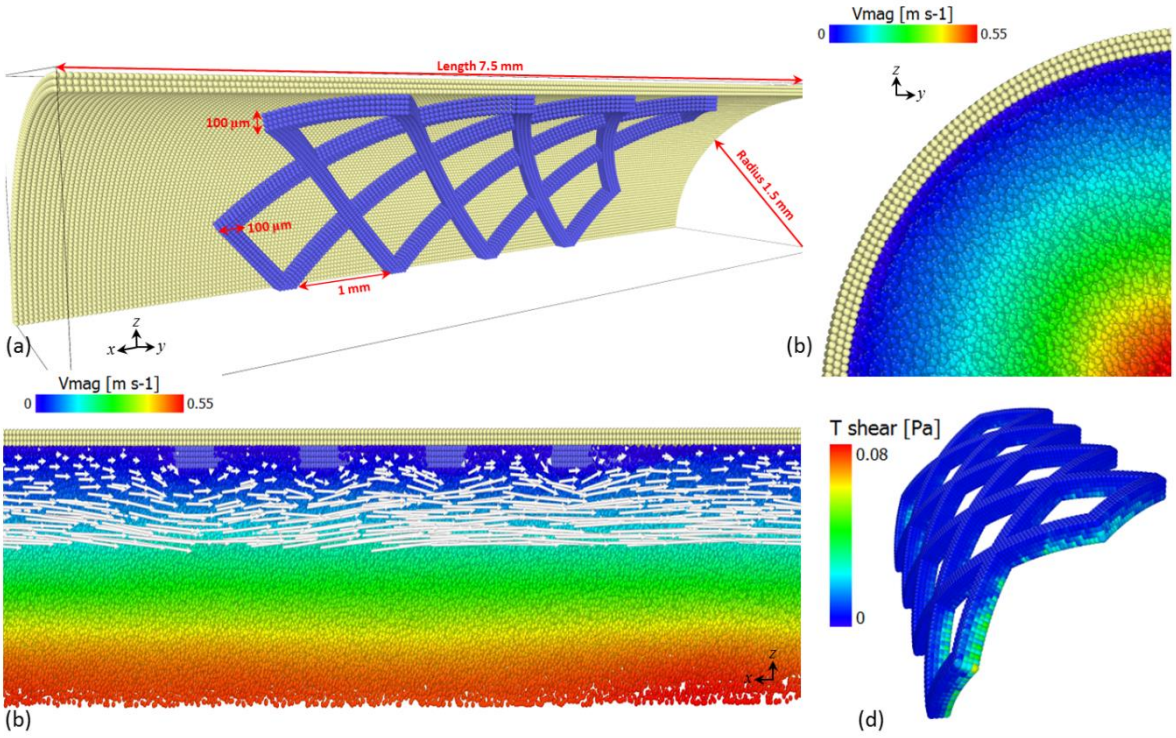

Fig. 8.1. (a) Illustration of the 3D stent geometry, (b) velocity profile in the *y*-direction, (c) velocity profile and vectors in the *x*-direction and (d) Shear stress in the stent.

Concerning the agglomeration process, the algorithm used in the previous chapters (see Chapter 3 and Chapter 4) can be optimised in order to add a threshold activation condition (Fig. 8.2). Every time step, during the identification of the particle position, the code outputs the information related to the particle forces and then calculates the corresponding shear stress. If the value is above a certain threshold, the solid formation is either always active or active every 2-N time step.

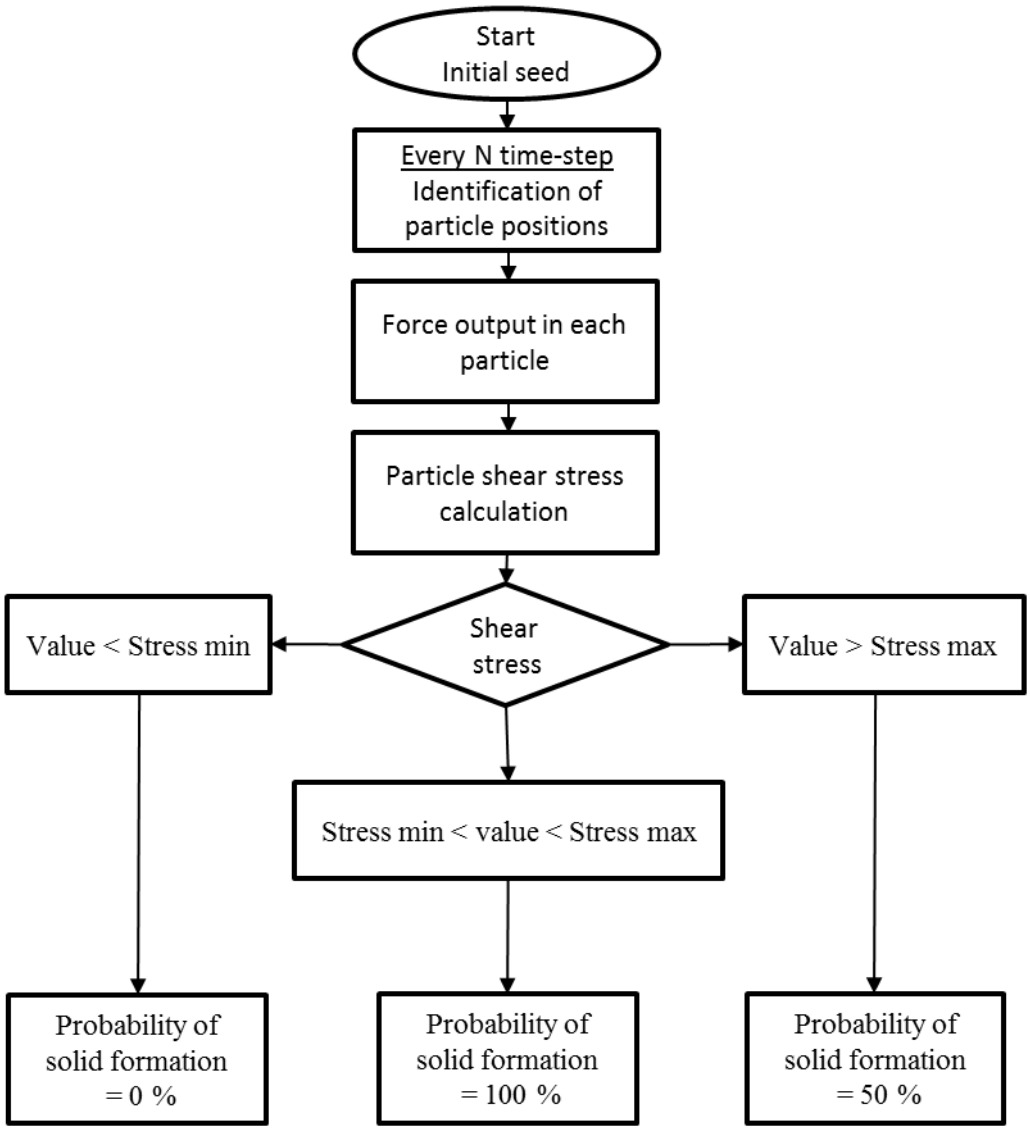

Fig. 8.2. Solid agglomeration with three level of probability.

8.2.2 Optimisation of a tricuspid heart valve

The work is in collaboration with the University of Sydney and the Heart Centre for Children (Australia). The purpose of this collaboration is to produce a prosthetic baby valve system. The Discrete Multi-Physics is used here in order to implement and simulate different configurations of designs with leaflets contact and valve closure. In the first step of the study, a three-dimensional heart valve is implemented with the model (Fig. 8.3a) and then, after calibration, the valve deformation is analysed and compared with the literature (Fig. 8.3b). The second step is to measure the required physical properties for an ideal valve material which will be tested by the experimental team in Australia.

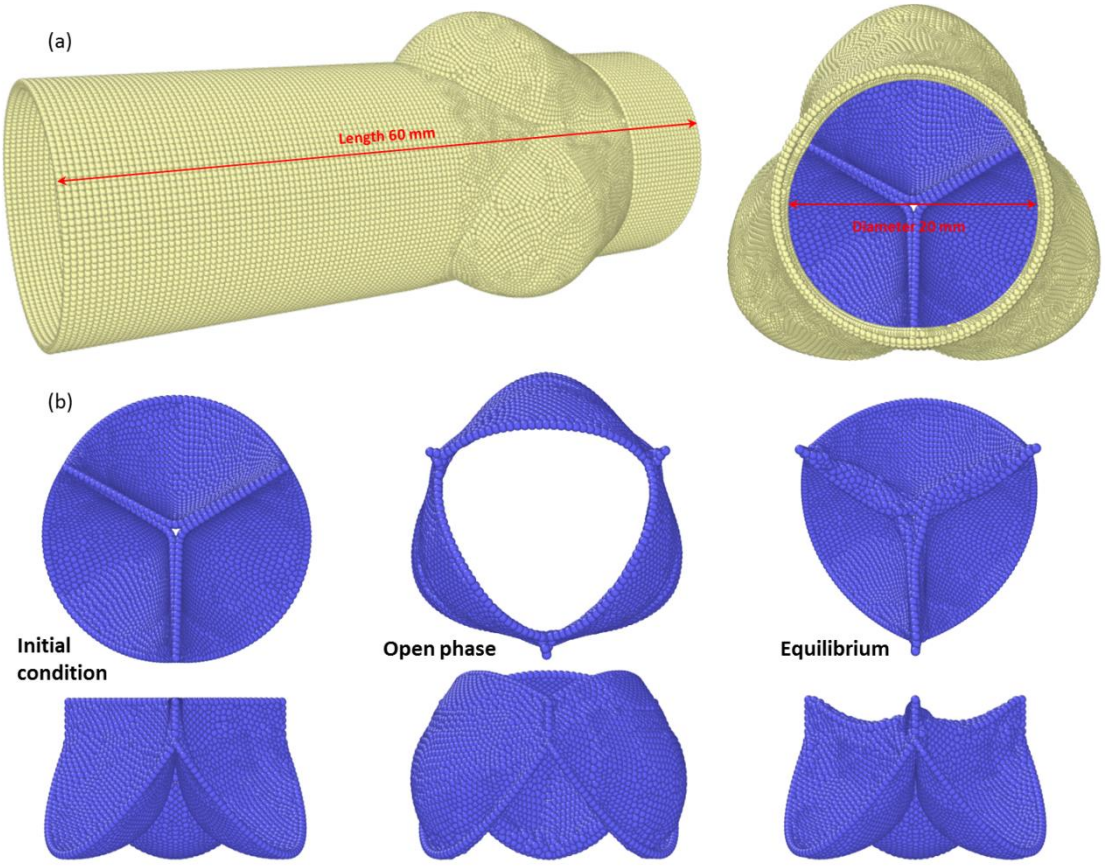

Fig. 8.3. Tricuspid heart valve. (a) Geometry, (b) Valve deformation before the simulation, during the opening phase and during the closing phase (equilibrium).

ACKNOWLEDGEMENTS

The author would like to acknowledge Dr Hatem Allouche, Dr Marco Bussone, Dr Fausto Giacosa, Prof. Frédéric Bernard, Ms Wei Wen, Dr Daniele Vigolo, Dr Alexander Brill, Prof. Gerard Nash, Dr Stravos Kassinos, Dr Sitaram Velaga and Prof. Martin Sommerfeld for their collaboration in the submitted/published articles.

Chapter 6 and Chapter 7 are based upon work from COST Action MP1404 SimInhale 'Simulation and pharmaceutical technologies for advanced patient-tailored inhaled medicines', supported by COST (European Cooperation in Science and Technology).

REFERENCES

Abolfazli, E., N. Fatouraee and B. Vahidi (2014). "Dynamics of motion of a clot through an arterial bifurcation: a finite element analysis." Fluid Dynamics Research **46**(5).

Agnew, J. E., P. P. Sutton, D. Pavia and S. W. Clarke (1986). "Radioaerosol assessment of mucociliary clearance - towards definition of a normal range." British Journal of Radiology **59**(698): 147-151.

Aiello, E. and M. Sleigh (1977). "Ciliary function of the frog oro-pharyngeal epithelium." Cell and Tissue Research **178**(2): 267-278.

Al-Azawy, M. G., A. Turan and A. Revell (2015). "Assessment of turbulence models for pulsatile flow inside a heart pump." Computer Methods in Biomechanics and Biomedical Engineering: 1-15.

Alexiadis, A. (2014). "A smoothed particle hydrodynamics and coarse-grained molecular dynamics hybrid technique for modelling elastic particles and breakable capsules under various flow conditions." International Journal for Numerical Methods in Engineering **100**(10): 713-719.

Alexiadis, A. (2015a). "The Discrete Multi-Hybrid System for the Simulation of Solid-Liquid Flows." Plos One **10**(5).

Alexiadis, A. (2015b). A new framework for modelling the dynamics and the breakage of capsules, vesicles and cells in fluid flow. Iutam Symposium on Dynamics of Capsules, Vesicles and Cells in Flow. D. BarthesBiesel, M. G. Blyth and A. V. Salsac. **16:** 80-88.

Alexiadis, A., D. A. Lockerby, M. K. Borg and J. M. Reese (2014). "The atomistic-continuum hybrid taxonomy and the hybrid-hybrid approach." International Journal for Numerical Methods in Engineering **98**(7): 534-546.

Alexiadis, A., K. Stamatopoulos, W. Wen, H. K. Batchelor, S. Bakalis, M. Barigou and M. J. H. Simmons (2017). "Using discrete multi-physics for detailed exploration of hydrodynamics in an in vitro colon system." Computers in Biology and Medicine **81**: 188-198.

Ariane, M., M. H. Allouche, M. Bussone, F. Giacosa, F. Bernard, M. Barigou and A. Alexiadis (2017a). "Discrete multi-physics: A mesh-free model of blood flow in flexible biological valve including solid aggregate formation." Plos One **12**(4).

Ariane, M., W. Wen, D. Vigolo, A. Brill, F. G. B. Nash, M. Barigou and A. Alexiadis (2017b). "Modelling and simulation of flow and agglomeration in deep veins valves using discrete multi physics." Computers in Biology and Medicine(89): 96-103.

Astorino, M., J. Hamers, S. C. Shadden and J.-F. Gerbeau (2012). "A robust and efficient valve model based on resistive immersed surfaces." International Journal for Numerical Methods in Biomedical Engineering **28**(9): 937-959.

Aycock, K. I., R. L. Campbell, K. B. Manning and B. A. Craven (2017). "A resolved two-way coupled CFD/6-DOF approach for predicting embolus transport and the embolus-trapping efficiency of IVC filters." Biomechanics and Modeling in Mechanobiology **16**(3): 851-869.

Badano, J. L., N. Mitsuma, P. L. Beales and N. Katsanis (2006). "The Ciliopathies: An Emerging Class of Human Genetic Disorders." Annual Review of Genomics and Human Genetics **7**(1): 125-148.

Bahraseman, H. G., K. Hassani, A. Khosravi, M. Navidbakhsh, D. M. Espino, N. Fatouraee and D. Kazemi-Saleh (2014). "Combining numerical and clinical methods to assess aortic valve hemodynamics during exercise." Perfusion-Uk **29**(4): 340-350.

Bajd, F. and I. Sersa (2013). "Mathematical Modeling of Blood Clot Fragmentation During Flow-Mediated Thrombolysis." Biophysical Journal **104**(5): 1181-1190.

Barton, C. and S. Raynor (1967). "Analytical investigation of cilia induced mucous flow." Bulletin of Mathematical Biophysics **29**(3): 419-&.

Basting, S., A. Quaini, S. Canic and R. Glowinski (2017). "Extended ALE Method for fluid-structure interaction problems with large structural displacements." Journal of Computational Physics **331**: 312-336.

Bavo, A. M., G. Rocatello, F. Iannaccone, J. Degroote, J. Vierendeels and P. Segers (2016). "Fluid-Structure Interaction Simulation of Prosthetic Aortic Valves: Comparison between Immersed Boundary and Arbitrary Lagrangian-Eulerian Techniques for the Mesh Representation." Plos One **11**(4).

Belytschko, T., Y. Krongauz, D. Organ, M. Fleming and P. Krysl (1996). "Meshless methods: An overview and recent developments." Computer Methods in Applied Mechanics and Engineering **139**(1–4): 3-47.

Belytschko, T., Y. Y. Lu and L. Gu (1994). "Element-free galerkin methods." International Journal for Numerical Methods in Engineering **37**(2): 229-256.

Bird, R., B., W. Stewart, E. and E. Lightfoot, N. (2002). Transport phenomena, J. Wiley.

Blake, J. R. (1984). "Mechanics of Muco-ciliary Transport." IMA Journal of Applied Mathematics **32**(1-3): 69-87.

Borazjani, I. (2015). "A Review of Fluid-Structure Interaction Simulations of Prosthetic Heart Valves." **25**(1-2): 75-93.

Boucher, R. C. (2007). Airway surface dehydration in cystic fibrosis: Pathogenesis and therapy. Annual Review of Medicine. **58:** 157-170.

Bovill, E. G. and A. van der Vliet (2011). Venous Valvular Stasis-Associated Hypoxia and Thrombosis: What Is the Link? Annual Review of Physiology, Vol 73. D. Julius and D. E. Clapham. **73:** 527-545.

Bradley, R. S. (1932). "The cohesive force between solid surfaces and the surface energy of solids." Philosophical Magazine **13**(86): 853-862.

Brilliantov, N. V., F. Spahn, J. M. Hertzsch and T. Poschel (1996). "Model for collisions in granular gases." Physical Review E **53**(5): 5382-5392.

Buxton, G. A. and N. Clarke (2006). "Computational phlebology: The simulation of a vein valve." Journal of Biological Physics **32**(6): 507-521.

Carrascal, P. G., J. G. Garcia, J. S. Pallares, F. C. Ruiz and F. J. M. Martin (2017). "Numerical Study of Blood Clots Influence on the Flow Pattern and Platelet Activation on a Stented Bifurcation Model." Annals of Biomedical Engineering **45**(5): 1279-1291.

Chan, H. K. (2006). "Dry powder aerosol delivery systems: Current and future research directions." Journal of Aerosol Medicine-Deposition Clearance and Effects in the Lung **19**(1): 21-27.

Chatelin, R., D. Anne-Archard, M. Murris-Espin, M. Thiriet and P. Poncet (2017). "Numerical and experimental investigation of mucociliary clearance breakdown in cystic fibrosis." Journal of Biomechanics **53**: 56-63.

Chesnutt, J. K. W. and H. C. Han (2015). "Simulation of the microscopic process during initiation of stent thrombosis." Computers in Biology and Medicine **56**: 182-191.

Chilvers, M. A. and C. O'Callaghan (2000). "Analysis of ciliary beat pattern and beat frequency using digital high speed imaging: comparison with the photomultiplier and photodiode methods." Thorax **55**(4): 314-317.

Chilvers, M. A., A. Rutman and C. O'Callaghan (2003a). "Ciliary beat pattern is associated with specific ultrastructural defects in primary ciliary dyskinesia." Journal of Allergy and Clinical Immunology **112**(3): 518-524.

Chilvers, M. A., A. Rutman and C. O'Callaghan (2003b). "Functional analysis of cilia and ciliated epithelial ultrastructure in healthy children and young adults." Thorax **58**(4): 333-338.

Chorin, A. J. and P. S. Bernard (1973). "Discretization of a vortex sheet, with an example of roll-up." Journal of Computational Physics **13**(3): 423-429.

Chueh, J. Y., A. K. Wakhloo, G. H. Hendricks, C. F. Silva, J. P. Weaver and M. J. Gounis (2011). "Mechanical Characterization of Thromboemboli in Acute Ischemic Stroke and Laboratory Embolus Analogs." American Journal of Neuroradiology **32**(7): 1237-1244.

Collins, R., A. Scrimgeour, S. Yusuf and R. Peto (1988). "Reduction in fatal pulmonary embolism and venous thrombosis by perioperative administration of subcutaneous heparin. Overview of results of randomized trials in general, orthopedic, and urologic surgery." N Engl J Med **318**(18): 1162-1173.

Cui, Y., S. Schmalfuss, S. Zellnitz, M. Sommerfeld and N. Urbanetz (2014). "Towards the optimisation and adaptation of dry powder inhalers." International Journal of Pharmaceutics **470**(1-2): 120-132.

Cui, Y. and M. Sommerfeld (2015). "Forces on micron-sized particles randomly distributed on the surface of larger particles and possibility of detachment." International Journal of Multiphase Flow **72**: 39-52.

Cundall, P. A. and O. D. L. Strack (1979). "A Discrete numerical-model for granular assemblies." Geotechnique **29**(1): 47-65.

D'Angelo, A. and B. Franco (2009). "The dynamic cilium in human diseases." PathoGenetics **2**(1): 3.

De Hart, J., G. W. M. Peters, P. J. G. Schreurs and F. P. T. Baaijens (2000). "A two-dimensional fluid-structure interaction model of the aortic value." Journal of Biomechanics **33**(9): 1079-1088.

Diamond, S. L. (2016). "Systems Analysis of Thrombus Formation." Circulation Research **118**(9): 1348-1362.

Duarte, C. A. and J. T. Oden (1996). "An h-p adaptive method using clouds." Computer Methods in Applied Mechanics and Engineering **139**(1-4): 237-262.

Eixarch, H., E. Haltner-Ukomadu, C. Beisswenger and U. Bock (2010). "Drug Delivery to the Lung: Permeability and Physicochemical Characteristics of Drugs as the Basis for a Pulmonary Biopharmaceutical Classification System (pBCS)." Journal of Epithelial Biology & Pharmacology **3**: 1-14.

Esmon, C. T. (2009). "Basic mechanisms and pathogenesis of venous thrombosis." Blood Reviews **23**(5): 225-229.

Espino, D. M., D. E. T. Shepherd and D. W. L. Hukins (2012). "Evaluation of a transient, simultaneous, arbitrary Lagrange-Euler based multi-physics method for simulating the mitral heart valve." Computer Methods in Biomechanics and Biomedical Engineering **17**(4): 450-458.

Fahrni, F., M. W. J. Prins and L. J. van Ijzendoorn (2009). "Micro-fluidic actuation using magnetic artificial cilia." Lab on a Chip **9**(23): 3413-3421.

Fenlon, A. J. and T. David (2001). "Numerical models for the simulation of flexible artificial heart valves: part I--computational methods." Computer methods in biomechanics and biomedical engineering **4**(4): 323-339.

Ferrand, M., D. R. Laurence, B. D. Rogers, D. Violeau and C. Kassiotis (2013). "Unified semi-analytical wall boundary conditions for inviscid, laminar or turbulent flows in the meshless SPH method." International Journal for Numerical Methods in Fluids **71**(4): 446-472.

Frenkel, D. and B. Smit (2002). Chapter 4 - Molecular Dynamics Simulations. Understanding Molecular Simulation (Second Edition). San Diego, Academic Press**:** 63-107.

Gallo, D., U. Gulan, A. Di Stefano, R. Ponzini, B. Luthi, M. Holzner and U. Morbiducci (2014). "Analysis of thoracic aorta hemodynamics using 3D particle tracking velocimetry and computational fluid dynamics." Journal of Biomechanics **47**(12): 3149-3155.

Gheber, L. and Z. Priel (1997). "Extraction of cilium beat parameters by the combined application of photoelectric measurements and computer simulation." Biophysical Journal **72**(1): 449-462.

Gingold, R. A. and J. J. Monaghan (1977). "Smoothed particle hydrodynamics: theory and application to non-spherical stars." Monthly Notices of the Royal Astronomical Society **181**(3): 375-389.

Gottlob, R. and R. May (1986). Venous Valves: Morphology, Function, Radiology, Surgery. New York, Springer-Verlag Wien.

Gray, J. P., J. J. Monaghan and R. P. Swift (2001). "SPH elastic dynamics." Computer Methods in Applied Mechanics and Engineering **190**(49-50): 6641-6662.

Gulan, U., B. Luthi, M. Holzner, A. Liberzon, A. Tsinober and W. Kinzelbach (2012). "Experimental study of aortic flow in the ascending aorta via Particle Tracking Velocimetry." Experiments in Fluids **53**(5): 1469-1485.

Halevi, R., A. Hamdan, G. Marom, M. Mega, E. Raanani and R. Haj-Ali (2015). "Progressive aortic valve calcification: Three-dimensional visualization and biomechanical analysis." Journal of Biomechanics **48**(3): 489-497.

Harlow, F. H. (1964). "The particle-in-cell computing method for fluid dynamics." Methods in Computational Physics **3**: 319-343.

Harrison, S. E., J. Bernsdorf, D. R. Hose and P. V. Lawford (2008). "A lattice Boltzmann framework for simulation of thrombogenesis." Progress in Computational Fluid Dynamics **8**(1-4): 121-128.

Hosseini, S. M. and J. J. Feng (2009). "A particle-based model for the transport of erythrocytes in capillaries." Chemical Engineering Science **64**(22): 4488-4497.

Hou, G. N., J. Wang and A. Layton (2012). "Numerical Methods for Fluid-Structure Interaction - A Review." Communications in Computational Physics **12**(2): 337-377.

Hou, X. Y., X. Sun, Y. T. Shi, K. L. Zhang and J. T. Yao (2015). "Simulation of the Formation Mechanism of Coronary Thrombosis Based on DEM-CFD Coupling." 2015 8th International Conference on Biomedical Engineering and Informatics (Bmei): 24-28.

Hughes, T. J. R., W. K. Liu and T. K. Zimmermann (1981). "Lagrangian-eulerian finite-element formulation for incompressible viscous flows." Computer Methods in Applied Mechanics and Engineering **29**(3): 329-349.

Hunt, B. J. (2009). "The prevention of hospital-acquired venous thromboembolism in the United Kingdom." British Journal of Haematology **144**(5): 642-652.

Ikeda, Y., M. Handa, K. Kawano, T. Kamata, M. Murata, Y. Araki, H. Anbo, Y. Kawai, K. Watanabe, I. Itagaki, K. Sakai and Z. M. Ruggeri (1991). "The role of vonwillebrand-factor and fibrinogen in platelet-aggregation under varying shear-stress." Journal of Clinical Investigation **87**(4): 1234-1240.

Jayathilake, P. G., D. V. Le, Z. Tan, H. P. Lee and B. C. Khoo (2015). "A numerical study of muco-ciliary transport under the condition of diseased cilia." Comput Methods Biomech Biomed Engin **18**(9): 944-951.

Jayathilake, P. G., Z. Tan, D. V. Le, H. P. Lee and B. C. Khoo (2012). "Three-dimensional numerical simulations of human pulmonary cilia in the periciliary liquid layer by the immersed boundary method." Computers & Fluids **67**(Supplement C): 130-137.

Ju, L. N., Y. F. Chen, L. Z. Xue, X. P. Du and C. Zhu (2016). "Cooperative unfolding of distinctive mechanoreceptor domains transduces force into signals." eLife **5**.

Kaialy, W., A. Alhalaweh, S. P. Velaga and A. Nokhodchi (2012). "Influence of lactose carrier particle size on the aerosol performance of budesonide from a dry powder inhaler." Powder Technology **227**(Supplement C): 74-85.

Kamensky, D., M.-C. Hsu, D. Schillinger, J. A. Evans, A. Aggarwal, Y. Bazilevs, M. S. Sacks and T. J. R. Hughes (2015). "An immersogeometric variational framework for fluid–structure interaction: Application to bioprosthetic heart valves." Computer Methods in Applied Mechanics and Engineering **284**: 1005-1053.

Keijsers, J. M. T., C. A. D. Leguy, W. Huberts, A. J. Narracott, J. Rittweger and F. N. van de Vosse (2015). "A 1D pulse wave propagation model of the hemodynamics of calf muscle pump function." International Journal for Numerical Methods in Biomedical Engineering **31**(7).

Ledesma-Alonso, R., J. E. V. Guzman and R. Zenit (2014). "Experimental study of a model valve with flexible leaflets in a pulsatile flow." Journal of Fluid Mechanics **739**: 338-362.

Lee, W. and E. Jung (2015). "A Multiscale Model of Cardiovascular System Including an Immersed Whole Heart in the Cases of Normal and Ventricular Septal Defect (VSD)." Bulletin of Mathematical Biology **77**(7): 1349-1376.

Lee, W. L., P. G. Jayathilake, Z. J. Tan, D. V. Le, H. P. Lee and B. C. Khoo (2011). "Muco-ciliary transport: Effect of mucus viscosity, cilia beat frequency and cilia density." Computers & Fluids **49**(1): 214-221.

Leonard, A. (1980). "Vortex methods for flow simulation." Journal of Computational Physics **37**(3): 289-335.

Leopold, P. L., M. J. O'Mahony, X. J. Lian, A. E. Tilley, B. G. Harvey and R. G. Crystal (2009). "Smoking Is Associated with Shortened Airway Cilia." Plos One **4**(12).

Liu, G. R. and M. B. Liu, Eds. (2003). Smoothed Particle Hyrodynamics: a meshfree method. Singapore, World Scientific Publishing Co. Pte. Ltd.

Liu, G. R. and M. B. Liu, Eds. (2016). Particle Methods for Multi-Scale and Multi-Physics. Singapore, World Scientific Publishing Co. Pte. Ltd.

Liu, M. B. and G. R. Liu (2010). "Smoothed Particle Hydrodynamics (SPH): an Overview and Recent Developments." Archives of Computational Methods in Engineering **17**(1): 25-76.

Liu, W. K., S. Jun and Y. F. Zhang (1995). "Reproducing kernel particle methods." International Journal for Numerical Methods in Fluids **20**(8-9): 1081-1106.

Lobovsky, L. and J. Kren (2007). "Smoothed particle hydrodynamics modelling of fluids and solids." Applied and Computational Mechanics **1**: 521-530.

Lucy, L. B. (1977). "A numerical approach to the testing of the fission hypothesis." Astronomical Journal **82**(12): 1013-1024.

Lurie, F., R. L. Kistner, B. Eklof and D. Kessler (2003). "Mechanism of venous valve closure and role of the valve in circulation: a new concept." Journal of Vascular Surgery **38**(5): 955-961.

Macia, F., J. M. Sanchez, A. Souto-Iglesias and L. M. Gonzalez (2012). "WCSPH viscosity diffusion processes in vortex flows." International Journal for Numerical Methods in Fluids **69**(3): 509-533.

MacIver, D. H., I. Adeniran, I. R. MacIver, A. Revell and H. G. Zhang (2016). "Physiological mechanisms of pulmonary hypertension." American Heart Journal **180**: 1-11.

Marino, M. R. and E. Aiello (1982). "Cinemicrographic analysis of beat dynamics of human respiratory cilia." J Progress in clinical and biological research **80**: 35-39.

Marom, G. (2015). "Numerical Methods for Fluid–Structure Interaction Models of Aortic Valves." Archives of Computational Methods in Engineering **22**(4): 595-620.

Mauroy, B., C. Fausser, D. Pelca, J. Merckx and P. Flaud (2011). "Toward the modeling of mucus draining from the human lung: role of the geometry of the airway tree." Phys Biol **8**(5): 056006.

Menichini, C., Z. Cheng, R. G. J. Gibbs and X. Y. Xu (2016). "Predicting false lumen thrombosis in patient-specific models of aortic dissection." Journal of the Royal Society Interface **13**(124).

Miandehi, E. E., M. H. Aazami, H. Niazmand, Y. Mesri, A. Deyranlou and S. Eslami (2015). "Clinical simulation of aortic valve: a narrative review." Studies in health technology and informatics **210**: 612-616.

Mihos, J. C. and L. Hernquist (1994). "Star-forming galaxy models-Blending star-formation into TREESPH." Astrophysical Journal **437**(2): 611-624.

Milenkovic, J., A. H. Alexopoulos and C. Kiparissides (2013). "Flow and particle deposition in the Turbuhaler: A CFD simulation." International Journal of Pharmaceutics **448**(1): 205-213.

Milenkovic, J., A. H. Alexopoulos and C. Kiparissides (2014). "Deposition and fine particle production during dynamic flow in a dry powder inhaler: A CFD approach." International Journal of Pharmaceutics **461**(1-2): 129-136.

Monaghan, J. J. (1992). "Smoothed Particle Hydrodynamics." Annual Review of Astronomy and Astrophysics **30**: 543-574.

Monaghan, J. J. (1994). "Simulating Free Surface Flows with SPH." Journal of Computational Physics **110**(2): 399-406.

Monaghan, J. J. (2011). "A turbulence model for Smoothed Particle Hydrodynamics." European Journal of Mechanics - B/Fluids **30**(4): 360-370.

Monaghan, J. J. (2012). "Smoothed Particle Hydrodynamics and Its Diverse Applications." Annual Review of Fluid Mechanics, Vol 44 **44**: 323-346.

Monaghan, J. J. and R. A. Gingold (1983). "Shock simulation by the particle method SPH." Journal of Computational Physics **52**(2): 374-389.

Moore, H. M., M. Gohel and A. H. Davies (2011). "Number and location of venous valves within the popliteal and femoral veins - a review of the literature." Journal of Anatomy **219**(4): 439-443.

Morris, J. P. (1996). "A study of the stability properties of smooth particle hydrodynamics." Publications Astronomical Society of Australia **13**(1): 97-102.

Morris, J. P., P. J. Fox and Y. Zhu (1997). "Modeling Low Reynolds Number Incompressible Flows Using SPH." Journal of Computational Physics **136**(1): 214-226.

Mühlberger, D., L. Morandini and E. Brenner (2008). "An anatomical study of femoral vein valves near the saphenofemoral junction." Journal of Vascular Surgery **48**(4): 994-999.

Müller, M., S. Schirm, M. Teschner, B. Heidelberger and G. M (2004). "Interaction of fluids with deformable solids." Computer Animation and Virtual Worlds **W 15**: 159-171.

Narracott, A., S. Smith, P. Lawford, H. Liu, R. Himeno, I. Wilkinson, P. Griffiths and R. Hose (2005). "Development and validation of models for the investigation of blood clotting in idealized stenoses and cerebral aneurysms." Journal of Artificial Organs **8**(1): 56-62.

Nayroles, B., G. Touzot and P. Villon (1992). "Generalizing the finite element method: Diffuse approximation and diffuse elements." Computational Mechanics **10**(5): 307-318.

Oldenburg, A. L., R. K. Chhetri, D. B. Hill and B. Button (2012). "Monitoring airway mucus flow and ciliary activity with optical coherence tomography." Biomedical Optics Express **3**(9): 1978-1992.

Olsson, B., E. Bondesson, L. Borgstrom, S. Edsbacker, S. Eirefelt, K. Ekelund, L. Gustavsson and T. Hegelund-Myrback (2011). Pulmonary Drug Metabolism, Clearance, and Absorption. Controlled Pulmonary Drug Delivery. H. D. C. Smyth and A. J. Hickey**:** 21-50.

Ouared, R. and B. Chopard (2005). "Lattice Boltzmann simulations of blood flow: Non-Newtonian rheology and clotting processes." Journal of Statistical Physics **121**(1-2): 209-221.

Panteleev, M. A., N. M. Dashkevich and F. I. Ataullakhanov (2015). "Hemostasis and thrombosis beyond biochemistry: roles of geometry, flow and diffusion." Thrombosis Research **136**(4): 699-711.

Peskin, C. S. (2002). "The immersed boundary method." Acta Num. **11**: 479-517.

Plimpton, S. (1995). "Fast parallel algorithms for short-range molecular-dynamics." Journal of Computational Physics **117**(1): 1-19.

Popinet, S. (2003). "Gerris: a tree-based adaptive solver for the incompressible Euler equations in complex geometries." Journal of Computational Physics **190**(2): 572-600.

Popov, V. L. (2010). Contact Mechanics and Friction: Physical Principles and Applications.

Priori, S. G., C. Blomstrom-Lundqvist, A. Mazzanti, N. Blom, M. Borggrefe, J. Camm, P. M. Elliott, D. Fitzsimons, R. Hatala, G. Hindricks, P. Kirchhof, K. Kjeldsen, K. H. Kuck, A. Hernandez-Madrid, N. Nikolaou, T. M. Norekval, C. Spaulding, D. J. Van Veldhuisen, C. European Soc and C. Assoc European Paediat (2015). "2015 ESC Guidelines for the management of patients with ventricular arrhythmias and the prevention of sudden cardiac death." Europace **17**(11): 1601-1687.

Reitsma, P. H., H. H. Versteeg and S. Middeldorp (2012). "Mechanistic View of Risk Factors for Venous Thromboembolism." Arteriosclerosis Thrombosis and Vascular Biology **32**(3): 563-568.

Reychler, G., J. F. Dessanges, L. Vecellio, G. Reychler, J. F. Dessanges and L. Vecellio (2007). "Aérosols : Présent et futur." Revue Des Maladies Respiratoires **24**(8): 1013-1023.

Sanderson, M. J. and M. A. Sleigh (1981). "Ciliary activity of cultured rabbit tracheal epithelium - beat pattern and metachrony." Journal of Cell Science **47**(FEB): 331-347.

Scarpa, F., S. Adhikari, A. J. Gil and C. Remillat (2010). "The bending of single layer graphene sheets: the lattice versus continuum approach." Nanotechnology **21**(12): 125702.

Sedaghat, M. H., M. M. Shahmardan, M. Norouzi, P. G. Jayathilake and M. Nazari (2016). "Numerical simulation of muco-ciliary clearance: immersed boundary lattice Boltzmann method." Computers & Fluids **131**: 91-101.

Shahriari, S. (2011). Computational Modeling of Cardiovascular Flows using Smoothed Particle Hydrodynamics. Degree of Doctor of Philosophy (Mechanical Engineering), Concordia University.

Shahriari, S., H. Maleki, I. Hassan and L. Kadem (2012). "Evaluation of shear stress accumulation on blood components in normal and dysfunctional bileaflet mechanical heart valves using smoothed particle hydrodynamics." Journal of Biomechanics **45**(15): 2637-2644.

Simão, M., J. M. Ferreira, J. Mora-Rodriguez and H. M. Ramos (2016). "Identification of DVT diseases using numerical simulations." Medical & Biological Engineering & Computing **54**(10): 1591-1609.

Sinnott, M. D., P. W. Cleary, J. W. Arkwright and P. G. Dinning (2012). "Investigating the relationships between peristaltic contraction and fluid transport in the human colon using Smoothed Particle Hydrodynamics." Computers in Biology and Medicine **42**(4): 492-503.

Smith, D. J., E. A. Gaffney and J. R. Blake (2008). "Modelling mucociliary clearance." Respiratory Physiology & Neurobiology **163**(1-3): 178-188.

Sommerfeld, M. and S. Schmalfuss (2016). "Numerical Analysis of Carrier Particle Motion in a Dry Powder Inhaler." Journal of Fluids Engineering-Transactions of the Asme **138**(4).

Swegle, J. W. and S. W. Attaway (1995). "On the feasibility of using smoothed particle Hydrodynamics for underwater explosion calculations." Computational Mechanics **17**(3): 151-168.

Tapson, V. F. (2008). "Acute Pulmonary Embolism." The New England journal of medecine(358): 1037-1052.

Thornton, C. and K. K. Yin (1991). "Impact of elastic spheres with and without adhesion." Powder Technology **65**(1-3): 153-166.

Tilley, A. E., M. S. Walters, R. Shaykhiev and R. G. Crystal (2015). Cilia Dysfunction in Lung Disease. Annual Review of Physiology, Vol 77. D. Julius. **77:** 379-+.

Tong, Z., W. Zhong, A. Yu, H.-K. Chan and R. Yang (2016). "CFD–DEM investigation of the effect of agglomerate–agglomerate collision on dry powder aerosolisation." Journal of Aerosol Science **92**(Supplement C): 109-121.

Tong, Z. B., H. Kamiya, A. B. Yu, H. K. Chan and R. Y. Yang (2015). "Multi-Scale Modelling of Powder Dispersion in a Carrier-Based Inhalation System." Pharmaceutical Research **32**(6): 2086-2096.

Tong, Z. B., R. Y. Yang, A. B. Yu, S. Adi and H. K. Chan (2009). "Numerical modelling of the breakage of loose agglomerates of fine particles." Powder Technology **196**(2): 213-221.

van Loon, R. (2010). "Towards computational modelling of aortic stenosis." International Journal for Numerical Methods in Biomedical Engineering **26**(3-4): 405-420.

van Loon, R., P. D. Anderson, J. de Hart and F. P. T. Baaijens (2004). "A combined fictitious domain/adaptive meshing method for fluid-structure interaction in heart valves." International Journal for Numerical Methods in Fluids **46**(5): 533-544.

van Loon, R., P. D. Anderson and F. N. van de Vosse (2006). "A fluid-structure interaction method with solid-rigid contact for heart valve dynamics." Journal of Computational Physics **217**(2): 806-823.

van Wachem, B., K. Thalberg, J. Remmelgas and I. Niklasson-Bjorn (2017). "Simulation of dry powder inhalers: Combining micro-scale, meso-scale and macro-scale modeling." Aiche Journal **63**(2): 501-516.

Violeau, D. and R. Issa (2007). "Numerical modelling of complex turbulent free-surface flows with the SPH method: an overview." International Journal for Numerical Methods in Fluids **53**(2): 277-304.

Wang, Y., Y. Gao, H. M. Wyss, P. D. Anderson and J. M. J. den Toonder (2015). "Artificial cilia fabricated using magnetic fiber drawing generate substantial fluid flow." Microfluidics and Nanofluidics **18**(2): 167-174.

Watton, P. N., X. Y. Luo, X. Wang, G. M. Bernacca, P. Molloy and D. J. Wheatley (2007). "Dynamic modelling of prosthetic chorded mitral valves using the immersed boundary method." Journal of Biomechanics **40**(3): 613-626.

Wijeratne, N. S. and K. A. Hoo (2008). Numerical studies on the hemodynamics in the human vein and venous valve. 2008 American Control Conference, Vols 1-12. New York, Ieee**:** 147-152.

Wu, K., D. M. Yang and N. Wright (2016). "A coupled SPH-DEM model for fluid-structure interaction problems with free-surface flow and structural failure." Computers & Structures **177**: 141-161.

Yang, J. C., C. Y. Wu and M. Adams (2015). "DEM analysis of the effect of particle-wall impact on the dispersion performance in carrier-based dry powder inhalers." International Journal of Pharmaceutics **487**(1-2): 32-38.

Zhang, H. P. and H. A. Makse (2005). "Jamming transition in emulsions and granular materials." Physical Review E **72**(1).

Zhang, J.-n., A. L. Bergeron, Q. Yu, C. Sun, L. V. McIntire, J. A. López and J.-f. Dong (2002). "Platelet Aggregation and Activation under Complex Patterns of Shear Stress." Thrombosis and Haemostasis **88**(11): 817-821.

Zhou, Q. T., Z. Tong, P. Tang, M. Citterio, R. Yang and H.-K. Chan (2013). "Effect of Device Design on the Aerosolization of a Carrier-Based Dry Powder Inhaler—a Case Study on Aerolizer® Foradile®." The AAPS Journal **15**(2): 511-522.